BEILSTEIN JOURNAL OF NANOTECHNOLOGY

Low-dimensional nanomaterials for sustainable applications

Edited by Sandeep Kumar and Ajeet Kaushik

Imprint

Beilstein Journal of Nanotechnology
www.bjnano.org
ISSN 2190-4286
Email: journals-support@beilstein-institut.de

The *Beilstein Journal of Nanotechnology* is published by the Beilstein-Institut zur Förderung der Chemischen Wissenschaften.

Beilstein-Institut zur Förderung der Chemischen Wissenschaften
Trakehner Straße 7–9
60487 Frankfurt am Main
Germany
www.beilstein-institut.de

BEILSTEIN JOURNAL OF NANOTECHNOLOGY

Tailoring of physical properties of RF-sputtered ZnTe films: role of substrate temperature

Kafi Devi, Usha Rani, Arun Kumar, Divya Gupta and Sanjeev Aggarwal*

Full Research Paper

Open Access

Address:
Ion Beam Centre, Department of Physics, Kurukshetra University, Kurukshetra-136119, India

Email:
Sanjeev Aggarwal* - saggarwal@kuk.ac.in

* Corresponding author

Keywords:
bandgap; physical properties; RF sputtering; substrate temperature; ZnTe

Beilstein J. Nanotechnol. **2025,** *16,* 333–348.
https://doi.org/10.3762/bjnano.16.25

Received: 30 September 2024
Accepted: 04 February 2025
Published: 05 March 2025

This article is part of the thematic issue "Low-dimensional nanomaterials for sustainable applications".

Associate Editor: J. J. Schneider

Abstract

In this study, zinc telluride (ZnTe) films were grown on quartz substrates at room temperature, 300 °C, 400 °C, 500 °C, and 600 °C using RF sputtering. The thickness of the films has been found to decrease from 940 nm at room temperature to 200 nm at 600 °C with increasing substrate temperature. The structural investigation using grazing incidence angle X-ray diffraction revealed that films deposited at room temperature are amorphous; those deposited at other substrate temperatures are polycrystalline with a cubic zincblende structure and a preferred orientation along the [111] direction. An increase in crystallite size (from 37.60 ± 0.42 Å to 68.88 ± 1.04 Å) is observed with increased substrate temperature. This leads to a reduction in microstrain and dislocation density. The optical studies using UV–vis–NIR spectroscopy reveal that the transmittance of films increases with substrate temperature. Further, the shift in transmittance threshold towards lower wavelengths with substrate temperature indicates that the optical bandgap of the films can be tuned from 1.47 ± 0.02 eV to 3.11 ± 0.14 eV. The surface morphology of the films studied using atomic force microscopy reveals that there is uniform grain growth on the surface. Various morphological parameters such as roughness, particle size, particle density, skewness, and kurtosis were determined. Current–voltage characteristics indicate that the conductivity of the films increased with substrate temperature. The observed variations in structural, morphological, and optical parameters have been discussed and correlated. The wide bandgap (3.11 eV), high crystallinity, high transmittance, and high conductivity of the ZnTe film produced at 600 °C make it a suitable candidate for use as a buffer layer in solar cell applications.

Introduction

The industrialization and burning of fossil fuels to fulfil the growing demands of energy results in environmental pollution. Environmentally friendly resources such as solar and wind energy can act as a substitute for these non-renewable energy resources because of their sustainability and abundance. Commonly, silicon-based solar cells are used for this purpose. How-

ever, the requirement of very pure material for making these devices leads to high production cost. Metal chalcogenide-based solar cells, because of their low cost and comparable efficiency, can act as a substitute for the Si-based technology. Metal chalcogenide (II–VI) compounds have numerous applications in optoelectronic devices such as light-emitting diodes [1], display devices [2], infrared detectors [3], and terahertz emitters [4]. Owing to their suitable physical properties (deposition at low temperatures and good thermal stability) and unique optical properties due to quantum confinement size effects, metal chalcogenides are of importance in different technological domains. Metal chalcogen compounds are composed of a transition metal with one or more members of the chalcogen family, and they exhibit semiconducting properties.

Zinc telluride (ZnTe) is a binary II–VI semiconductor with a direct bandgap of 2.26 eV, which lies in the visible range of the electromagnetic spectrum. ZnTe is a p-type semiconductor because of zinc vacancies and has a low electron affinity of 3.53 eV at room temperature [5]. It exists in both zincblende and wurtzite structures, depending on the deposition method and deposition parameters. ZnTe is sensitive towards visible and infrared illumination; hence, it is used in the fabrication of optoelectronic devices and infrared detectors. Moreover, its electrical aspects are alterable in intrinsic or doped binary (ZnTe) and ternary (CdZnTe) compounds.

Currently many efforts are made to increase the efficiency of CdTe-based solar cells. A maximum efficiency of 22.1% has been achieved using CdTe-based solar cells. The efficiency can be tuned by the formation of a stable ohmic back contact. For this, a material with a bandgap greater than 5.78 eV, that is, the sum of CdTe electron affinity (4.28 eV) and bandgap (1.5 eV), would be required. Such a material is not available; therefore, the formation of a Schottky barrier is unavoidable. Because of the small 0.1 eV valance band offset at the CdTe/ZnTe interface, which is best for carrier transport, ZnTe can be used as a buffer layer in CdTe-based solar cells for back contact. Moreover, n-type zinc telluride films can be used in the window layer as a substitute for CdS [6].

Zinc telluride films are highly resistive with a resistivity of about several megaohm·centimetres [7]. The resistivity of the films depends on the structure, grain boundary defects, and surface morphology of the films. These properties can be altered by varying the deposition method as well as the deposition parameters. In literature, there are several reports of zinc telluride films deposited using various physical and chemical methods such as molecular beam epitaxy [8], electron-beam evaporation [9], thermal evaporation [10], pulsed laser deposition (PLD) [11], and RF sputtering [12]. RF sputtering is a versatile technique because various process parameters such as RF power, deposition time, substrate–target distance, substrate temperature, and pressure during deposition inside the chamber can be varied. These process parameters have a remarkable impact on the structural, optical, and electrical properties of the grown films. Further, films with uniform thickness can be grown using this technique.

Bellakhder et al. [13] have investigated the impact of varying RF power on the structure, optical, and electrical properties of RF-sputtered ZnTe films and found that the deposited films are highly resistive and have low refractive index because of the polycrystalline nature of films. Isik et al. [14] carried out studies on the structure and temperature-dependent optical properties of magnetron-sputtered ZnTe films. Bacaksiz et al. [15] reported the effect of substrate temperature (−123 and 27 °C) on structural, morphological, optical, and electrical properties of ZnTe films deposited by evaporation. Rakhshani et al. [16] reported the impact of substrate temperature (35 and 305 °C), thermal annealing, and nitrogen doping on optoelectronic properties of ZnTe films and established an optimal doping concentration of nitrogen for lowering the resistivity of the grown films. Further, there are reports [17-23] which show that chemical composition and morphology of the substrate affect the properties of grown films. Therefore, a suitable substrate needs to selected before the deposition of films. The thermal expansion coefficient of substrate and the lattice mismatch between film and substrate are two important parameters for substrate selection. To the best of our knowledge, studies related to the impact of the substrate (silicon and quartz) and film deposition temperature up to 600 °C on the structural, morphological, optical, and electrical behaviour of RF-sputtered ZnTe films are very rare. Therefore, it is necessary to carry out a detailed study in this regard and to find out the optimum parameters for film deposition for applications in optoelectronic devices.

Recently we reported the impact of substrate temperature on the structure, morphology, and reflectance behaviour of ZnTe films on silicon substrates [24]. It was observed that 400 °C is the optimum temperature for the growth of ZnTe films.

In this study, our we focus on optimizing the deposition parameters for ZnTe films on quartz substrates and study the impact of substrate temperature (300–600 °C) on various physical properties (structure, morphology, optical and electrical properties, and luminescence) of RF-sputtered ZnTe films. Quartz is an import substrate because of its high transparency, high melting point, and low thermal expansion coefficient. This study helps in optimizing the substrate temperature to grow films with superior quality in terms of grain size, dislocation density, and optical and electrical properties to enhance the

performance of ZnTe-based optoelectronic devices and solar cells.

Experimental

ZnTe films were deposited on quartz (Qz) using RF sputtering at different substrate temperatures. Prior to film deposition, the substrates were cleansed in an ultrasonic cleaner using acetone and isopropyl alcohol sequentially for 10 min at room temperature. The cleaned substrates were then dried in air and placed on the substrate holder in the chamber. A ZnTe target (dimensions 2 inch diameter and 3 mm thickness) having 99.99% purity was used for sputter deposition of the films. The substrate was kept at a distance of 7 cm from the target. The different deposition parameters are specified in Table 1.

Table 1: Deposition parameters for film fabrication.

Deposition parameters	Value
RF power	60 W
base pressure	10^{-5} mbar
working pressure	10^{-3} mbar
deposition environment	Ar gas
Ar gas flow	10 sccm
substrate temperature	room temperature (R.T.), 300 °C, 400 °C, 500 °C, and 600 °C
deposition time	30 min

The thickness of the fabricated ZnTe/Qz films was determined using spectroscopic ellipsometry (SE). The experimental parameters ψ and Δ were recorded at an incident angle of 70° with respect to film surface using a SENTECH ellipsometer in the wavelength range of 200–1000 nm. The thickness of the films was found to be 940 ± 0.53 nm, 623 ± 0.16 nm, 563 ± 0.02 nm, 337 ± 0.02 nm, and 200 ± 0.30 nm for the films deposited at room temperature, 300 °C, 400 °C, 500 °C, and 600 °C, respectively.

The structural aspects of the ZnTe/Qz films were analysed using grazing incidence X-ray diffraction (GXRD) on a Bruker AXS D8 Advance with Cu Kα radiation (λ = 1.5406 Å) available at Ion Beam Centre, Kurukshetra University. The grazing incidence angle was fixed at 0.5°. The diffraction pattern was recorded in the 2θ range of 20°–70° with a step increment of 0.07°.

The optical properties of ZnTe/Qz films were analysed from transmittance spectra obtained using a Shimadzu UV–vis–NIR spectrophotometer (UV-3600 Plus) equipped with Integrating Sphere Assembly (Model-ISR-603) in the wavelength range of 200–2000 nm (accuracy 1 Å) available at Ion Beam Centre, Kurukshetra University.

The photoluminescence (PL) emission spectra of ZnTe/Qz films were recorded using a HORIBA Scientific (Fluorescence 3.5) spectrophotometer under 320 nm excitation produced by a xenon arc lamp.

For investigating the surface topography, atomic force microscopy (AFM) micrographs of ZnTe/Qz films were recorded (scan area 2 × 2 μm^2) using a Bruker multimode-8 AFM in the ScanAsyst mode at the Ion Beam Centre, Kurukshetra University. The obtained micrographs were then analysed regarding various statistical parameters such as roughness, skewness, kurtosis, and power spectral density using the NanoScope Analysis software.

Surface morphology and composition of the films were studied by field-emission scanning electron microscopy attached with energy-dispersive X-ray spectroscopy (EDS) operated at 10 keV.

The current–voltage (*I*–*V*) characteristics of the films were measured in the voltage range from −1 V to 1 V using a two-probe Keithley 4200 A-SCS parametric analyser available at Ion Beam Centre, Kurukshetra University.

Results and Discussion

X-ray diffraction studies

GXRD patterns of ZnTe films grown on quartz substrates at different substrate temperatures (R.T.–600 °C) are presented in Figure 1. A broad hump in the GXRD pattern of the film deposited at room temperature indicates that the film is amorphous. The three diffraction peaks in the GXRD pattern at 2θ = 25.33°, 42.04°, and 49.47° correspond to (111), (220), and (311) reflection planes, respectively. They are observed for all films deposited above room temperature. Another diffraction peak at 2θ = 67.17°, corresponding to (331) reflection planes, starts evolving at a substrate temperature of 400 °C. Indexing of peaks and comparison with JCPDS data (card no. 01-071-8947) reveals that the deposited films are polycrystalline with a cubic zincblende structure. At a substrate temperature of 600 °C, some other diffraction peaks at 2θ = 34.34° and 56.52° are observed. Comparison with the JCPDS card no. 00-019-1482 reveals that these correspond, respectively, to the (102) and (202) reflections of the hexagonal ZnTe phase. Thus, a mixture of phases exists at this substrate temperature. Other very low-intensity peaks at this temperature are from pure Zn and Te.

The deposition temperature affects the preferred crystallite orientation. To quantitatively analyse the impact of deposition

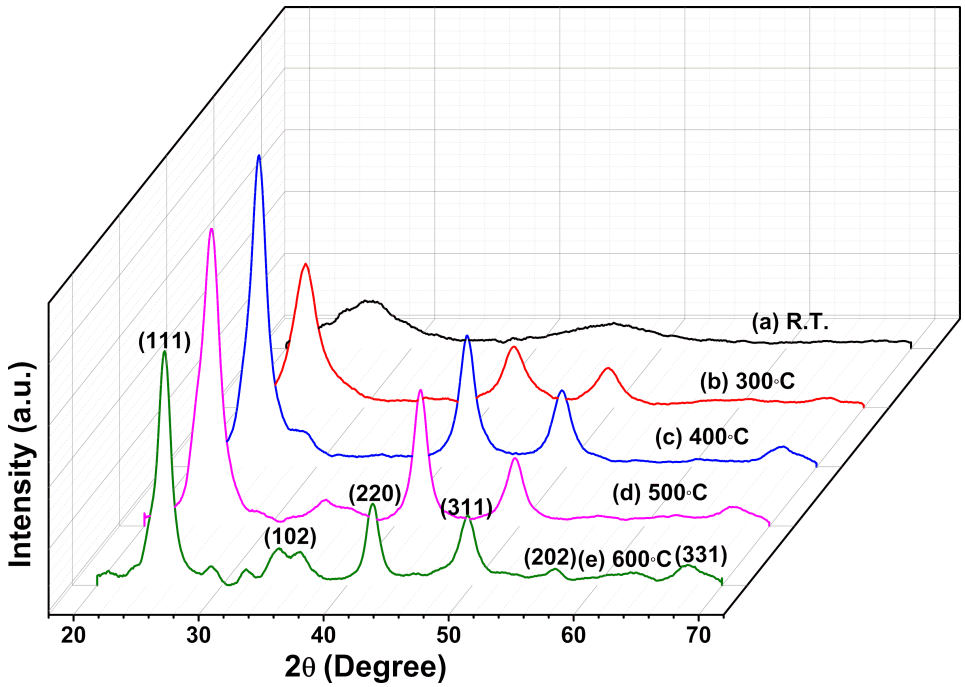

Figure 1: GXRD pattern of the ZnTe/Qz films deposited at room temperature and different substrate temperatures in the range of 300–600 °C.

temperature on the preferred orientation, the texture coefficient (TC(hkl)) was determined using the relation [25]

$$\mathrm{TC}(\mathrm{hkl}) = \frac{\frac{I(\mathrm{hkl})}{I_S(\mathrm{hkl})}}{\frac{1}{n}\sum \frac{I(\mathrm{hkl})}{I_S(\mathrm{hkl})}}, \quad (1)$$

where I(hkl) stands for the Lorentz-fitted peak intensity, I_s(hkl) represents the intensity of peaks in the referenced JCPDS database at corresponding angles, and n represents the number of peaks in the diffraction pattern. The calculated values of TC(hkl) for different diffraction planes is given in Table 2.

TC values greater than or equal to one indicate the preferential orientation in that particular (hkl) direction, that is, more crystallites grow in this particular direction, while TC values less than one indicate that the orientation is random. The TC value of the (111) planes is greater than one, which indicates that [111] is the preferred orientation for all ZnT/Qz film samples.

Table 2: The structural parameters crystallite size (D), dislocation density (Δ), microstrain (ε), interplanar spacing (d_{hkl}), lattice constant (a), and texture coefficient (TC) of ZnTe films fabricated at different substrate temperatures.

Substrate temperature (°C)	2θ (°)	(hkl)	Crystallite size (D)	Δ (×10^{17} m^{-2})	ε (×10^{-2})	d_{hkl} (Å)	a (Å)	TC
R.T.	—	—	—	—	—	—	—	—
300	25.33	(111)	37.60 ± 0.42	0.7	4.3	3.511	6.08	1.28
	42.04	(220)						0.83
	49.47	(311)						0.88
400	25.34	(111)	54.26 ± 0.60	0.3	3.0	3.510	6.08	1.32
	42.05	(220)						0.87
	49.61	(311)						0.80
500	25.30	(111)	52.11 ± 1.10	0.36	3.1	3.516	6.09	1.32
	42.08	(220)						0.96
	49.75	(311)						0.72
600	25.35	(111)	68.88 ± 1.04	0.21	2.4	3.509	6.07	1.34
	42.04	(220)						0.74
	49.61	(311)						0.91

The TC value for the (111) planes increases from 1.16 to 1.34 with the rise of substrate temperature. Other preferred orientations are [220] and [311], but with a smaller degree of texture compared to the [111] direction. The texture coefficient value for the (220) planes increases from 0.83 to 0.96 and decreases for the (311) planes from 0.88 to 0.72 with the rise of substrate temperature (300–500 °C). At a substrate temperature of 600 °C, the TC value for the (311) planes is higher than that for the (220) planes. Further, some other low-intensity peaks corresponding to (102) and (202) planes are also observed at this temperature, which indicates that, at higher substrate temperatures, the preferred orientation and structure may change.

The higher texture coefficient of the (111) planes indicates a minimum surface energy density of these planes because crystal growth in films occurs in the direction of the lowest surface energy. The intensity of X-rays in a diffraction pattern is a function of the atomic structure factor. The change in the texture coefficient of different planes shows that the atomic densities of the planes change with the substrate temperature.

The increase in intensity for the most preferred orientation along the [111] direction is observed with rising substrate temperature up to 400 °C. This may be because atoms have more thermal energy with increasing substrate temperature; therefore, the surface mobility of atoms increases, which leads to rearrangement and the increase in intensity. However, a decrement in intensity is observed for the films deposited at higher substrate temperatures of 500 and 600 °C. This may be because, at rising substrate temperatures, the chance for dissociation and desorption of atoms increases, which causes a decrease in the intensity [26]. To investigate the effect of substrate temperature on peak broadening of ZnTe films, various structural parameters including crystallite size, microstrain, and dislocation density were calculated corresponding to the most prominent peak.

The crystallite size (D) was calculated using Scherrer's formula [27]

$$D = \frac{0.94\lambda}{\beta\cos\theta}, \tag{2}$$

where λ = 1.5406 Å is the X-ray wavelength and β denotes the full width at half maximum (in radians).

The microstrain (ε) is calculated using the formula [27]

$$\varepsilon = \frac{\beta}{4\tan\theta}. \tag{3}$$

The dislocation density (Δ) is calculated using the formula [27]

$$\Delta = \frac{1}{D^2}, \tag{4}$$

where D represents the crystallite size.

The calculated values of D, ε, and Δ are listed in Table 2. Films deposited at R.T. are amorphous; therefore, the crystallite size has not been calculated. The crystallite size increases from 37.60 to 54.26 Å with the rise in substrate temperature from 300 to 400 °C. There is no appreciable change in crystallite size at 500 °C. While a significant increase in crystallite size from 52.11 Å at 500 °C to 68.66 Å at 600 °C is observed. All these alterations in crystallite size can be explained in terms of growth processes occurring during film fabrication. In RF sputtering, the film formation is preceded by three steps, namely, condensation, nucleation, and crystallization on the substrate surface. The mobility of atoms on the substrate surface is very much affected by the substrate temperature. At low substrate temperatures, because of the low diffusion rate and low mobility of atoms, columnar microstructures form on the substrate surface. With the increase in substrate temperature, mobility and diffusion rate of atoms increase, which results in the evolution of grains that further recrystallize at higher substrate temperatures [28]. The observed variation in the crystallite size is due to changes in mobility and diffusion rate of atoms with substrate temperature.

The interplanar spacing (d_{hkl}) and lattice constant (a) were calculated for the (111) plane using Bragg's law [29],

$$d_{hkl} = \frac{n\lambda}{2\sin\theta}, \tag{5}$$

$$a = d_{hkl}\sqrt{h^2 + k^2 + l^2}, \tag{6}$$

where θ represents the Bragg angle, λ is the X-ray wavelength, d is the interplanar spacing, and a is the lattice constant for a particular (hkl) plane. The calculated values are presented in Table 2. The lattice constant value for ZnTe/Qz films is slightly larger than in the bulk (6.07 Å, JCPDS card no.01-071-8947). This may be on account of lattice mismatch or difference in thermal expansion coefficient between film and substrate, which ultimately lead to the development of stress and strain within the film. At a substrate temperature of 600 °C, the lattice constant value is the same as in the bulk material. The strain in films occurs due to lattice mismatch between film and bulk. The microstrain in films was calculated using Equation 3. The microstrain decreases with increasing substrate temperature.

This implies that imperfections along grain boundaries decrease with temperature. The dislocation density, which is defined as the average number of dislocations present per unit volume in a crystal was calculated using Equation 4, and it decreases with increasing substrate temperature. The high value of crystallinity and low value of microstrain and dislocation density at 600 °C shows that good quality films can be fabricated at this temperature.

Morphological investigation

AFM was utilized to study the evolution of surface morphology of ZnTe/Qz films grown at different substrate temperatures. 2D and 3D AFM images (scan area 2 × 2 μm^2) are presented in Figure 2. The 2D images (Figure 2a–e) show that the surface of all film samples is covered with densely packed spherical nanograins. The 3D images (Figure $2a_1$–e_1) reveal a columnar growth on the surface of the films. The AFM micrographs were

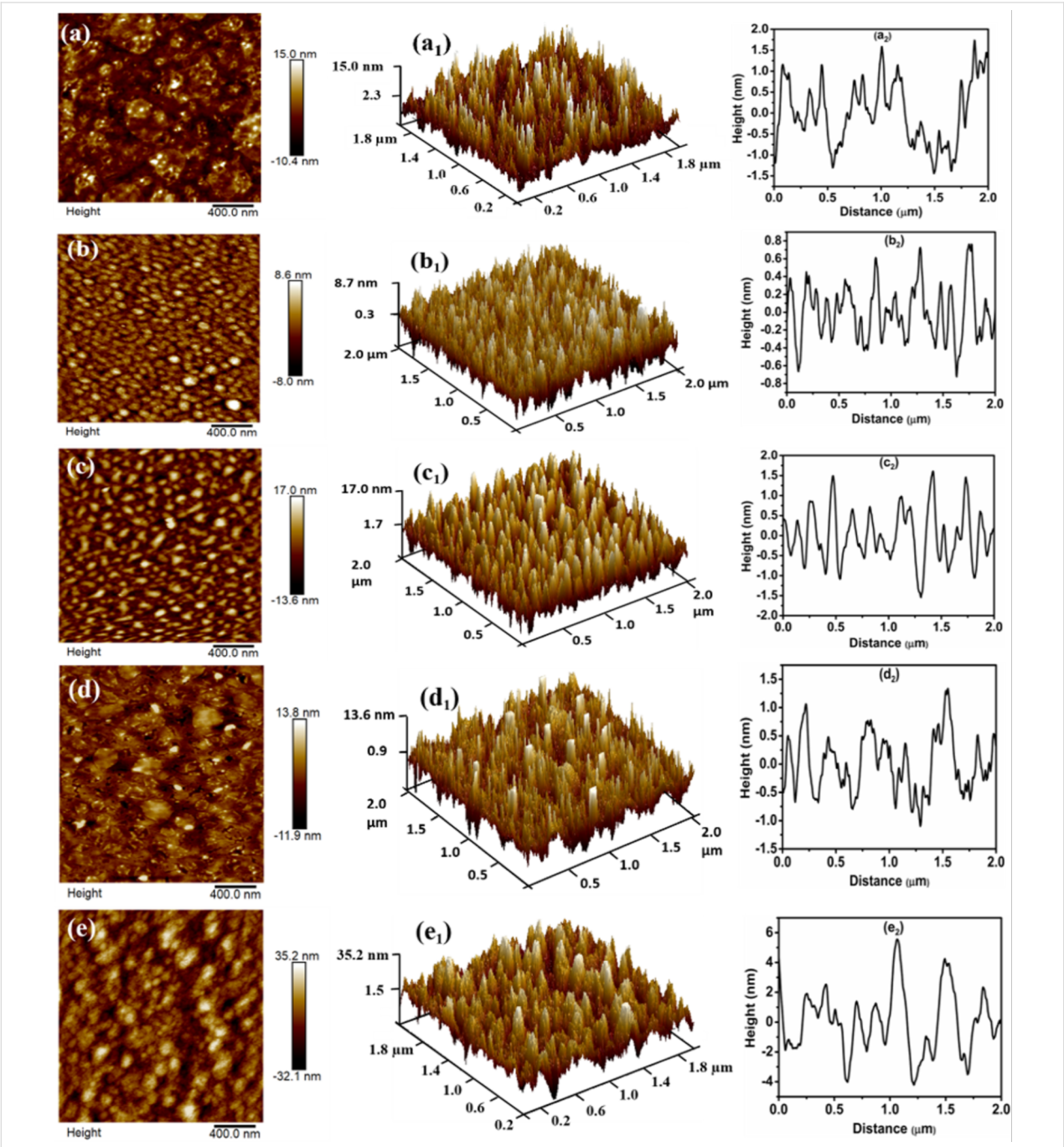

Figure 2: 2D (a–e) and 3D (a_1–e_1) AFM images and Height profile (a_2–e_2) analysis of ZnTe films deposited at (a, a_1, a_2) R.T. and substrate temperatures of (b, b_1, b_2) 300 °C, (c, c_1, c_2) 400 °C, (d, d_1, d_2) 500 °C, and (e, e_1, e_2) 600 °C.

analysed using NanoScope software, and various morphological parameters including roughness, particle density, particle size, skewness, and kurtosis were summarized in Table 3. To investigate the quality of the surface and the texture of the films, the root mean square roughness (R_q) was measured. R_q for the ZnTe film produced at R.T. is 3.49 nm. It increases from 2.27 nm at 300 °C to 3.53 nm at 400 °C. There is no appreciable change in roughness at a substrate temperature of 500 °C (i.e., it lies within the error of the value at 400 °C). However, a significant increase in roughness from 3.12 nm at 500 °C to 9.28 nm at 600 °C was observed. These results are in correlation with our GXRD results, where a similar change in crystallinity was observed with substrate temperature [30]. The surface growth of films can be investigated in terms of two parameters, namely, height fluctuation and lateral aggregation among the spherical nanograins. The height profile for ZnTe films fabricated at various substrate temperatures is given in Figure 2a$_2$–e$_2$. The height fluctuation is related to the number density of particles, and the lateral aggregation is related to the particle size [31].

Figure 2a$_2$–e$_2$ shows that the height fluctuation first increases from R.T. to 300 °C and then continuously decreases with substrate temperature (300–600 °C). This indicates that the particle density first increases and then continuously decreases with substrate temperature accordingly. The lateral aggregation on the surface is inversely related to the height fluctuation. Thus, lateral aggregation (i.e., particle size) first decreases on rising the substrate temperature from R.T. to 300 °C and then continuously increases with substrate temperature (300–600 °C).

The symmetry of the surface of grown films can be investigated in terms of skewness and kurtosis. A zero value of skewness shows that the surface is symmetric, that is, a flat surface. Positive skewness values indicate that peaks are dominant, and negative skewness values indicate that valleys are dominant. The distribution of height on the surface is studied in terms of kurtosis. A kurtosis value equal to three means that the height distribution on the surface is Gaussian, and the surface is called mesokurtic. A kurtosis value of less than three points toward a platykurtic surface, and a kurtosis value greater than three indicates that peaks are dominant. It can be seen from Table 3 that the skewness value is positive and the kurtosis value is greater than three. This shows that peaks are dominant over valleys. This is also evident from the 3D micrographs (Figure 2a$_2$–e$_2$).

The R_q value only gives information about the vertical fluctuation in height on a surface. To get more insight into possible surface growth mechanisms and variations in surface roughness, both vertically and laterally power spectral density (PSD) analyses were carried out. In PSD analysis, the surface is divided into various spatial wavelengths, and a comparative study of roughness is done over different frequency ranges. Figure 3 depicts the log–log plot for the evolution of PSD with spatial frequency (q) for ZnTe/QZ films deposited at different substrate temperatures. The information about surface corrugation is obtained from the slope of the line connecting two points on the surface. The surface corrugation is small for points separated by a length larger than the correlation length ($\eta = 1/q_0$). As a result, for $q < q_o$, the PSD is independent of frequency, and the surface is considered to be flat in this region. But for $q > q_0$, surface corrugation is significant, and the PSD is found to decrease with spatial frequency. The points where a sharp decrease in the PSD curve takes place are indicated in Figure 3 by vertical arrows with values of q_0. The integral of the PSD in the entire frequency range is proportional to the surface roughness. Therefore, PSD curves corresponding to higher roughness should lie at higher ordinates compared to PSD curves for lower roughness. In our case, it was found that the films fabricated at 300 and 600 °C had the lowest and highest roughness, respectively. Therefore, the PSD curves for films fabricated at 300 and 600 °C are at the lowest and highest ordinates, respectively. The PSD curve follows a power law as per equation

$$\mathrm{PSD} = Aq^{-b}, \tag{7}$$

where A is a constant and b is the power law exponent. The value of b gives an idea about the film growth mechanism that is accountable for morphological changes on the surface of

Table 3: Variation in surface parameters (i.e., skewness, kurtosis, roughness, density, and particle size) with substrate temperature.

Substrate temperature (°C)	Roughness (nm)	Particle density (μm^{-2})	Particle size (nm)	Skew-ness	Kurtosis	Power exponent (b)
R.T.	3.49 ± 0.27	37.43	59.03 ± 1.74	0.94	4.64	2.20
300	2.27 ± 0.24	82.22	54.72 ± 1.54	0.19	3.29	1.69
400	3.53 ± 0.23	46.76	58.88 ± 0.70	0.54	3.41	1.60
500	3.12 ± 0.13	45.24	63.58 ± 1.06	0.25	3.91	1.84
600	9.28 ± 0.81	27.13	83.99 ± 1.37	0.15	3.02	1.12

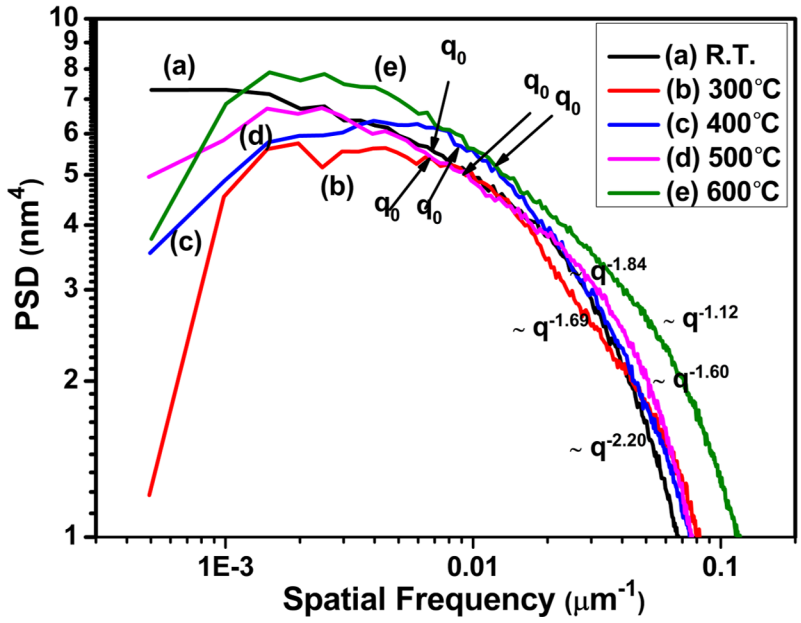

Figure 3: Power spectral density (PSD)-vs-frequency curve of ZnTe films produced at (a) R.T. and substrate temperatures of (b) 300 °C, (c) 400 °C, (d) 500 °C, and (e) 600 °C.

ZnTe films grown on quartz substrate at different substrate temperatures. Values of *b* equal to 1, 2, 3, and 4 represent four surface growth mechanisms, that is, viscous flow, evaporation–condensation, volume diffusion, and surface diffusion, respectively. The experimental data was fitted using Equation 7 in the high-frequency region, and the obtained values of *b* are listed in Table 3. For the film deposited at R.T., the value of *b* lies between 2 and 3, which implies that the possible surface growth mechanism is a combined effect of evaporation–condensation and volume diffusion. The *b* value for the films deposited at substrate temperature of 300–600 °C lies in the range from 1.12 to 1.84. This shows that the possible surface growth mechanism at these temperatures is a combined effect of viscous flow and evaporation–condensation [32].

The microstructure of ZnTe films deposited at different substrate temperatures has been studied using FESEM. The FESEM micrographs are presented in Figure 4a–e, along with the EDS results (Figure 4a$_1$–e$_1$). The films consist of spherical well-connected particles that are uniformly distributed over the entire surface of the substrate. A significant change in particle size along with a change in agglomerated particle density occurs with increasing substrate temperature. The surface is free from pinholes and voids, and clusters of particles can be seen. Quantitative analysis of the surface composition was carried out using EDS, and the obtained spectra are shown in Figure 4a$_1$–e$_1$. The existence of zinc and tellurium peaks indicates the formation of ZnTe thin films. The silicon and oxygen peaks are from the quartz substrate. The atomic percentages of Zn and Te are listed in Table 4. The film deposited at room temperature (R.T.) is of stoichiometric ZnTe. The elemental composition of the films changes with increasing substrate temperature. This variation in the atomic percentage of different elements may be due to the difference in the vapour pressures of Zn and Te.

Optical properties

Transmittance, absorbance, and optical bandgap

The transmittance spectra of fabricated ZnTe/Qz films in the wavelength range from 300 to 2000 nm are presented in Figure 5A. A number of interference fringes are observed in the transmittance spectra for all film samples. The interference fringes in the transmittance spectra result from the interference of two beams, one reflected from the surface and the other from the film–substrate interface. The occurrence of interference fringes in the transmittance spectra implies that there is a well-defined boundary between film and substrate and that films with uniform thickness were grown [33]. The number of interference fringes in the transmission spectra is related to the thickness of the deposited film. With increasing substrate temperature, the desorption of atoms increases. For the film deposited at substrate temperatures of 500 and 600 °C, the thickness of deposited films is low compared to that of films deposited at lower substrate temperatures. Because of this, the transmission spectra of the films deposited at these substrate temperatures differ from the others [15,17].

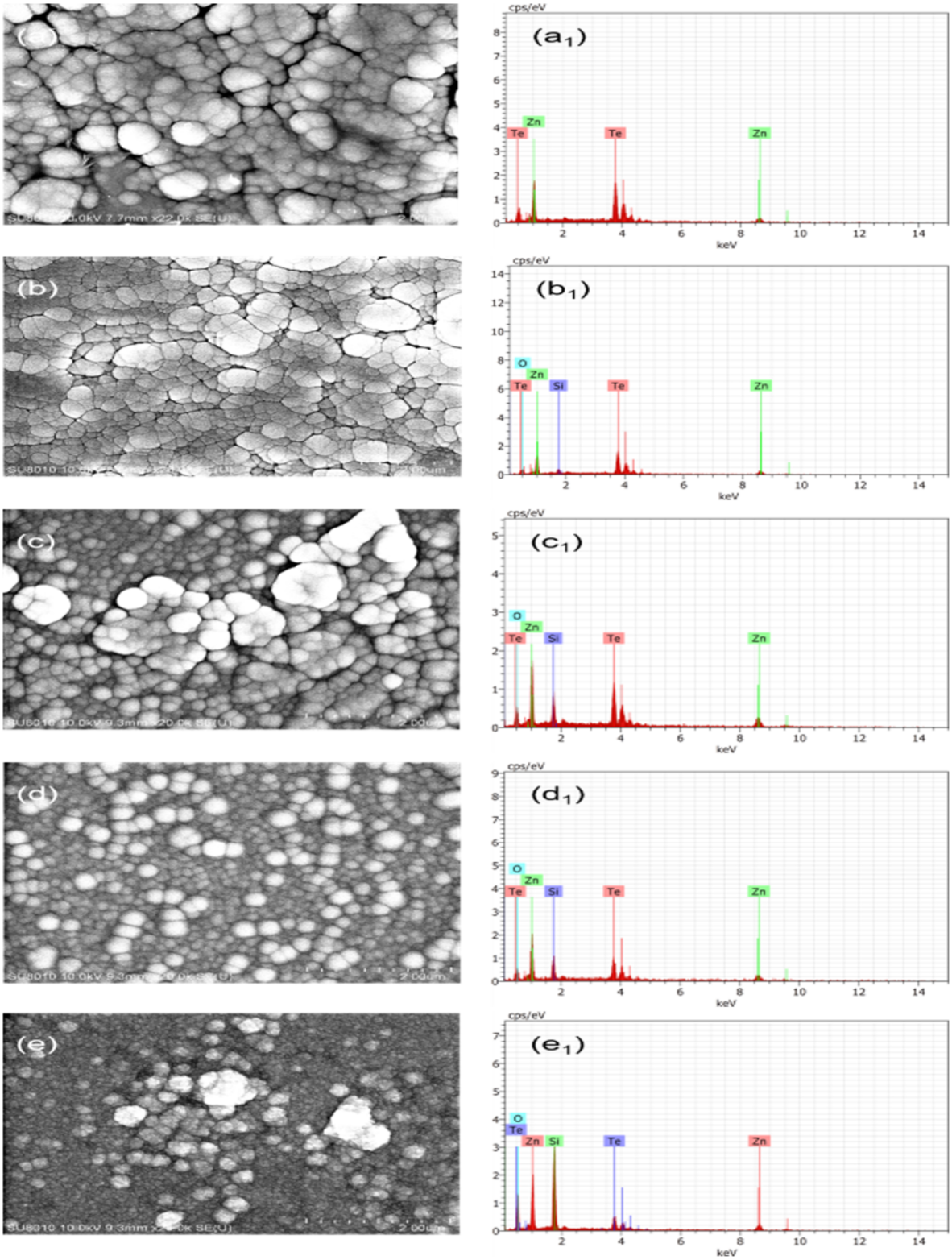

Figure 4: FESEM micrographs (a–e) and EDS spectra (a_1–e_1) of ZnTe films deposited at (a, a_1) R.T., (b, b_1) 300 °C, (c, c_1) 400 °C, (d, d_1) 500 °C, and (e, e_1) 600 °C. (The scale bars are 2 µm).

Table 4: Elemental composition of ZnTe films obtained from EDS.

Element	R.T.	300 °C	400 °C	500 °C	600 °C
Zn (atom %)	50.47	45.14	43.54	44.02	22.58
Te (atom %)	49.53	36.33	22.09	17.65	5.43
Si (atom %)	—	7.22	15.84	17.83	32.45
O (atom %)	—	11.31	18.54	20.50	39.54

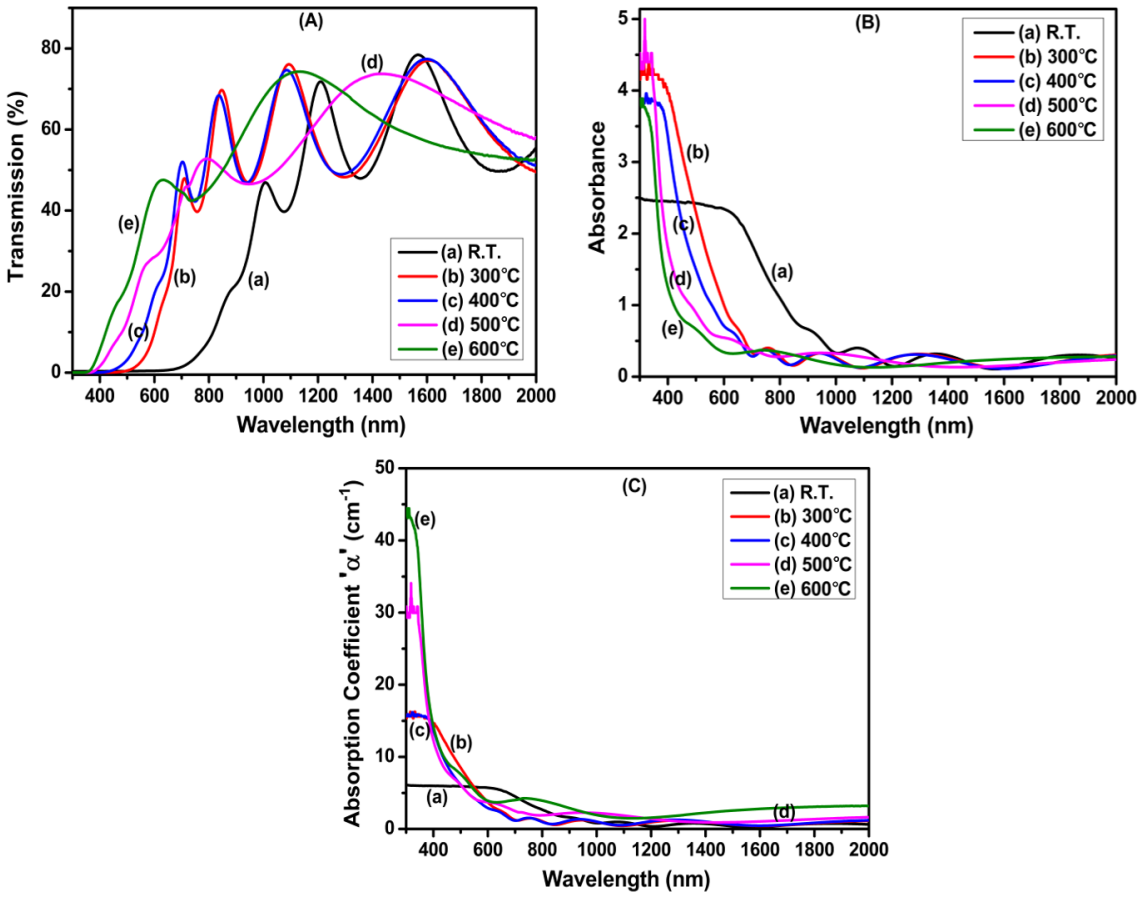

Figure 5: Variation in (A) transmittance, (B) absorbance, and (C) absorption coefficient with wavelength of ZnTe films produced at (a) R.T. and substrate temperatures of (b) 300 °C, (c) 400 °C, (d) 500 °C, and (e) 600 °C.

From the transmittance spectra, it has been found that the films deposited at room temperature exhibit transparency in the NIR region only. Whereas the films deposited at higher substrate temperatures exhibits transparency in both visible and NIR regions. Further, it is observed that the average transmittance of the films increases with increasing substrate temperature, which may be because of the higher crystallinity of films with increasing substrate temperature. The enhancement of transmittance in the vis–NIR region with increasing substrate temperature indicates a possible application of these films in optoelectronic devices. The variation in absorbance with wavelength for ZnTe films deposited at different substrate temperatures is presented in Figure 5B. It has been found that the films exhibit maximum absorbance in the visible region, which later decreases with the increase in wavelength. This decrease in absorbance with wavelength may be due to interband electronic transitions between the conduction band and ionized donor levels.

The absorbance was also found to decrease with increasing substrate temperature. This is due to the increase in the transparency of films with increasing substrate temperature. A blue shift in the absorption edge was observed with increasing tem-

perature. The absorption coefficient (α) for the produced films was determined from the transmittance spectra using the relation [34]

$$\alpha = \frac{1}{t}\ln\left(\frac{1}{T}\right), \tag{8}$$

where T is the transmittance and t represents the thickness of films, which is about 940 ± 0.53 nm, 623 ± 0.16 nm, 563 ± 0.02 nm, 337 ± 0.02 nm, and 200 ± 0.30 nm for films deposited at R.T., 300 °C, 400 °C, 500 °C, and 600 °C, respectively.

Figure 5C shows the absorption coefficient as a function of the wavelength for ZnTe/Qz films at different substrate temperatures. From Figure 5C, it is observed that α has very low values at higher wavelengths (≥600 nm). The absorption coefficient increases very slowly in this region. In contrast, a sharp increase in α is observed in the lower-wavelength (≤600 nm) region. This type of variation in absorption coefficient points toward the existence of both direct and indirect bandgaps in a material. ZnTe films exhibit both direct and indirect transitions [35,36]. Therefore, in this study we have determined both direct and indirect bandgaps.

The Tauc relation was used to determine the optical bandgaps (E_g) of ZnTe/Qz films [34]

$$\alpha h\nu = C\left(h\nu - E_g\right)^m, \tag{9}$$

where h represents the Planck constant, ν is the frequency of the incident light, α is the absorption coefficient, and C is an energy-independent constant. The value of the power exponent m depends on the type of transition in the films. For a direct allowed transition, m takes a value of 1/2. Figure 6 (left Y-axis scale, Figure 6A(a,b,c) and Figure 6B(d,e)) shows the $(\alpha h\nu)^2$-vs-$h\nu$ graph for ZnTe films deposited at different substrate temperatures. For obtaining E_g, the linear portion of the graph was extrapolated onto the x-axis. The intercept on the x-axis gives the optical bandgap value. The direct optical bandgap value for the film deposited at room temperature was found to be 1.47 eV, which is much less than that of the bulk counterpart, which is 2.26 eV. This may be due to the presence of a high density of localized states present near the band edge, which was confirmed by GXRD results. Further, the direct optical bandgap value increases from 2.19 eV at 300 °C to 3.11 eV at 600 °C. The increase in the direct bandgap value with substrate temperature is assigned to the enhancement in crystallinity and decrease in dislocation density in the films [15].

For indirect allowed transitions, m = 2. Figure 6 (right Y-axis scale, A(a′, b′, c′) and B(d′, e′)) shows the $(\alpha h\nu)^{1/2}$-vs-hv plot for ZnTe films deposited at different substrate temperatures. The linear portion of the graph was extrapolated to find the bandgap values. The indirect bandgap also increases, from 0.98 eV at R.T. to 2.63 eV at 600 °C, with the rise in substrate temperature. Pal et al. reported changes in direct and indirect bandgap values of ZnTe thin films with varying thickness [35]. However, the changes we observed for direct bandgaps (1.47–3.11 eV) and indirect bandgaps (0.98–2.63 eV) are more significant.

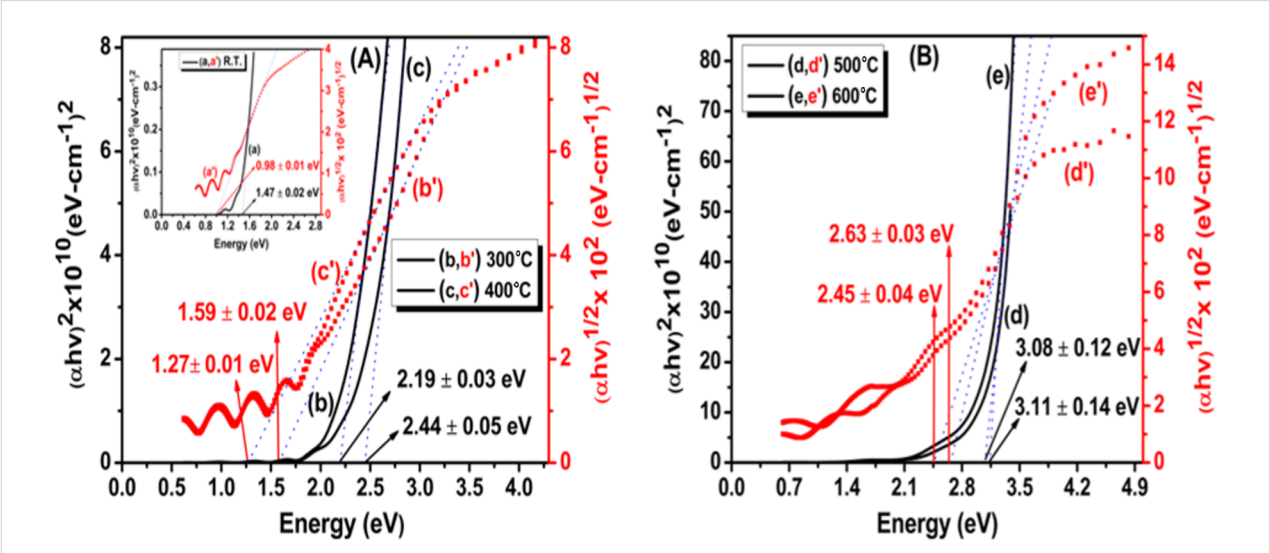

Figure 6: Tauc plots for direct bandgap (left Y-axis scale, a–e) and indirect bandgap (right Y-axis scale, a′–e′) calculation of ZnTe films fabricated at (A) RT (a, a′) (displayed in inset), 300 °C (b, b′), 400 °C (c, c′); (B) 500 °C (d, d′) and 600 °C (e, e′). R^2 = 0.99.

The existence of both direct and indirect bandgaps in a material has implications regarding the efficiency of solar cells. The efficiency of solar cells can be increased if most of the incident photons are absorbed by the absorbing layer and used in charge carrier generation. For this, a large thickness is required in solar cell construction. But thickness has a negative effect on the efficiency because the diffusion length of minority carriers is short for large thickness; thus, not every charge carrier that is generated will participate in conduction. Direct-bandgap materials also have a very short diffusion length of minority carriers, while the diffusion length of minority carriers is very long for the indirect-bandgap materials. Therefore, the best choice is a material having both direct and indirect bandgaps along with some localized states for photon absorption and charge carrier generation [36]. The existence of both direct and indirect bandgaps and their tuneable nature with substrate temperature point toward the application of the fabricated ZnTe films in solar cells.

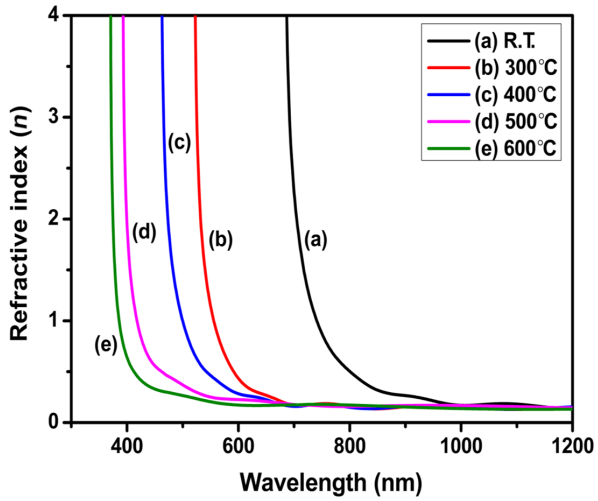

Figure 7: Variation in refractive index (n) with wavelength of ZnTe films deposited at (a) R.T. and substrate temperatures of (b) 300 °C, (c) 400 °C, (d) 500 °C, and (e) 600 °C.

Refractive index

The refractive index is one of the important optical parameters as it is connected to the electronic polarizability, local fields in the semiconducting material, and transmission. The refractive index is related to the transmission of films through the relation [37]

$$n = \frac{1}{T} + \left(\frac{1}{T-1}\right)^{1/2}, \tag{10}$$

where T represents the transmission in percent. Figure 7 shows the variation in refractive index with wavelength for films fabricated at various substrate temperatures (R.T.–600 °C). The change in the refractive index shows a normal dispersion behaviour. The refractive index has a high value in the lower-wavelength region. It decreases sharply and becomes nearly constant in the higher-wavelength region. This is because, at lower wavelengths, the absorption capacity of a material is high, which results in a decrease in the speed of light, thus increasing the value of n. The refractive index value is also found to decrease with increasing substrate temperature. This may be due to the enhancement in crystallinity and decrement in dislocation density with substrate temperature.

This variation in refractive index value is also associated with the optical bandgap according to the Harve–Vandamme model [38]

$$n^2 = 1 + \left(\frac{A}{E_g + B}\right)^2, \tag{11}$$

where A (= 13.6 eV) and B (= 3.4 eV) are constants, and E_g represents the direct bandgap. Using this formula, the refractive index has been calculated. The refractive index value decreases from 2.96 at R.T. to 2.31 at 600 °C because of the bandgap increment [39]. The dielectric constant and the dielectric loss of the deposited ZnTe films exhibit a similar pattern and were also found to decrease with increasing substrate temperature (see below).

Photoluminescence studies

Photoluminescence (PL) studies were carried out to analyse the films' electronic features. The photoluminescence occurs when a material absorbs energy higher than its bandgap. In a semiconductor, this leads to the creation of a large number of electrons and holes in comparison to their equilibrium concentration. These generated charge carriers recombine after thermal relaxation, and photons with energy lower than the excitation photon energy are emitted. The recombination can occur either from band to band or through impurities and defects present within an energy level inside the forbidden gap. Grain boundaries are responsible for non-radiative recombination processes. For the present analysis, the PL spectra of the ZnTe films were recorded at room temperature using an excitation wavelength of 320 nm from a Xenon arc lamp. Figure 8 shows the PL spectra of ZnTe films deposited at different substrate temperatures. A strong and broad emission spectrum is observed for all film samples in the wavelength range from 420 to 453 nm, with shoulders at 413 and 476 nm. With the increase in substrate temperature (400–600 °C), an additional peak at 563 nm appears. A red shift in the emission peaks is observed at higher substrate temperatures compared to the spectrum of the room-

temperature sample. The peaks observed in the emission spectra are accredited to deep and shallow band transitions. The variation in the width of emission peaks may be due to the change in the lattice environment with substrate temperature. The photoluminescence intensity depends on the number of charge carriers that undergo direct band-to-band recombination [40]. The PL intensity decreases with an increase in substrate temperature (300–600 °C). This may be because ZnTe exhibits both direct and indirect bandgaps. The direct bandgap increases with substrate temperature as shown in our bandgap studies. Therefore, the possibility for indirect transition increases with an increase in substrate temperature, which leads to a decrease in PL intensity with substrate temperature. The decrease in PL intensity corroborates our structural and morphological studies, where it was found that both dislocation density and particle density decrease with increasing substrate temperature [40].

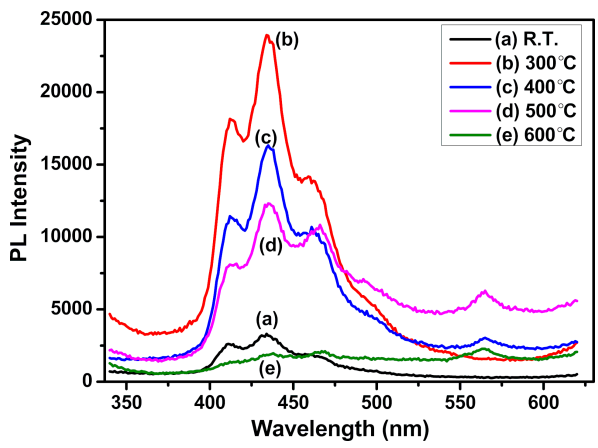

Figure 8: Photoluminescence spectra of ZnTe films deposited at (a) room temperature (R.T.) and substrate temperatures of (b) 300 °C, (c) 400 °C, (d) 500 °C, and (e) 600 °C.

Electrical studies

Figure 9 depicts the current–voltage (*I–V*) characteristics of ZnTe films deposited at different substrate temperatures. The *I–V* characteristics were recorded using a two-probe arrangement provided with a Keithley 4200 SCSA parametric analyser. For this, equally spaced ohmic contacts were made on the surface of the films using silver paste. The characteristics were recorded in the voltage range from −1 V to 1 V. The *I–V* characteristics are nearly linear and regular in both positive and negative voltage regions. This points towards a nearly ohmic contact between ZnTe film and quartz substrate, which is necessary for the fabrication of the optoelectronic device.

The conductivity (σ) of films was determined using the relation [41]

$$\sigma = \left(\frac{1}{\rho}\right) = \left(\frac{l}{A \times R}\right), \quad (12)$$

where ρ is the electrical resistivity, R is the resistance of the film, A is the area of ZnTe film samples (width of film × thickness of film), and l corresponds to the distance between the probes (1 cm) while taking the measurement. The measured values of resistance, resistivity, and conductivity are presented in Table 5. The conductivity of the ZnTe films increases (from 1.42×10^{-8} to 6.02×10^{-4} $\Omega^{-1}\cdot cm^{-1}$) with increasing substrate temperature (from 300 to 600 °C). The increase in mobility, variation in charge carrier concentration, and enhancement in the crystallinity of the films with increasing substrate temperature might be the possible reason behind the increase in conductivity of films with substrate temperature [42].

Grain boundaries have a significant effect on the electric transport properties in polycrystalline films. Grain boundaries are growth process-dependent phenomena and have a large number of charge-trapping centres. Thus, grain boundaries reduce the mobility of charge carriers, and various scattering events take place at grain boundaries such that the conductivity of the films decreases. The number of grain boundaries decreases with an increase in crystallite size. Thus, the increase in crystallinity and decrease in dislocation density with substrate temperature might be the possible reasons for an increase in the conductivity of films. To understand the dependence of the electrical properties of films on different parameters, it is essential to measure the electrical properties of grain boundaries.

Conclusion

In this work, the effect of substrate temperature on various properties of RF-sputtered ZnTe films was investigated systematically. The structural investigations using GXRD revealed that the films are polycrystalline with cubic zincblende structure. The crystallite size increases (from 37.60 to 68.88 Å) with increasing substrate temperature (300–600 °C). The crystallite size was found to be maximum for the film produced at 600 °C. Optical studies revealed that the average transmittance of ZnTe films increases with substrate temperature. A blue shift in the bandgap was observed with increasing substrate temperature. Taking into account the possibility for indirect transitions, the indirect bandgap for ZnTe films was calculated. Morphological investigation revealed that the roughness increases and the particle density decreases with the increase in substrate temperature. The electrical conductivity was found to increase (from 1.42×10^{-8} to 6.06×10^{-4} $\Omega^{-1}\cdot cm^{-1}$) with the increase in substrate temperature (300–600 °C). The observed large bandgap (3.11 eV), high transmittance, large crystallite size (68.88 Å) and high conductivity of the ZnTe film produced at 600 °C indi-

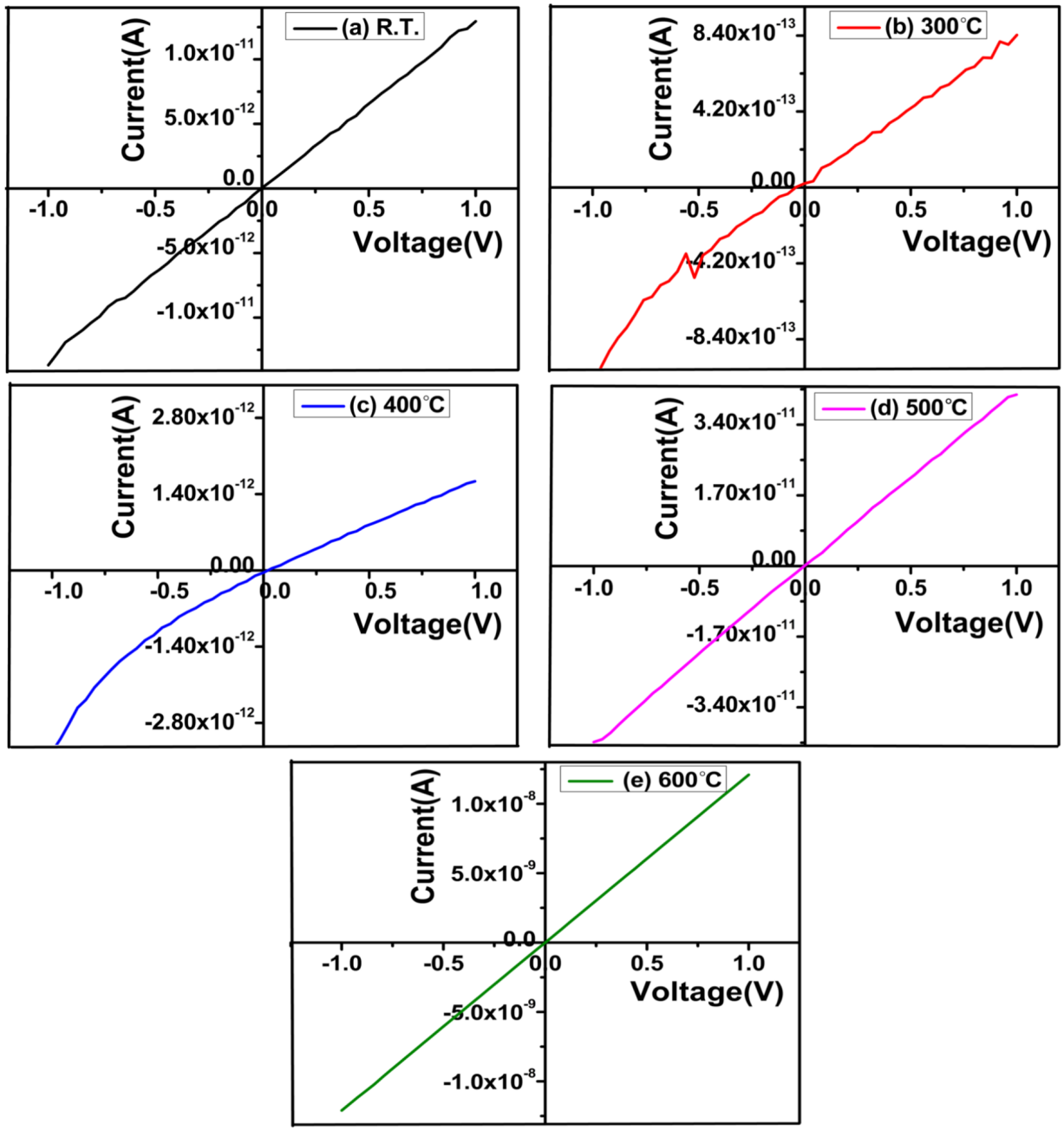

Figure 9: *I–V* characteristics of ZnTe films deposited at different substrate temperatures in the range of R.T.–600 °C.

Table 5: Variation in resistance, resistivity, and conductivity of ZnTe films deposited at various substrate temperatures.

Substrate temperature (°C)	Resistance (Ω)	Resistivity (Ω·cm)	Conductivity ($\Omega^{-1}\cdot cm^{-1}$)
R.T.	7.63×10^{10}	7.20×10^{6}	1.39×10^{-7}
300	1.13×10^{12}	7.04×10^{7}	1.42×10^{-8}
400	5.20×10^{11}	2.93×10^{7}	3.41×10^{-8}
500	2.35×10^{10}	7.94×10^{5}	1.26×10^{-6}
600	8.25×10^{7}	1.66×10^{3}	6.02×10^{-4}

cate a possible application of such films as a buffer layer in solar cells.

Supporting Information

Supporting Information File 1

Additional data on optical measurements.
[https://www.beilstein-journals.org/bjnano/content/supplementary/2190-4286-16-25-S1.pdf]

Acknowledgements

The authors acknowledge the Department of Physics, (Deenbandhu Chhotu Ram University Of Science And Technology) DCRUST, Murthal for providing PL facilities.

Funding

One of the authors (Kafi Devi) thanks the University Grant Comission (UGC), New Delhi for providing a (UGC-JRF) fellowship. The authors are greatful to the Department of Science and Technology (DST), New Delhi for providing funds for 200 kV ion accelerator and related characterization facilities at Kurukshetra University. The authors are also thankful to the Ministry of Human Resource and Development (MHRD), New Delhi for RUSA 2.0 grants to the Center for Advanced Material Research (CAMR), Kurukshetra University.

Author Contributions

Kafi Devi: conceptualization; formal analysis; investigation; methodology; visualization; writing – original draft. Usha Rani: investigation; methodology; writing – original draft. Arun Kumar: investigation; methodology; validation; writing – review & editing. Divya Gupta: conceptualization; investigation; validation; visualization; writing – review & editing. Sanjeev Aggarwal: conceptualization; supervision; validation; visualization; writing – review & editing.

ORCID® iDs

Usha Rani - https://orcid.org/0009-0007-8584-0189
Sanjeev Aggarwal - https://orcid.org/0000-0002-0054-4679

Data Availability Statement

Data generated and analyzed during this study is available from the corresponding author upon reasonable request.

References

1. Kim, T.; Kim, K.-H.; Kim, S.; Choi, S.-M.; Jang, H.; Seo, H.-K.; Lee, H.; Chung, D.-Y.; Jang, E. *Nature* **2020,** *586,* 385–389. doi:10.1038/s41586-020-2791-x
2. Ferahtia, S.; Saib, S.; Bouarissa, N.; Benyettou, S. *Superlattices Microstruct.* **2014,** *67,* 88–96. doi:10.1016/j.spmi.2013.12.021
3. Nishio, M.; Saito, K.; Nakatsuru, Y.; Shono, T.; Matsuo, Y.; Tomota, A.; Tanaka, T.; Guo, Q. X. *J. Cryst. Growth* **2017,** *468,* 666–670. doi:10.1016/j.jcrysgro.2017.01.030
4. Rao, G. K.; Bangera, K. V.; Shivakumar, G. K. *Mater. Res. Bull.* **2010,** *45,* 1357–1360. doi:10.1016/j.materresbull.2010.06.050
5. Kashyout, A. B.; Aricò, A. S.; Antonucci, P. L.; Mohamed, F. A.; Antonucci, V. *Mater. Chem. Phys.* **1997,** *51,* 130–134. doi:10.1016/s0254-0584(97)80281-7
6. Uličná, S.; Isherwood, P. J. M.; Kaminski, P. M.; Walls, J. M.; Li, J.; Wolden, C. A. *Vacuum* **2017,** *139,* 159–163. doi:10.1016/j.vacuum.2017.01.001
7. Lin, J. S.; Wei, S. S.; Yu, Y. T.; Hsu, C. H.; Kao, W. H.; Chen, W. S.; Tseng, C. F.; Lai, C. H.; Lu, J. M.; Ju, S. P. *Adv. Mater. Res.* **2013,** *690–693,* 569–572. doi:10.4028/www.scientific.net/amr.690-693.569
8. Nakasu, T.; Sun, W.; Kobayashi, M.; Asahi, T. *J. Cryst. Growth* **2017,** *468,* 635–637. doi:10.1016/j.jcrysgro.2016.11.035
9. Pattar, J.; Sawant, S. N.; Nagaraja, M.; Shashank, N.; Balakrishna, K. M.; Sanjeev, G.; Mahesh, H. M. *Int. J. Electrochem. Sci.* **2009,** *4,* 369–376. doi:10.1016/s1452-3981(23)15147-9
10. Ibrahim, A. A.; El-Sayed, N. Z.; Kaid, M. A.; Ashour, A. *Vacuum* **2004,** *75,* 189–194. doi:10.1016/j.vacuum.2004.02.005
11. Erlacher, A.; Lukaszew, A. R.; Jaeger, H.; Ullrich, B. *Surf. Sci.* **2006,** *600,* 3762–3765. doi:10.1016/j.susc.2006.02.061
12. Lin, X.; Zhang, Y.; Zhu, Z.; Wu, Q.; Liu, X. *Chem. Phys. Lett.* **2021,** *767,* 138358. doi:10.1016/j.cplett.2021.138358
13. Bellakhder, H.; Outzourhit, A.; Ameziane, E. L. *Thin Solid Films* **2001,** *382,* 30–33. doi:10.1016/s0040-6090(00)01697-7
14. Isik, M.; Gullu, H. H.; Parlak, M.; Gasanly, N. M. *Phys. B (Amsterdam, Neth.)* **2020,** *582,* 411968. doi:10.1016/j.physb.2019.411968
15. Bacaksiz, E.; Aksu, S.; Ozer, N.; Tomakin, M.; Özçelik, A. *Appl. Surf. Sci.* **2009,** *256,* 1566–1572. doi:10.1016/j.apsusc.2009.09.023
16. Rakhshani, A. E. *Thin Solid Films* **2013,** *536,* 88–93. doi:10.1016/j.tsf.2013.03.136
17. Erdoğan, E.; Kundakçı, M. *Microelectron. Eng.* **2019,** *207,* 15–18. doi:10.1016/j.mee.2018.12.010
18. Boulegane, A.; Guittoum, A.; Hadj Larbi, A.; Laggoun, A.; Boudissa, M. *Appl. Phys. A: Mater. Sci. Process.* **2024,** *130,* 361. doi:10.1007/s00339-024-07516-5
19. Basak, A.; Hati, A.; Mondal, A.; Singh, U. P.; Taheruddin, S. K. *Thin Solid Films* **2018,** *645,* 97–101. doi:10.1016/j.tsf.2017.10.039
20. Asare, J.; Agyei-Tuffour, B.; Amonoo, E. A.; Dodoo-Arhin, D.; Nyankson, E.; Mensah, B.; Oyewole, O. O.; Yaya, A.; Onwona-Agyeman, B. *Cogent Eng.* **2020,** *7,* 1829274. doi:10.1080/23311916.2020.1829274
21. Hasani, E.; Kamalian, M.; Gholizadeh Arashti, M.; Babazadeh Habashi, L. *J. Electron. Mater.* **2019,** *48,* 4283–4292. doi:10.1007/s11664-019-07204-8
22. Das, S.; Paikaray, S.; Swain, I.; Senapati, S.; Naik, R. *Surf. Interfaces* **2023,** *42,* 103395. doi:10.1016/j.surfin.2023.103395
23. Dalouji, V. *Heliyon* **2024,** *10,* e37509. doi:10.1016/j.heliyon.2024.e37509
24. Devi, K.; Singh, G.; Kumar, A.; Gupta, D.; Aggarwal, S. *Integr. Ferroelectr.* **2024,** in press.

25. Lakmal, A. A. I.; Kumarasinghe, R. K. K. G. R. G.; Seneviratne, V. A.; Chen, J.-Y.; Song, J.-M.; Dassanayake, B. S. *Mater. Sci. Eng., B* **2021,** *273,* 115406. doi:10.1016/j.mseb.2021.115406
26. Punitha, K.; Sivakumar, R.; Sanjeeviraja, C.; Ganesan, V. *Appl. Surf. Sci.* **2015,** *344,* 89–100. doi:10.1016/j.apsusc.2015.03.095
27. Suthar, D.; Himanshu; Patel, S. L.; Chander, S.; Kannan, M. D.; Dhaka, M. S. *J. Mater. Sci.: Mater. Electron.* **2021,** *32,* 19070–19082. doi:10.1007/s10854-021-06424-1
28. Das, N. K.; Chakrabartty, J.; Farhad, S. F. U.; Sen Gupta, A. K.; Ikball Ahamed, E. M. K.; Rahman, K. S.; Wafi, A.; Alkahtani, A. A.; Matin, M. A.; Amin, N. *Results Phys.* **2020,** *17,* 103132. doi:10.1016/j.rinp.2020.103132
29. Goyal, S.; Chauhan, R. P. *J. Mater. Sci.: Mater. Electron.* **2019,** *30,* 1345–1353. doi:10.1007/s10854-018-0402-5
30. Singh, H.; Singh, M.; Singh, J.; Bansod, B. S.; Singh, T.; Thakur, A.; Wani, M. F.; Sharma, J. *J. Mater. Sci.: Mater. Electron.* **2019,** *30,* 3504–3510. doi:10.1007/s10854-018-00627-9
31. Sharma, N.; Prabakar, K.; Ilango, S.; Dash, S.; Tyagi, A. K. *Appl. Surf. Sci.* **2015,** *347,* 875–879. doi:10.1016/j.apsusc.2015.04.151
32. Ghosh, K.; Pandey, R. K. *Phys. Scr.* **2019,** *94,* 115704. doi:10.1088/1402-4896/ab292c
33. Kuznetsova, Y. A.; Zatsepin, A. F.; Gavrilov, N. V. *Opt. Mater. (Amsterdam, Neth.)* **2021,** *120,* 111382. doi:10.1016/j.optmat.2021.111382
34. Singh, H.; Duklan, N.; Singh, T.; Thakur, A.; Sharma, J. *J. Mater. Sci.: Mater. Electron.* **2018,** *29,* 4992–4998. doi:10.1007/s10854-017-8460-7
35. Pal, U.; Saha, S.; Chaudhuri, A. K.; Rao, V. V.; Banerjee, H. D. *J. Phys. D: Appl. Phys.* **1989,** *22,* 965–970. doi:10.1088/0022-3727/22/7/014
36. Shalaan, E.; Ibrahim, E.; Al-Marzouki, F.; Al-Dossari, M. *Appl. Phys. A: Mater. Sci. Process.* **2020,** *126,* 852. doi:10.1007/s00339-020-04045-9
37. Das, S.; Priyadarshini, P.; Alagarasan, D.; Vardhrajperumal, S.; Ganesan, R.; Naik, R. *J. Non-Cryst. Solids* **2022,** *592,* 121742. doi:10.1016/j.jnoncrysol.2022.121742
38. Chander, S.; Dhaka, M. S. *J. Mater. Sci.: Mater. Electron.* **2016,** *27,* 11961–11973. doi:10.1007/s10854-016-5343-2
39. Kumar, B. R.; Hymavathi, B.; Rao, T. *Chalcogenide Lett.* **2014,** *11,* 509–517.
40. Kosyak, V.; Opanasyuk, A.; Bukivskij, P. M.; Gnatenko, Y. P. *J. Cryst. Growth* **2010,** *312,* 1726–1730. doi:10.1016/j.jcrysgro.2010.02.034
41. Javed, A.; Khan, N.; Bashir, S.; Ahmad, M.; Bashir, M. *Mater. Chem. Phys.* **2020,** *246,* 122831. doi:10.1016/j.matchemphys.2020.122831
42. Rao, G. K.; Bangera, K. V.; Shivakumar, G. K. *Vacuum* **2009,** *83,* 1485–1488. doi:10.1016/j.vacuum.2009.06.047

License and Terms

BEILSTEIN JOURNAL OF NANOTECHNOLOGY

Quantification of lead through rod-shaped silver-doped zinc oxide nanoparticles using an electrochemical approach

Ravinder Lamba[1,2], Gaurav Bhanjana[2], Neeraj Dilbaghi[2], Vivek Gupta[*1] and Sandeep Kumar[*3]

Full Research Paper

Open Access

Address:
[1]Department of Physics, Guru Jambheshwar University of Science and Technology, Hisar-Haryana, 125001, India, [2]Department of Bio and Nano Technology, Guru Jambheshwar University of Science and Technology, Hisar-Haryana, 125001, India and [3]Department of Physics, Punjab Engineering College (Deemed to be University), Chandigarh, 160012, India

Email:
Vivek Gupta[*] - vivekgupta.skgt@gmail.com; Sandeep Kumar[*] - ksandeep36@yahoo.com

* Corresponding author

Keywords:
electrochemical methods; chemical sensor; doping; lead; nanoparticles; ZnO nanorods

Beilstein J. Nanotechnol. **2025,** *16,* 422–434.
https://doi.org/10.3762/bjnano.16.33

Received: 05 October 2024
Accepted: 26 February 2025
Published: 26 March 2025

This article is part of the thematic issue "Low-dimensional nanomaterials for sustainable applications".

Associate Editor: P. Ayala

Abstract

Special features of zinc oxide nanoparticles have drawn a lot of interest due to their wide bandgap, high surface area, photocatalytic activity, antimicrobial activity, and semiconductor properties. By doping ZnO nanoparticles with transition metals, we can alter their electrical, optical, and magnetic properties by introducing new electronic states into the band structure. Herein, Ag is added to ZnO nanostructures to improve their optical properties to detect heavy metal lead ions. The prepared lead sensor with ultrahigh sensitivity, based on silver-doped ZnO nanorods (Ag@ZnO NRs), was fabricated and characterized. The morphological, structural, compositional, and optical characteristics of the Ag@ZnO NRs were investigated using a variety of methods after they were fabricated using a low-temperature co-precipitation method. The resulting Ag@ZnO NRs had good optical properties, nanorod morphologies, and high crystallinity with no impurities. Technological advancements are leading people to use lightweight electronics and affordable sensors. Electrochemical techniques comparatively offer quick, portable, sensitive, and inexpensive basic equipment for heavy metal detection. The interactions between Ag@ZnO NRs and lead were studied using electrochemical methods. The prepared lead sensor using Ag@ZnO NRs show a very low detection limit and a very high sensitivity toward lead. The lead chemical sensor that was developed had a detection limit of 3 ppm with a sensitivity of 16 $\mu A \cdot ppm^{-1} \cdot cm^{-2}$. The recorded reaction time of lead sensor was less than two seconds.

Introduction

According to the literature, a lot of work has been done to create durable and dependable smart sensors for the effective identification of analytes that are harmful but also crucial for the environment and technology [1]. Even at very low levels, heavy metals can permanently harm health, and their acute exposure leads to chronic disorders by affecting organ func-

tions [2]. For example, lead poisoning in liquid effluents, is one of the worst environmental hazards which can affect human health and readily impact immune responses [3]. Due to the detrimental effects on the environment and human health, determining the presence of trace heavy metals is crucial. Lead is a highly toxic element that affects human soft tissues and organs, acting in concert with other carcinogens to cause cancer in the kidneys, lungs, or brain. Lead paint, lead-containing petrol, mining, and smelting are some of the sources of lead exposure [4]. Through contaminated food or drink or through mouth-to-mouth contact, lead can enter the body. Standard techniques for determining lead content involve the use of atomic absorption spectroscopy (AAS) [5] and inductively coupled plasma–mass spectrometry (ICP–MS) [6]. Although both techniques yield reliable results in matrices as complicated as serum or blood, they require costly, large-scale equipment as well as highly skilled operators. Furthermore, these methods are not as desired or even appropriate for point-of-care (POC) use because of the considerable time delays caused by the shipment of samples to centralized laboratories. Miniaturization is made possible by electrochemical procedures for determining heavy metals, which need a comparatively simple apparatus. Thus, it is imperative to develop low-cost, miniaturized analytical instruments to monitor hazardous chemical substances [7,8]. Target detection in real time is a strong suit for electrochemical devices. Electron mediators are typically used to modify the working electrodes in electrochemical sensor fabrication. These days, due to their unique electrical and optical characteristics, nanomaterials are employed as effective electron mediators [9].

Zinc oxide nanoparticles have gained a lot of attention due to their unique features, such as wide bandgap (approximately 3.37 eV), excellent electron transportation, piezoelectric behavior, semiconductor nature, low toxicity, and enhanced electrochemical response, and have a vast range of uses. Zinc oxide shows excellent features, such as nanoscale particles, highly crystalline nature, tunable shape, size and density, and a high aspect ratio. In summary, ZnO nanoparticles offer a versatile platform for technological advancements across fields such as medicine, electronics, environmental remediation, and energy [10,11]. The use of certain metal dopants to modify the chemical, optical, and electrical features of a material has gained considerable interest in the realm of semiconductor technology. A recent study has conducted thorough investigations into the effects of transition metal ions, such as silver, copper, nickel, and manganese on the chemical and physical properties of ZnO nanoparticles. These metal dopants utilize their partially occupied d-electron shells, leading to the presence of unpaired electrons. Out of these metals, silver is particularly well-suited for ZnO doping because of its notable characteristics, including strong conductivity, solubility, favorable ionic size, and low orbital energy. These features contribute to the improvement of optical and electrical characteristics of ZnO. The incorporation of silver boosts the mobility of oxygen on the surface by means of the formation of oxygen vacancies, leading to enhanced catalytic activity. Also, the small doping of Ag introduces more active sites on the catalyst surface, potentially improving the overall catalytic activity [12,13]. This study demonstrates an efficient and uncomplicated method for producing Ag@ZnO NRs. These fabricated Ag@ZnO NRs play an effective role as an electron mediator in the development of lead chemical sensors which are both highly sensitive and robust in nature. Based on our current understanding, the lead sensor we developed exhibits the most notable sensitivity among all.

Results and Discussion

X-ray diffraction of as-synthesized Ag@ZnO nanorods

The Ag@ZnO NRs were analyzed for their crystal phases by evaluating the X-ray diffraction pattern. Figure 1a displays the diffraction pattern of the Ag@ZnO NRs that were formed. It was observed that this pattern closely corresponds to the data that has already been reported [14]. The distinct reflections indicate the high degree of crystalline nature of the nanorods that were created. Ag@ZnO NRs have a hexagonal wurtzite structure with space group 186: $P6_3mc$. The lattice is primitive with dimensions $a = b = 0.32488$ nm and $c = 0.52001$ nm. The peaks in this pattern are detected at specific angles, denoted as 2θ, which are 31.79°, 34.48°, 36.27°, 47.55°, 56.62°, 62.92°, 66.43°, 67.95°, 69.07°, 72.58°, 77.02°, 81.54°, and 89.69°. These angles correspond to the lattice planes (100), (002), (101), (102), (110), (103), (200), (112), (201), (004), (202), (104), and (203) respectively. The pattern of Ag-doped ZnO nanoparticles exhibits three additional diffraction peaks at 2θ values of 38.29°, 44.39°, and 64.58°. These peaks are associated with the metallic FCC phase of Ag. Ag doping at the substitution sites of the ZnO crystal lattice results in a decrement in the peak position values because Ag^+ ion (12.2 nm) has a larger ionic size compared to that of the Zn^{2+} ion (7.4 nm). Consequently, the given data aligns with the decrease in the highest location of the point, indicating a reduction in the *c*-axis lattice. This implies that the Ag ion has filled the spaces between the atoms in the ZnO structure. Also, Ag functions as an amphiprotic dopant, meaning it can both donate and accept protons. It tends to occupy interstitial sites and also substitute for Zn [15,16]. Debye–Scherrer's relation is used to calculate the average crystallite size of the Ag@ZnO NRs:

$$D = \frac{0.9\lambda}{\beta \cos\theta},$$

where λ = 1.54 Å (wavelength of the Kα radiation of Cu), β = full width at half maximum, and θ = peak position. The average crystal size of Ag@ZnO NRs is found to be approximately 28 nm.

The dislocation density (δ) of the crystalline material expressed as $\delta = 1/D^2$ is 0.001275. The total broadening of the peak (β_T) caused by the crystalline size and strain in the lattice is given by:

$$\beta_T = \beta_D + \beta_\varepsilon,$$

where β_D is broadening of the peak due to crystal size and β_ε is broadening due to lattice strain. For analyzing stress and strain resulting from X-ray diffraction, Williamson and Hall's approach is the simplest method. The peak broadening resulting from the lattice strain can be obtained by the Stokes–Wilson relation:

$$\beta_\varepsilon = \varepsilon \tan\theta,$$
$$\beta_T = \frac{k\lambda}{D\cos\theta} + \frac{4\varepsilon\sin\theta}{\cos\theta}.$$

By plotting $\beta_T\cos\theta$ as a function of $4\sin\theta$ as shown in Figure 1b, we get the value of ε = 0.00195, and the intercept = $k\lambda/D$ = 0.00193.

This plotted straight line using a W–H plot is a good fit as the correlation coefficient value of R^2 is 0.96. Using the value of the intercept, the calculated size of the nanoparticle is found to be 71.8 nm. The value of the crystalline size obtained by the Williamson–Hall method is 2.5 times than that obtained by the Scherrer method. This difference is proportional to the strain value [17].

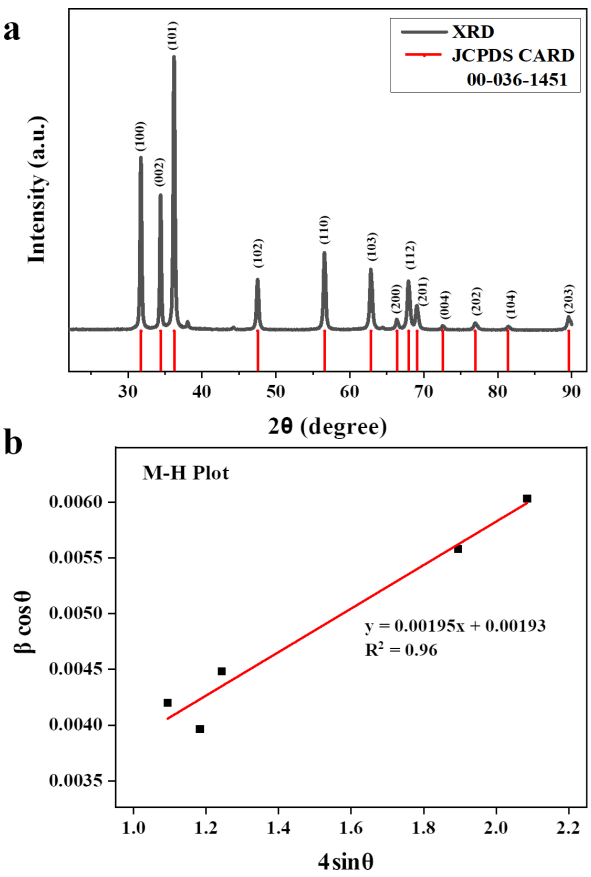

Figure 1: (a) XRD of Ag@ZnO NRs and (b) M–H plot of Ag@ZnO NRs.

Field-emission scanning electron microscopy of Ag@ZnO nanorods

The general morphological characteristics of the as-obtained nanorods were analyzed by electron microscopy. Figure 2a depicts the typical field-emission scanning electron microscopy (FESEM) image of the as-obtained nanomaterials. The produced nanomaterials had rod-shaped morphologies and were grown at extremely high densities, as seen by the SEM image. Figure 2b represents the average diameter of Ag@ZnO NRs which was calculated using the Image J software. The average diameter of Ag@ZnO NRs is approximately 70 nm. The elemental composition of the fabricated nanorods was examined through energy-dispersive spectroscopy (EDS). Figure 2c depicts the typical EDS spectrum of the produced Ag@ZnO NRs. Observations from the EDS spectrum lead to the conclusion that the nanorods are made of zinc and oxygen. The produced nanorods are pure Ag@ZnO NRs with no detectable impurities, as evidenced by the absence of any other peak in the spectrum associated with any impurity.

Fourier-transform infrared spectroscopy analysis of Ag@ZnO nanorods

Figure 3 presents the typical Fourier-transform infrared spectroscopy (FTIR) spectrum of produced Ag@ZnO NRs. Different groups and bonds were examined using the FTIR spectrum. Ag doping changes the bond length of the sample, resulting in a minor shift in peak location toward higher wavelengths.

The distinctive stretching mode of the Zn–O bond is responsible for a significant vibrational band in the FTIR spectra, ranging from 450 to 550 cm^{-1}. The presence of a hydroxy residue, which is caused by ambient moisture, is indicated by a large peak at 3433 cm^{-1} (stretching) and at 1330 to 1720 cm^{-1} (bending). Peaks present at 2922 and 2854 cm^{-1} relate to the stretching vibration of carbon and hydrogen bonds. The peaks at

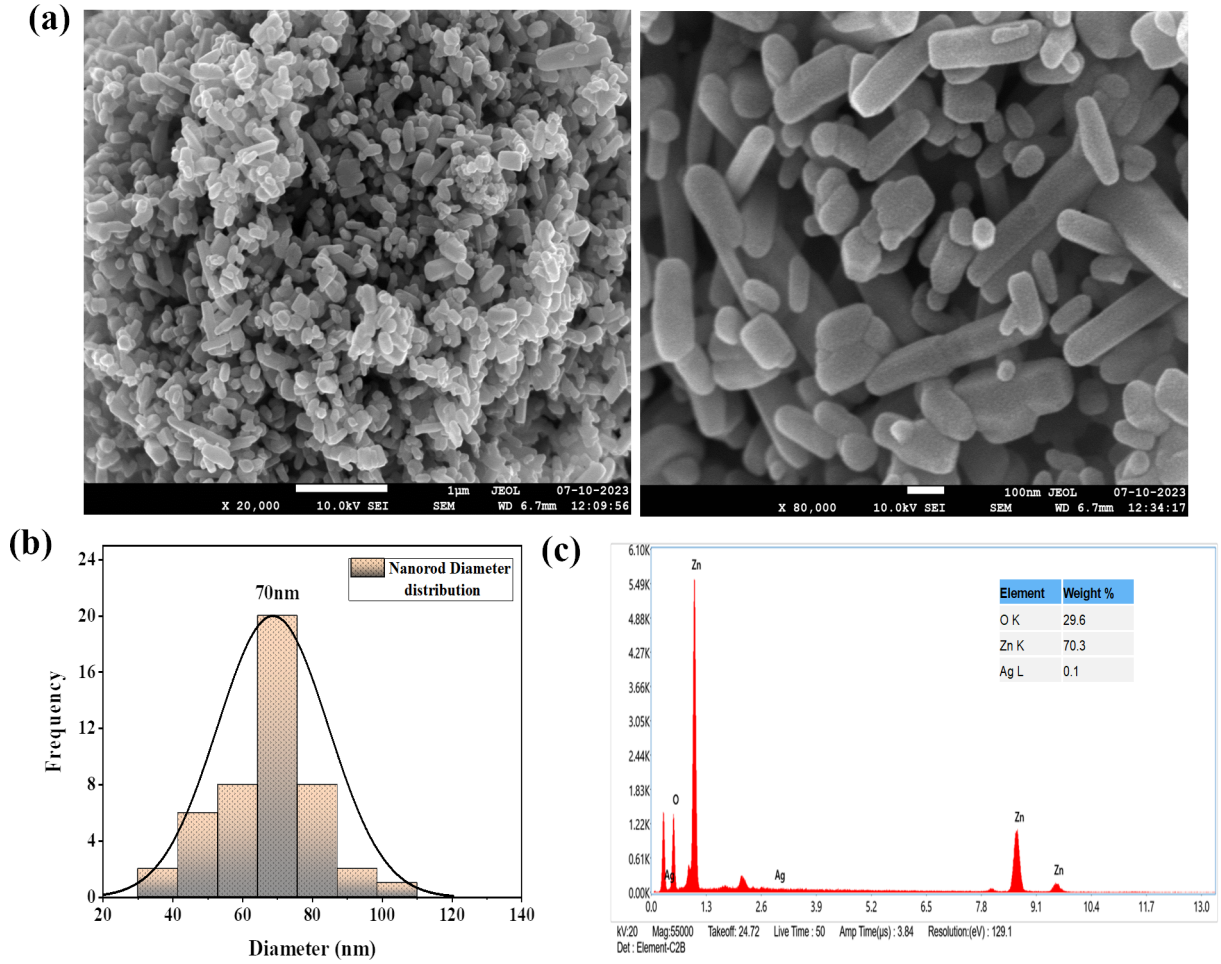

Figure 2: (a) SEM images, (b) diameter distribution of nanorods, and (c) EDS of Ag@ZnO NRs.

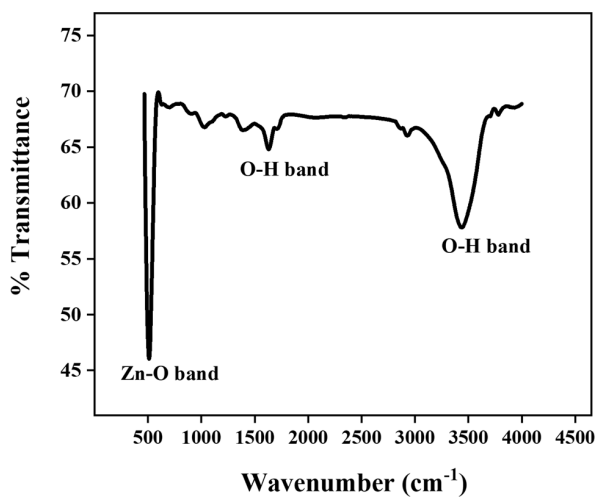

Figure 3: FTIR of Ag@ZnO NRs.

1030 and 1380 cm^{-1} are related to vibrational or in-plane bending of residual ethanol which was used for washing the nanoparticles and KBr pellet die set (used for pellet making for FTIR) [18,19].

Optical study of Ag@ZnO nanorods

Figure 4a displays the optical spectra of Ag@ZnO NRs, which was obtained in the 200–600 nm wavelength range. The absorbance peak in this spectrum, which is moved toward a higher wavelength also known as redshift, is shown at 378 nm (for pure ZnO it is 362 nm) [20]. The bandgap energy of Ag@ZnO NRs has been calculated through the use of the Tauc's method, as shown in Figure 4b, and it is determined to be 2.8 eV.

No further peak indicative of contaminants is observed in the aforementioned spectra, indicating the high purity of the synthesized nanorods. Incorporating Ag dopants into ZnO frequently

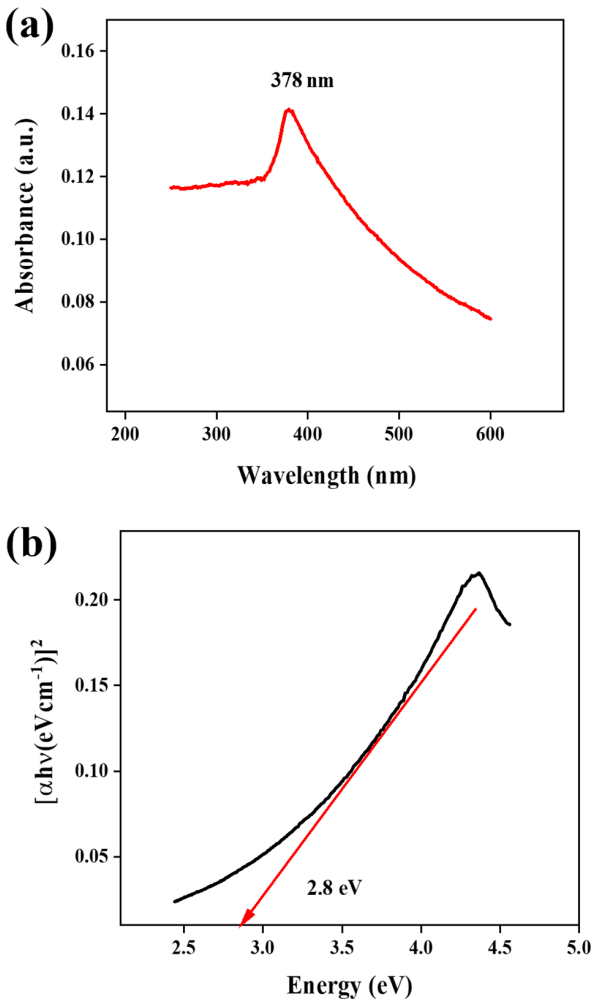

Figure 4: (a) UV–vis spectrum and (b) bandgap of Ag@ZnO NRs.

causes a reduction in the bandgap, leading to a shift toward longer wavelengths in the absorption spectra. The smaller bandgaps of the samples in optoelectronic devices provide a significant advantage [21].

Zeta potential of Ag@ZnO nanorods

Surface properties of the synthesized Ag@ZnO NRs were studied using dynamic light scattering analysis, and their zeta potential was determined. Figure 5 represents the zeta potential of Ag@ZnO NRs. The samples were collected in the liquid state and the Ag@ZnO NRs zeta potential of ≈30 mV accounts for the stability of the nanoparticles in water.

Raman spectroscopy of Ag@ZnO nanorods

The influence of Ag doping in ZnO nanorods were investigated by Raman scattering. Raman scattering of Ag@ZnO NRs were recorded using a 532 nm laser at room temperature in the spectra range varying from 0 to 2000 cm^{-1}. ZnO has four atoms in each primitive cell, which results in 12 degrees of freedom (three acoustic phonon modes and nine optical phonon modes). Figure 6 demonstrates the Raman spectra of Ag@ZnO NRs; when doping is done in ZnO, there is a significant change in the optical and non-optical modes of ZnO. The collapse of the translational crystal symmetry is a consequence of Ag doping, which also results in peaks broadening. The wurtzite structure of ZnO is characterized by dominant peaks at approximately 96 and 473 cm^{-1}, the peak at 473 cm^{-1} represents the E_{2H} mode corresponding to oxygen, and this mode is sensitive to internal stress. Ag doping results in the broadening of the E_{2H} mode and also expands and relocates the $E_1(LO)/A_1(LO)$ peak, present at approximately 567 cm^{-1}, to a lower energy level. The broadening and shifting of the $A_1(LO)$ modes is the result of the scattering effects generated by the $A_1(LO)$ branch extending

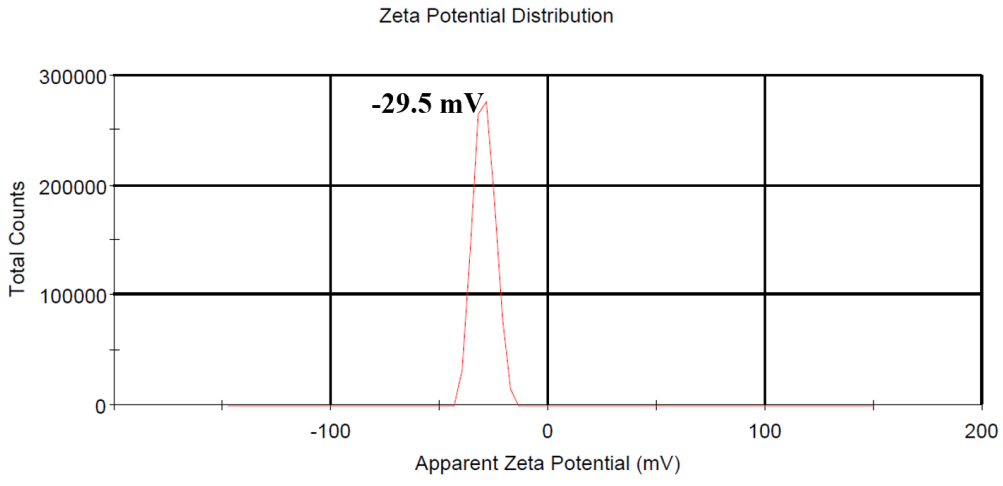

Figure 5: Zeta potential of Ag@ZnO NRs.

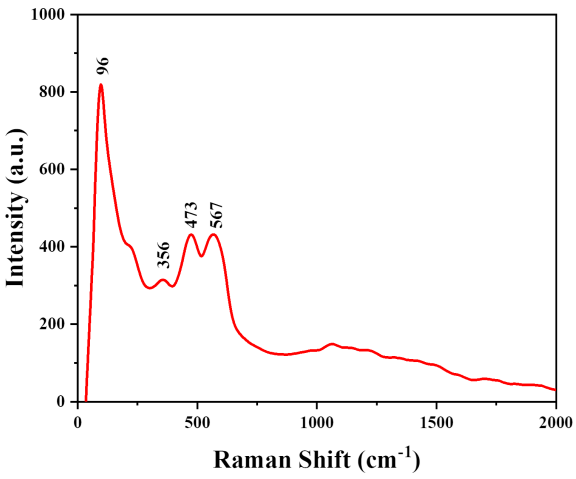

Figure 6: Raman spectra of Ag@ZnO NRs.

beyond the central region of the Brillouin zone. Oxygen vacancies are commonly linked to the A_1(LO) phonon mode. The presence of a small peak at 218 cm^{-1} denotes the radial movement of Ag atoms. Raman peaks at around 356 cm^{-1} are specifically attributed to the A_1(TO) mode. Also, the results of Ag doping in ZnO coincide with XRD results of secondary phase formations [22-24].

X-ray photoelectron spectroscopy study of Ag@ZnO nanorods

The physical state and chemical compositions of Ag@ZnO NRs were analyzed using X-ray photoelectron spectroscopy (XPS). Figure 7a represents the scan results of the binding energy. The peaks of the curve were attributed to the elements silver, zinc, oxygen, and carbon, whereas no peaks corresponding to other elements were observed. Figure 7b represents the coupled state of the 3d orbital of silver. The peaks at 371.2 and 365.3 eV cor-

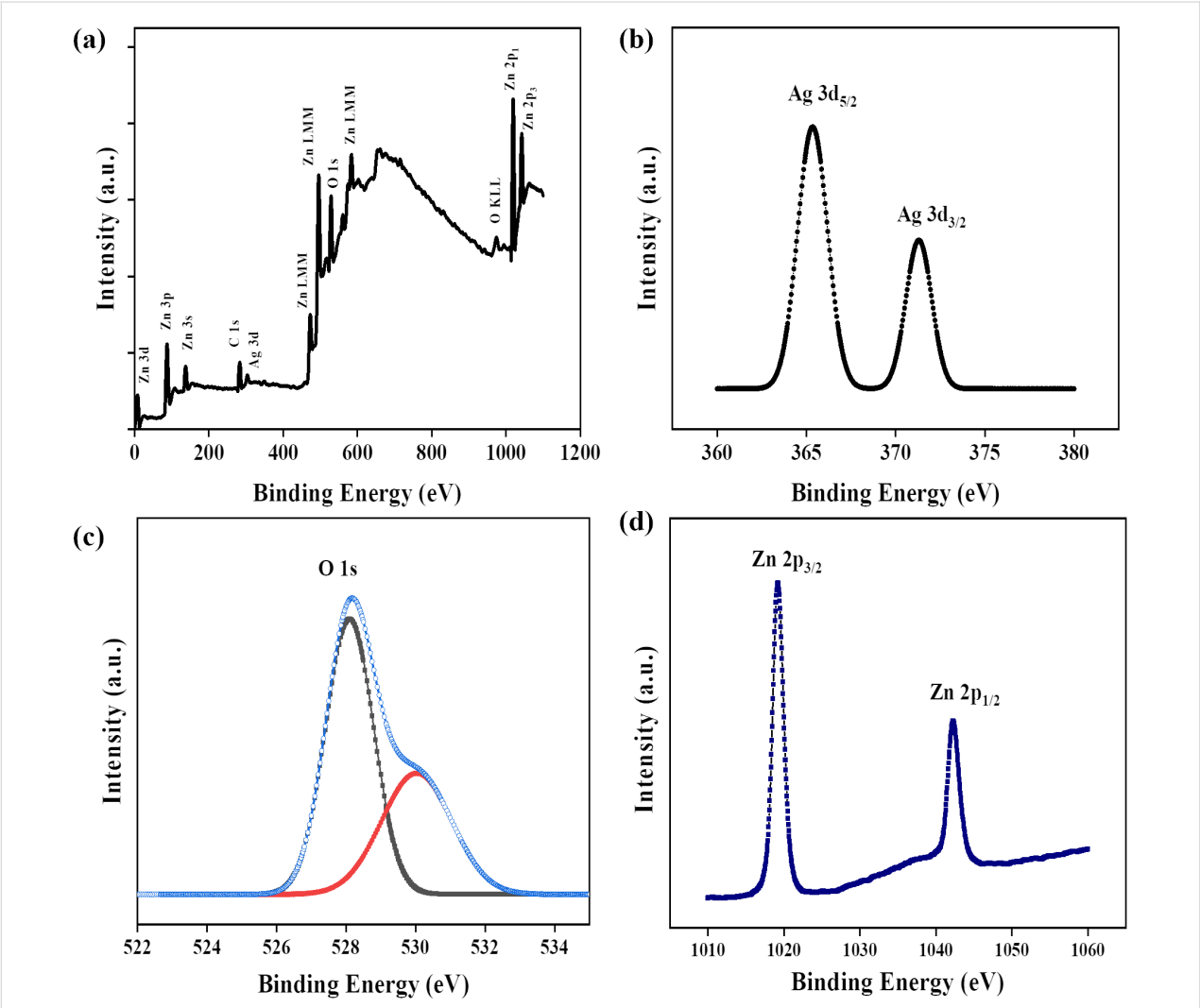

Figure 7: XPS of Ag@ZnO NRs: (a) full scan spectrum, (b) scan of Ag 3d, (c) scan of oxygen 1s, and (d) scan of Zn 2p.

respond to Ag $3d_{3/2}$ and Ag $3d_{5/2}$, respectively, and the 5.9 eV difference between them indicate that Ag exists in the form of Ag_2O. This demonstrates the Ag integration into ZnO and the absence of metallic Ag production. The Ag-doped ZnO samples display two distinct peaks at 1042.4 and 1019.2 eV in their Zn 2p spectra (Figure 7d). The peak at 1042.4 eV corresponds to the Zn $2p_{1/2}$ and the 1019.2 eV peak corresponds to Zn $2p_{3/2}$. The peak location was marginally changed toward lower binding energy values with the addition of Ag. The peak shift observed was a consequence of the increase in electron density in the host matrix which is caused by the doping of Ag. The 23 eV gap between two binding energies suggests that the Zn element is in a +2 oxidation state. The 1s orbital spectra of oxygen in Ag–ZnO samples are shown in Figure 7c, revealing a peak with a binding energy of 528 eV. The oxygen peak can be resolved into two distinct peaks, which indicates two different types of oxygen species (one at 528 eV due to lattice oxygen of ZnO and another at 530 eV due to presence of surface hydroxy group) [25,26].

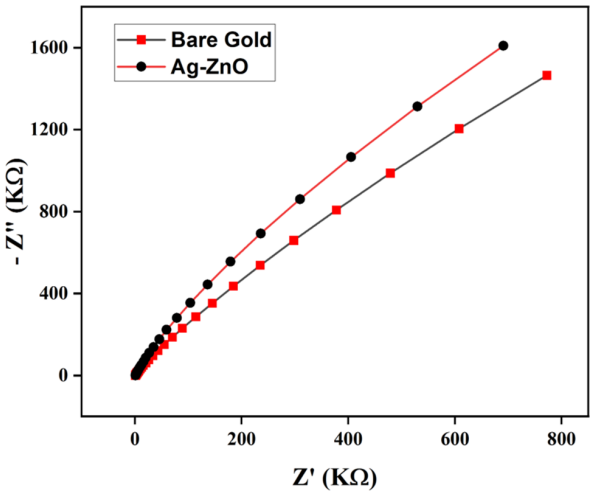

Figure 8: Electrochemical impedance spectroscopy (EIS) Nyquist plots of modified Ag@ZnO NRs/Au and bare Au electrode.

Cyclic voltammetry of modified Ag@ZnO nanorods/gold electrode

Figure 8 presents the results of an impedance analysis using a frequency-response analyzer (FRA) potentiostat on both fabricated Ag–ZnO/Au electrodes and bare gold electrodes. The modified Ag@ZnO NRs electrode exhibits higher impedance than that of the bare gold electrode. This higher impedance leads to better sensitivity, better electron exchange, and can provide more information about the electrochemical process. The higher impedance of the modified Ag@ZnO NRs electrode improved signal-to-noise ratio, which means that the electrode can better distinguish the electrochemical signal of the analyte from background noise, resulting in more accurate results. Furthermore, a higher impedance of the electrode can provide additional details about the electrochemical process. It can help to understand the kinetics of electron transfer reactions, analyte diffusion, and electrode surface contact mechanisms. A modified Ag@ZnO NRs electrode with greater impedance is more stable and durable. This provides consistent performance throughout time, which is critical for obtaining accurate and repeatable electrochemical results.

The lead chemical sensor was fabricated by utilizing the Ag–ZnO nanorods, which functioned as efficient electron mediators. An aqueous solution which includes freshly produced Ag–ZnO nanorods was generated and coated onto a gold electrode. The modified electrode was then dried to form a chemical sensor specifically designed for the detection of lead. The performance of the sensor, including sensitivity, correlation coefficient, and detection limit, was evaluated using cyclic voltammetry. This evaluation involved the usage of a three-electrode system and a gold electrode modified with Ag–ZnO nanorods. The modified electrode was used as a working electrode in the three-electrode system, while the reference electrode was made of Ag/AgCl (sat. KCl), and the Pt electrode was used as a counter electrode [27]. In order to investigate Ag@ZnO NRs response to lead, a standard cyclic voltammetry (CV) experiment was conducted both with and without lead. A typical CV sweep curve for a gold electrode modified with Ag@ZnO NRs in double-distilled water with (black line) and without (red line) lead at a 40 mV/s scan rate is shown in Figure 9.

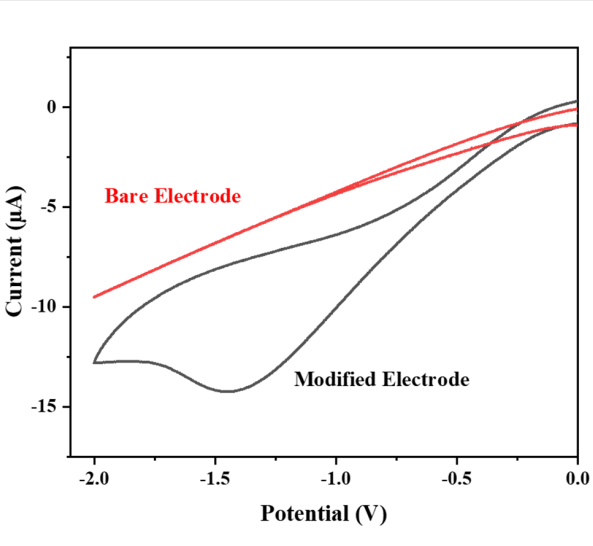

Figure 9: Cyclic voltammetry sweep curves for a modified electrode (black curve) or a bare electrode (red curve) in lead solution.

The obtained CV graph demonstrates that the gold electrode modified with Ag@ZnO NRs exhibits no response in the absence of lead (black line). However, when lead is introduced in moderate quantities, a significant reduction peak is distinctly observed in the *I*–*V* graph (red line). A reduction peak appeared approximately at −1.5 V with an I_{pc} of −14.5 µA. The obtained *I*–*V* graph clearly shows that the fabricated electrode is highly responsive to lead, which supports the idea that the synthesized Ag@ZnO NRs are useful electron mediators for the creation of lead chemical sensors. The significant rise in peak height is indicative of a faster electron-transfer event because it causes a sharper, more defined peak. Furthermore, the absence of a cathodic current in the reverse cycle indicates the irreversibility of the electrochemical response that was observed [28]. The suggested redox reaction that occurs during the electrochemical sensing experiment is depicted in Figure 10.

Scan rate study of the modified sensor

Furthermore, by carrying out several scan-rate dependent studies, the electrochemical response of the modified electrode was thoroughly investigated. The studies on scan-rate dependence were conducted at different scan rates between 40–100 mV/s in a solution containing 20 ppm of lead. Figure 11a displays the CV results of the Ag@ZnO NRs/Nafion/gold electrode, using scan rates varying from 40 to 100 mV/s. The observed CV response, which varies with the scan rate, indicates that the current values proportionally increase with higher scan rates, indicating that the reduction process is controlled by diffusion. Figure 11b displays a graph illustrating the relationship between I_{pc} (cathodic current) and $v^{1/2}$ (square root of the scan rate). Clearly, the cathodic peak current demonstrates a linear connection with $v^{1/2}$, demonstrating diffusion-controlled kinetics [29].

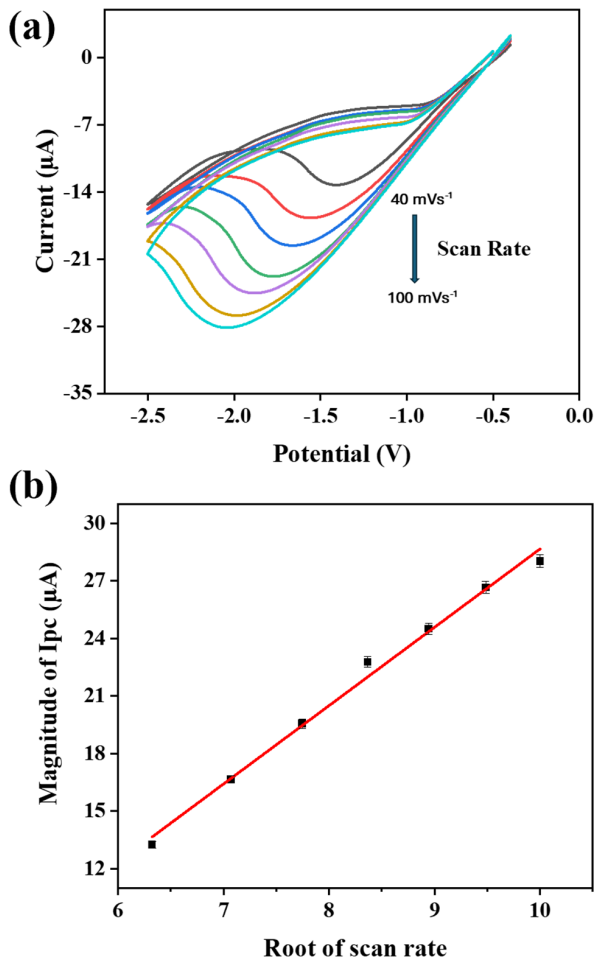

Figure 11: (a) The *I*–*V* response of the modified electrode at varying scan rates and (b) peak current magnitude as a function of the square root of the scan rate of the modified electrode.

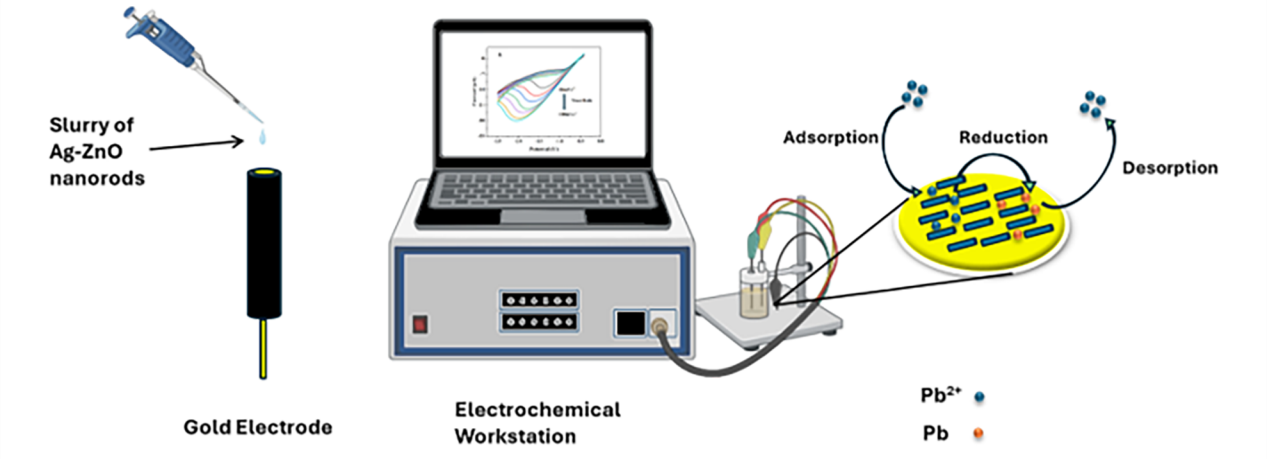

Figure 10: Schematic diagram of the proposed electrochemical detection of lead using a potentiostat and a galvanostat. Figure 10 was partly created in BioRender. Ravinder, R. (2025) https://BioRender.com/g83x775. Afterwards it was adapted with PowerPoint. This content is not subject to CC BY 4.0.

Concentration effect on the peak current or calibration curve

Figure 12a illustrates a steady increase in peak current as lead concentration increases. A standard calibration curve was obtained by graphing the magnitude of peak current data as a function of concentration (Figure 12b). The prepared lead sensor demonstrates a high sensitivity of 16 $\mu A \cdot ppm^{-1} \cdot cm^{-2}$, as determined by dividing the slope of the standard curve with the surface area of the modified electrode. The limit of detection was found to be 3 ppm by estimating it using the standard curve (current as a function of the concentration) illustrated in Figure 12b. The calculation was carried out by dividing the standard deviation by the slope of the standard curve and multiplying by three [30].

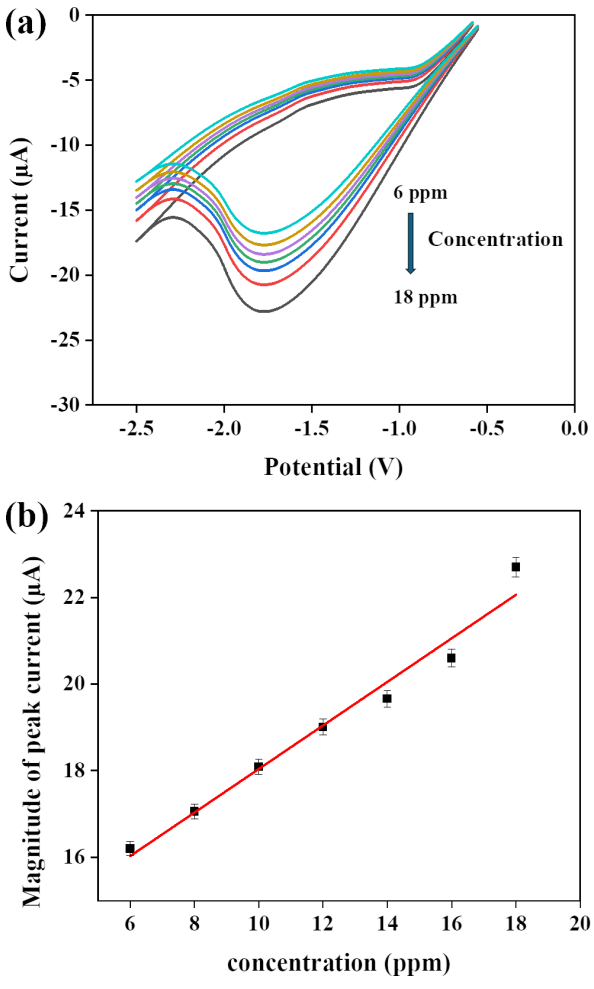

Figure 12: (a) *I–V* response of the modified electrode at varying concentrations of lead; and (b) peak current magnitude as a function of lead concentration.

Analytical application of the proposed sensor

To check the suitability of the proposed lead sensor, different real samples were tested. Real samples were collected from various sources (e.g., tap water, groundwater, canal water, and water contaminated with a known amount of lead). In order to assess the presence of lead, real samples were analyzed by measuring the cyclic voltammetry response of the sensor. As shown in Figure 13, clearly visible signals have been obtained for artificially contaminated samples using the built electrode and the standard approach.

Table 1 presents the samples, the lead spiking amount, and the calculated amount of lead using the aforementioned technique. As the detected amount of lead in real samples are slightly higher than the spiking amount of lead, this is probable due to lead toxicity of real samples or greater conductivity of real samples due to the presence of more ions, which can influence the calculation of lead concentration.

Table 1 illustrates that the designed sensor and the proposed technique yielded reasonable outcomes. The obtained results are compatible with theoretical calculations, demonstrating the feasibility of the proposed standardized technique. Table 2 presents the comparison of this work with other similar works. The fabricated sensor showed a slightly higher limit of detection (LOD) value, which is due to the use of PBS and the higher impedance of the electrode. An acidic pH provides better sensitivity, but it also brings health and safety issues, environmental impact, can cause electrode corrosion, enhances interference, and is incompatible with real-life or biological samples. Therefore, PBS with pH 7 has been used for electrochemical studies since it provides a stable pH, which is crucial for maintaining consistent electrochemical conditions during experiments.

Conclusion

In conclusion, a low-temperature co-precipitation technique was utilized to yield highly crystalline nanorods of ZnO doped with Ag. A variety of techniques were employed to analyze the physical and chemical characteristics of as-synthesized Ag@ZnO NRs. The results demonstrate that the synthesized nanorods possess a crystalline structure, specifically a wurtzite hexagonal phase structure (space group: 186: $P6_3mc$) and exhibit advantageous optical properties. The integration of Ag into ZnO nanostructures enhances their optical characteristics and improves their ability to detect heavy metal ions such as lead. The reason for this is that the addition of silver decreases the holes and electron recombination rate, resulting in an expansion of the surface area. Subsequently, they were effectively employed as an electron mediator in the fabrication of highly sensitive lead sensors. The fact that prolonged exposure to lead ions can result in a range of health problems, it is crucial to identify the presence of lead for the sake of public health and environmental preservation. The lead chemical sensor exhibited exceptional sensitivity and a remarkably low detection limit. The synthe-

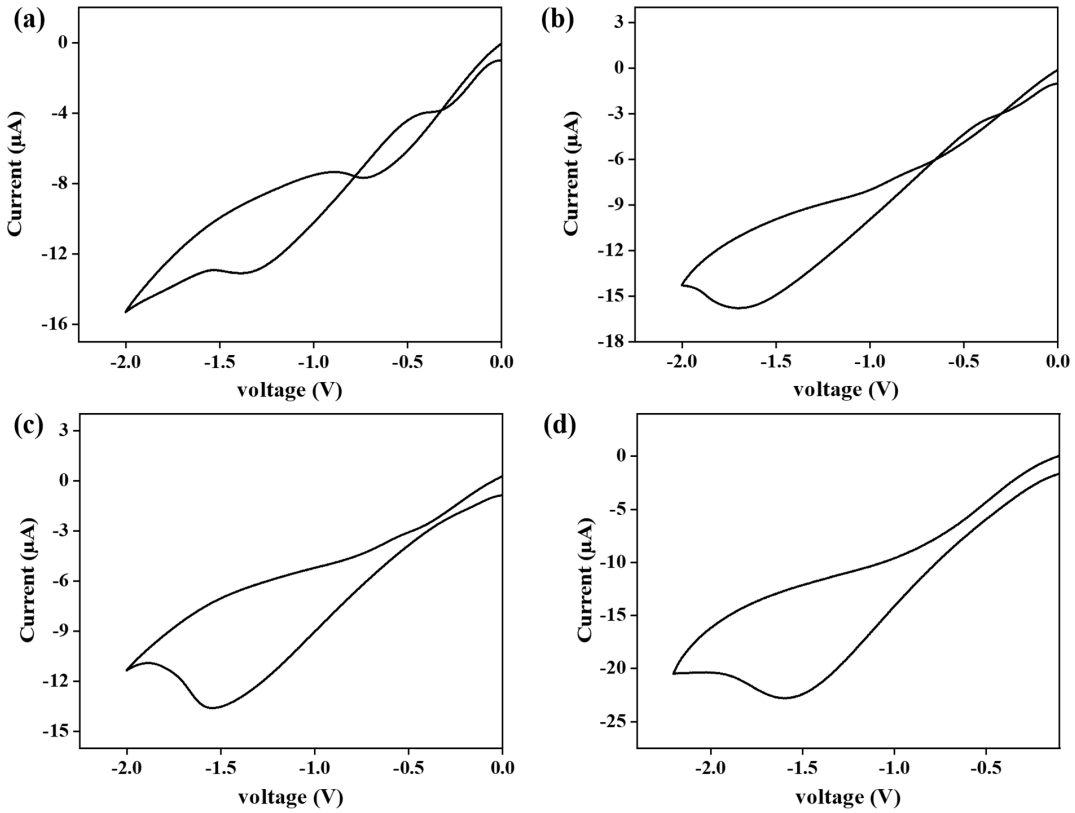

Figure 13: *I–V* response of the modified electrode at a varying concentration of lead in (a) canal water, (b) groundwater, (c) water obtained after reverse osmosis (RO) and (d), supply drinking water.

Table 1: Quantitative analysis of lead concentrations in real samples artificially contaminated with lead.

Sr. No.	Sample	Amount of lead measured by the modified Ag–ZnO electrode (ppm)	Spiking amount of lead (ppm)
1	spiked canal water	3.0398	3
2	spiked ground water	8.3784	8
3	spiked RO water	4.1752	4
4	spiked supply drinking water	19.5219	19

Table 2: Comparison between the fabricated sensor and similar electrochemical sensors.

S. No.	Electrode	LOD	Linear range	Method of detection	Refs.
1	Ag–ZnO modified glassy carbon electrode	3.5 nM (in acetate buffer)	50–350 nM	DPASV	[18]
2	Cork-modified carbon paste electrode	0.3 μM (in 0.1 M H_2SO_4) 4.8 μM (in 0.1 M PBS)	1–25 μM	SWASV	[31]
3	Calcinated and acidified clay-modified carbon graphite electrode	0.15 μM (in 0.1 M Na_2SO_4)	0.24–2.6 μM	SWV	[32]
4	CG electrode	0.4 μM (in 0.5 M $NaNO_3$)	5–50 μM	ASV	[33]
5	MWCNT+ B18C6 ion-selective electrode	19.9 μM (NaTFPB as a cation exchanger)	0.1–10 mM	potentiometry	[34]
6	Ag@ZnO NRs modified gold electrode	8 μM (3 ppm) (in 0.1 M PBS)	16–48 μM	CV	present work

sized lead sensor had a high sensitivity of 16 μA·ppm^{-1}·cm^{-2}, along with a detection limit of 3 ppm. Additionally, it demonstrated a response time of less than 2 s. This sensor is most suitable for applications that necessitate cost-effectiveness, rapid readings, and data collection in the field or at the point of care. To our knowledge, this study presents the initial demonstration of a novel method for fabricating an exceptionally responsive lead chemical sensor utilizing Ag@ZnO NRs.

Experimental Details

Synthesis of Ag@ZnO nanorods

For the synthesis of Ag@ZnO NRs, chemicals were purchased from Sigma-Aldrich and used as such without any additional purification steps. Firstly, a 2 mL aqueous solution of silver nitrate ($AgNO_3$) (0.1 M) and a 100 mL aqueous solution of zinc nitrate hexahydrate (Zn $(NO_3)_2{\cdot}6H_2O$) (0.1 M) were simultaneously prepared. After that, the silver nitrate solution was mixed with the zinc nitrate hexahydrate solution. The resulting solution was stirred for approximately 10 min at room temperature. After the reaction time, a 1 M potassium hydroxide (KOH) solution was gradually added drop by drop. This step adjusted the pH of the mixture to 10. Then the mixture underwent further stirring for 2 h at room temperature. Once the stirring was complete, the deposited precipitate was formed. These precipitates were subjected to centrifugation and the pellet was collected; further washing was done multiple times using distilled water and ethanol. The obtained nanoparticles were oven-dried at 70 °C for 2 h. Finally, the nanoparticles were annealed by subjecting them to a temperature of 450 °C in a muffle furnace for 1 h.

Evaluation of Ag@ZnO nanorods

The Ag@ZnO NRs obtained above were assessed for their morphological, structural, and optical characteristics. The FE-SEM experiments and examination of morphological characteristics were performed on a 7610F Plus/JEOL. A benchtop Miniflex X-ray diffractometer, (Japan model) manufactured by Rigaku, was utilized to analyze the structural and crystal phases. The study was conducted using a wavelength of 1.54 Å and a 2θ angle ranging from 20° to 90°. The elemental compositions were analyzed using EDS and XPS (Model PHI 5000 Versaprobe III). The chemical states were assessed using FTIR spectroscopy with a Perkin Elmer spectrometer model. The spectrum data was acquired between the frequency range of 450 to 4000 cm^{-1} (resolution of 0.5 cm^{-1}). The optical characteristics of the obtained Ag-doped ZnO nanorods were determined using UV–visible spectroscopy (Varian Cary-5000) at room temperature. The measurements were taken in the wavelength range of 200 to 600 nm. Raman spectroscopy (Alpha300/WI Tec) was used to investigate the molecular vibrations, rotational energy, electronic energy levels, and scattering characteristics of Ag–ZnO nanorods. The Malvern Nano-ZS90 was utilized to determine the zeta potential of synthesized nanorods.

Fabrication of the lead sensor / (Ag@ZnO nanorods/gold electrode)

The obtained Ag@ZnO NRs served as an electron mediator for creating a lead electrochemical sensor with high sensitivity. In order to coat the Ag@ZnO NRs, a mixture of 1 mg of as-produced nanorods was mixed in 10 mL of ethanol and sonicated for 30 min. This 4 μL mixture was then applied to the cylindrical gold electrode of 2 mm diameter and allowed to dry at room temperature. Then, 1 μL Nafion solution was applied resulting in a uniform layer of tightly bound nanorods covering the entire electrode surface. Subsequent electrochemical sensing experiments were conducted at room temperature using an Autolab electrochemical workstation with a three-electrode configuration. The working electrode consisted of the modified Ag@ZnO NRs/Au electrode, a platinum wire used as the counter electrode, and the reference electrode was an Ag/AgCl electrode. A 0.1 M phosphate buffer solution with a pH of 7.0 was used for all measurements.

Acknowledgements

The authors acknowledge the instrumentation support from the Central Instrumental Lab (CIL) at Guru Jambheshwar University of Science and Technology, Hisar, Haryana. The graphical abstract was partly created in BioRender. Ravinder, R. (2025) https://BioRender.com/g83x775. Afterwards it was adapted with PowerPoint. This content is not subject to CC BY 4.0.

Funding

The authors thank the MoE, Government of India, for a research grant vide letter No. SPARC/2019-2020/P2065/SL, dated 28-07-2023. Mr. Ravinder Lamba is thankful to UGC, Govt. of India for providing SRF vide letter number 1399/(CSIR-UGC NET JUNE 2019) dated 16 December 2019. Dr. Gaurav Bhanjana is thankful to CSIR, Govt. of India for providing CSIR-SRA (No. B-12998 dated 31 March 2023). Sandeep Kumar thanks the Punjab Engineering College (Deemed to be University) for providing a research initiation grant (No. PEC/DSR&IC/54 dated 10-04-2024) and the Department of Science and Technology, Govt. of India for the DST-PURSE grant (No. SR/PURSE/2024/350 dated 14-10-2024).

Author Contributions

Ravinder Lamba: data curation; investigation; writing – original draft. Gaurav Bhanjana: formal analysis; methodology; writing – original draft. Neeraj Dilbaghi: formal analysis; methodology; resources; supervision; writing – review & editing. Vivek Gupta: data curation; formal analysis; supervision; validation. Sandeep Kumar: conceptualization; formal analysis;

funding acquisition; resources; supervision; visualization; writing – review & editing.

ORCID® iDs

Vivek Gupta - https://orcid.org/0000-0002-3762-5376

Data Availability Statement

Data generated and analyzed during this study is available from the corresponding author upon reasonable request.

References

1. Gavrilaş, S.; Ursachi, C. Ş.; Perța-Crișan, S.; Munteanu, F.-D. *Sensors* **2022,** *22,* 1513. doi:10.3390/s22041513
2. Keshri, S.; Goel, A. K.; Garg, A. K. *Cureus* **2021,** *13,* e15155. doi:10.7759/cureus.15155
3. Yin, Y.; Zhang, P.; Yue, X.; Du, X.; Li, W.; Yin, Y.; Yi, C.; Li, Y. *Ecotoxicol. Environ. Saf.* **2018,** *161,* 755–762. doi:10.1016/j.ecoenv.2018.06.056
4. Settle, D. M.; Patterson, C. C. *Science* **1980,** *207,* 1167–1176. doi:10.1126/science.6986654
5. Abkenar, S. D.; Dahaghin, Z.; Sadeghi, H. B.; Hosseini, M.; Salavati-Niasari, M. *J. Anal. Chem.* **2011,** *66,* 612–617. doi:10.1134/s1061934811060062
6. Jenner, G. A.; Longerich, H. P.; Jackson, S. E.; Fryer, B. J. *Chem. Geol.* **1990,** *83,* 133–148. doi:10.1016/0009-2541(90)90145-w
7. Ding, R.; Cheong, Y. H.; Ahamed, A.; Lisak, G. *Anal. Chem. (Washington, DC, U. S.)* **2021,** *93,* 1880–1888. doi:10.1021/acs.analchem.0c04247
8. Okpara, E. C.; Fayemi, O. E.; Wojuola, O. B.; Onwudiwe, D. C.; Ebenso, E. E. *RSC Adv.* **2022,** *12,* 26319–26361. doi:10.1039/d2ra02733j
9. Tiwari, J.; Rao, C. *Solid State Ionics* **2008,** *179,* 299–304. doi:10.1016/j.ssi.2008.01.097
10. Shi, Z.-F.; Zhang, Y.-T.; Cui, X.-J.; Zhuang, S.-W.; Wu, B.; Chu, X.-W.; Dong, X.; Zhang, B.-L.; Du, G.-T. *Phys. Chem. Chem. Phys.* **2015,** *17,* 13813–13820. doi:10.1039/c5cp00674k
11. Xu, J.; Pan, Q.; Shun, Y.; Tian, Z. *Sens. Actuators, B* **2000,** *66,* 277–279. doi:10.1016/s0925-4005(00)00381-6
12. Ren, C.; Yang, B.; Wu, M.; Xu, J.; Fu, Z.; Iv, Y.; Guo, T.; Zhao, Y.; Zhu, C. *J. Hazard. Mater.* **2010,** *182,* 123–129. doi:10.1016/j.jhazmat.2010.05.141
13. Meng, X.; Fan, G.; Xu, L.; Zhang, B.; Chen, Y.; Zhou, Y.; Xu, F.; Zhang, S. *Phys. B (Amsterdam, Neth.)* **2025,** *699,* 416864. doi:10.1016/j.physb.2024.416864
14. Naqvi, S. M. A.; Soleimani, H.; Yahya, N.; Irshad, K. *AIP Conf. Proc.* **2014,** *1621,* 530–537. doi:10.1063/1.4898517
15. Fan, J.; Freer, R. *J. Appl. Phys.* **1995,** *77,* 4795–4800. doi:10.1063/1.359398
16. Sharma, N.; Singh, R. P. P.; Sharma, V. *Appl. Phys. A: Mater. Sci. Process.* **2019,** *125,* 326. doi:10.1007/s00339-019-2594-9
17. Mote, V.; Purushotham, Y.; Dole, B. *J. Theor. Appl. Phys.* **2012,** *6,* 6. doi:10.1186/2251-7235-6-6
18. Nagaraju, G.; Udayabhanu; Shivaraj; Prashanth, S. A.; Shastri, M.; Yathish, K. V.; Anupama, C.; Rangappa, D. *Mater. Res. Bull.* **2017,** *94,* 54–63. doi:10.1016/j.materresbull.2017.05.043
19. Zamiri, R.; Rebelo, A.; Zamiri, G.; Adnani, A.; Kuashal, A.; Belsley, M. S.; Ferreira, J. M. F. *RSC Adv.* **2014,** *4,* 20902–20908. doi:10.1039/c4ra01563k
20. Kumar, S.; Bhanjana, G.; Dilbaghi, N.; Umar, A. *Ceram. Int.* **2015,** *41,* 3101–3108. doi:10.1016/j.ceramint.2014.10.154
21. Hosseini, S. M.; Sarsari, I. A.; Kameli, P.; Salamati, H. *J. Alloys Compd.* **2015,** *640,* 408–415. doi:10.1016/j.jallcom.2015.03.136
22. Hamidian, K.; Sarani, M.; Sheikhi, E.; Khatami, M. *J. Mol. Struct.* **2022,** *1251,* 131962. doi:10.1016/j.molstruc.2021.131962
23. Altun, B.; Karaduman Er, I.; Çağırtekin, A. O.; Ajjaq, A.; Sarf, F.; Acar, S. *Appl. Phys. A: Mater. Sci. Process.* **2021,** *127,* 687. doi:10.1007/s00339-021-04843-9
24. Silambarasan, M.; Shanmugam, S.; Soga, T. *Int. J. ChemTech Res.* **2015,** *7,* 1644–1650.
25. Ahmad, I.; Ahmed, E.; Ahmad, M. *SN Appl. Sci.* **2019,** *1,* 327. doi:10.1007/s42452-019-0331-9
26. Molla, M. A. I.; Furukawa, M.; Tateishi, I.; Katsumata, H.; Kaneco, S. *J. Compos. Sci.* **2019,** *3,* 18. doi:10.3390/jcs3010018
27. Bhanjana, G.; Toor, I.; Chaudhary, G. R.; Dilbaghi, N.; Kim, K.-H.; Kumar, S. *J. Mol. Liq.* **2019,** *292,* 111455. doi:10.1016/j.molliq.2019.111455
28. Bhanjana, G.; Chaudhary, G. R.; Dilbaghi, N.; Chauhan, M.; Kim, K.-H.; Kumar, S. *Electrochim. Acta* **2019,** *293,* 283–289. doi:10.1016/j.electacta.2018.10.042
29. Bhanjana, G.; Rana, P.; Chaudhary, G. R.; Dilbaghi, N.; Kim, K.-H.; Kumar, S. *Sci. Rep.* **2019,** *9,* 8050. doi:10.1038/s41598-019-44525-4
30. Bansal, P.; Bhanjana, G.; Prabhakar, N.; Dhau, J. S.; Chaudhary, G. R. *J. Mol. Liq.* **2017,** *248,* 651–657. doi:10.1016/j.molliq.2017.10.098
31. Silva, I. B.; de Araújo, D. M.; Vocciante, M.; Ferro, S.; Martínez-Huitle, C. A.; Dos Santos, E. V. *Appl. Sci.* **2021,** *11,* 2355. doi:10.3390/app11052355
32. Blaise, N.; Gomdje Valéry, H.; Maallah, R.; Oubaouz, M.; Tigana Djonse Justin, B.; Andrew Ofudje, E.; Chtaini, A. *J. Anal. Methods Chem.* **2022,** *2022,* 6900839. doi:10.1155/2022/6900839
33. Silva, K. N. O.; Paiva, S. S. M.; Souza, F. L.; Silva, D. R.; Martínez-Huitle, C. A.; Santos, E. V. *J. Electroanal. Chem.* **2018,** *816,* 171–178. doi:10.1016/j.jelechem.2018.03.051
34. Kerric, G.; Parra, E. J.; Crespo, G. A.; Xavier Rius, F.; Blondeau, P. *J. Mater. Chem.* **2012,** *22,* 16611. doi:10.1039/c2jm33153e

BEILSTEIN JOURNAL OF NANOTECHNOLOGY

N_2^+-implantation-induced tailoring of structural, morphological, optical, and electrical characteristics of sputtered molybdenum thin films

Usha Rani, Kafi Devi, Divya Gupta and Sanjeev Aggarwal*

Full Research Paper

Open Access

Address:
Ion Beam Centre, Department of Physics, Kurukshetra University, Kurukshetra-136119, India

Email:
Sanjeev Aggarwal* - saggarwal@kuk.ac.in

* Corresponding author

Keywords:
atomic force microscopy; grazing angle X-ray diffractometer; Keithley parametric analyzer; Mo thin films; RF sputtering; spectroscopic ellipsometry

Beilstein J. Nanotechnol. **2025,** *16,* 495–509.
https://doi.org/10.3762/bjnano.16.38

Received: 30 September 2024
Accepted: 19 March 2025
Published: 01 April 2025

This article is part of the thematic issue "Low-dimensional nanomaterials for sustainable applications".

Guest Editor: S. Kumar

Abstract

Molybdenum (Mo) thin films have extensive applications in energy storage devices and photovoltaic solar cells because of their remarkable thermal stability, high melting point, and chemical inertness. In the present study, Mo thin films of different thicknesses (150, 200, 250, and 300 nm) have been deposited on Si(100) substrates via radio frequency sputtering in an argon atmosphere at room temperature. Some of these films have been implanted with 1×10^{17} $N_2^+ \cdot cm^{-2}$ at 30 keV using a current density of 4 $\mu A \cdot cm^{-2}$. Surface morphology and structural, optical, and electrical properties of the as-deposited and implanted Mo thin films have been systematically investigated. The crystallinity of Mo thin films is enhanced with increasing thickness of the as-deposited films. This pattern persists with film thickness even after N_2^+ implantation. After implantation, crystallinity decreases relative to as-deposited films with the same nominal thickness. The AFM analysis reveals that RMS roughness increases with the thickness of Mo films. Optical studies using spectroscopic ellipsometry reveal a significant increase in absorbance and reflectance in as-deposited and N_2^+-implanted films. Electrical investigations show that the conductivity increases with film thickness in both as-deposited and implanted films. The conductivity decreases for the same nominal film thickness after implantation.

Introduction

Molybdenum thin films have garnered significant attention in diverse technological applications owing to their outstanding characteristics. The high melting point and stability of molybdenum ensure that it remains structurally intact under the harsh operating conditions of solar cells [1,2]. This stability is essential for long-term reliability and performance. The low resistivity of Mo thin films makes them desirable for integrated circuits, where they contribute to the efficient flow of

electrical current [3]. Furthermore, their optical properties make them well suited for a use as a protective coating in energy storage and electronic devices [4,5]. Mo films deposited on substrates under suitable conditions lead to improvements in functionality and address the needs of various cutting-edge industries [6,7].

For the deposition of Mo thin films, various techniques such as chemical vapor deposition, physical vapor deposition (RF sputtering and DC sputtering) [1,8,9], and electron beam evaporation [10] have been reported in the literature. RF sputtering is the predominant technique for thin film deposition because of its benefits regarding layer adhesion, uniformity, composition, and deposition rate compared to other methods [11]. In the deposition of molybdenum films, RF sputtering allows for precise control of film thickness, shape, and stoichiometry, making it a key method for preparing films with specific characteristics [12].

Numerous approaches exist to improve the performance of thin films, including ion implantation techniques that enable precise alteration of material characteristics. Ion implantation is one of the most attractive techniques because it introduces considerable changes in the surface morphology and composition of the films [13,14]. The uses of implanted Mo thin films cover a broad range of applications including microelectronics and optoelectronics. One major use area is in microelectromechanical systems, where these films are used in parts such as microsensors, actuators, and microfluidic devices [15].

In this regard, the effects of different ion beams on the characteristics of Mo thin films have been explored [13-21]. Ahmed et al. [13] investigated the effect of helium ion irradiation on the structural and electrical properties of Mo thin films. They noted that α-particles create defects that reduce charge carrier mobility, and the hardness increased from low to high ion fluence. Hoffman et al. [14] investigated the effects of argon ion bombardment on the characteristics of Mo thin films. Films with reduced porosity and larger grains demonstrated increased reflectance and decreased resistivity, consistent with electron mean free path analysis results. Navin et al. [15] investigated self-organized pattern generation in Mo thin films with a low-energy argon ion beam (1 keV) across different ion fluences (10^{16}–10^{18} ions·cm^{-2}). Thornton et al. [16] examined a transition from tensile to compressive stress in argon-ion-implanted Mo thin films as the sputtering gas pressure decreased. Sun et al. [17] also analyzed the properties of argon-ion-implanted Mo thin films deposited via ion beam sputtering, varying deposition parameters such as accelerating voltage, incidence angle, and chamber pressure. Films deposited at near-normal incidence exhibited compressive stress and a nearly linear increase with the accelerating voltage. At grazing incidence, the observed stress is either minimal or slightly tensile and is mostly unaffected by the accelerating voltage. Tripathi et al. [18] examined the temperature-dependent surface alterations in Mo films induced by He^+ ion irradiation within the 773–1073 K range as a prospective substitute for tungsten in plasma-facing components of fusion devices. Klaver et al. [19] investigated the impact of irradiation with low-energy helium ions on the physical properties of molybdenum thin films. Ono et al. [20] studied the degradation of the optical characteristics of single- and polycrystalline Mo mirrors for plasma diagnostics when treated with low-energy He^+ ion irradiation at ambient temperature and 400 °C. Takamura et al. [21] examined the effects of He plasma irradiation on Mo thin films. The temperature range for nanostructure growth was within a temperature range of 800 to 1050 K, under incident helium ion energies of 50 to 100 eV. Nitrogen gas offers a fascinating opportunity for ion implantation in Mo thin films because of its high reactivity [22]. The incorporation of nitrogen ions alters the characteristics of Mo thin films, potentially improving their performance in a wide range of applications [23-28]. Kim et al. [23] examined the impact of a 3×10^{17} N_2^+·cm^{-2} ion fluence on the structural characteristics, surface morphology, and thermal stability of Mo thin films. The internal stress of these films transitioned from strongly compressive to weakly tensile after annealing. Lee et al. [24] efficiently incorporated nitrogen ions into epitaxial Mo films, forming a buried superconducting layer. They deposited atomically flat epitaxial Mo(110) films on Al_2O_3(0001) substrates. Carreri et al. [25] investigated high-temperature (800–1200 °C) plasma-based nitrogen ion implantation on molybdenum thin films. They also examined the phase development and tribological alterations caused by ion implantation. Furthermore, Nakano et al. [26] investigated the deterioration of optical characteristics in polycrystalline Mo mirrors exposed to irradiation with helium or deuterium ions. With increasing fluence and energy of the ions, a greater extent of deterioration was observed in helium-irradiated specimens than in deuterium-irradiated specimens. Mändl et al. [27,28] examined the impact of nitrogen ion implantation on Mo, focusing on nitride phase formation and nitrogen diffusion behavior within a temperature range of 330 to 580 °C. They observed the formation of a new cubic Mo_2N phase. In addition, they also examined the impact of high ion fluence and temperature on nitrogen implantation in molybdenum with supplementary heating within the temperature range of 500 to 750 °C.

It is well documented that ion beam implantation, including helium, nitrogen, and argon ions, is a versatile technique for tuning the properties of molybdenum thin films. Researchers examined the effects of ion fluence, implantation temperature, and ion energy on the characteristics of Mo thin films. Despite

these advances, a noticeable gap exists in the systematic exploration of nitrogen implantation with variations in the thickness of Mo films. To address this gap, this study employs an extensive approach, implementing low-energy nitrogen ion implantation with a systematic variation in film thickness and investigating the effects of these factors on the characteristics of molybdenum thin films. This study promotes the development of next-generation Mo thin films with precisely tuned characteristics. The findings of this research contribute to the optimization and development of Mo thin films for various applications in photovoltaics, sensors, optoelectronics, and electronic devices.

In the present work, Mo thin films with varying thickness of 150, 200, 250, and 300 nm were deposited on Si(100) substrates using radio frequency (RF) sputtering in an argon environment at ambient temperature. Some films with different thicknesses were implanted with 1×10^{17} $N_2^+ \cdot cm^{-2}$ at 30 keV using a current density of 4 $\mu A \cdot cm^{-2}$. This study illustrates the effects of nitrogen ion implantation and film thickness on the structural, optical, and electrical properties of thin molybdenum films.

Experimental

In this study, molybdenum thin films of varying thickness were deposited at room temperature on Si(100) substrates via RF sputtering using a pure 2″ diameter Mo target (99.99% purity) in Ar gas atmosphere with a flow rate of 10 sccm. The plasma was obtained by setting the RF power to 100 W, while careful minimizing the reflected power. Before deposition, the target surface was pre-sputtered for 15 min to remove any surface contamination. The silicon substrates were meticulously cleaned by washing them with distilled water and isopropyl alcohol and rinsing them with acetone. The vacuum chamber was evacuated to a base pressure of 2.0×10^{-3} mbar, with a working pressure during deposition of approximately 1.2×10^{-2} mbar; deposition times varied from 7 to 12 min, resulting in films with thicknesses from 150 to 300 nm, as measured by spectroscopic ellipsometry. After deposition, some films with different thicknesses were implanted with 1×10^{17} $N_2^+ \cdot cm^{-2}$ at 30 keV using a current density of 4 $\mu A \cdot cm^{-2}$.

The structural properties of the deposited Mo thin films were investigated using a GXRD Bruker AXS GmbH D8 Advance X-ray diffractometer in grazing incidence geometry, employing Cu Kα radiation with a wavelength of 1.5405 Å. Measurements were conducted with a fixed incident angle of 0.5°, and the X-ray tube was operated at 40 kV and 40 mA. The surface morphology was analyzed using a Bruker Multimode-8 atomic force microscopy (AFM). The optical characteristics of the molybdenum thin films were analyzed using a SENresearch 4.0 spectroscopic ellipsometer across a wide spectral range of 200–800 nm. The electrical properties of the films were evaluated using a Keithley 4200 A-SCS parametric analyzer equipped with two probes. All these analytical instruments are available at the Ion Beam Centre, Kurukshetra University, Kurukshetra, ensuring comprehensive and accurate characterization of the properties of Mo thin films.

Results and Discussion

SRIM-TRIM simulation

The “Stopping & Range of Ions in Matter and Transport of Ions in Matter” (SRIM-TRIM) simulation software was used to quantitatively estimate implantation-induced damages. These calculations provide detailed insights into the distribution of incident ions and the ion damage cascades within the molybdenum target material. The range of the nitrogen ions is 184 ± 98 Å, which is significantly less than the thickness of the thin films, as shown in Figure 1A,B.

The values for electronic energy losses and nuclear energy losses have been determined to be 25.6 and 18.2 $eV \cdot Å^{-1}$, respectively. Both energy loss processes have values within a similar range, which suggests that contributions from both processes are approximately equivalent in their effect on the target material. This balance highlights the importance of electronic and nuclear interactions in the energy transfer processes during ion implantation. Furthermore, of the total energy of 15 keV from a single nitrogen ion, 8.5 keV produce ionization, while 6.2 keV generate phonons, and 0.29 keV create damage within the target material, as demonstrated in Figure 1C.

These findings highlight the significant interactions between the nitrogen ions and the molybdenum target material during the implantation process, providing valuable insights into the mechanisms that govern ion implantation and the subsequent alterations in the material properties. As indicated by the TRIM simulations, a single nitrogen ion with this energy can produce 95 displacements, that is, 95 vacancies and no replacement collisions, before coming to a stop, as illustrated in Figure 1D. This significant level of displacement underscores the ions’ capacity to induce damage within the target material.

Structural characteristics

Figure 2 depicts the GXRD patterns of as-deposited and implanted Mo thin films (at an ion fluence of 1×10^{17} $N_2^+ \cdot cm^{-2}$) with different thicknesses of 150, 200, 250, and 300 nm. The patterns indicate the face-centered cubic Mo phase, as per JCPDS no. 01-088-2331 [29].

In Figure 2A, there is a notable reduction in peak intensity of the Mo film after N_2^+ implantation relative to the as-deposited

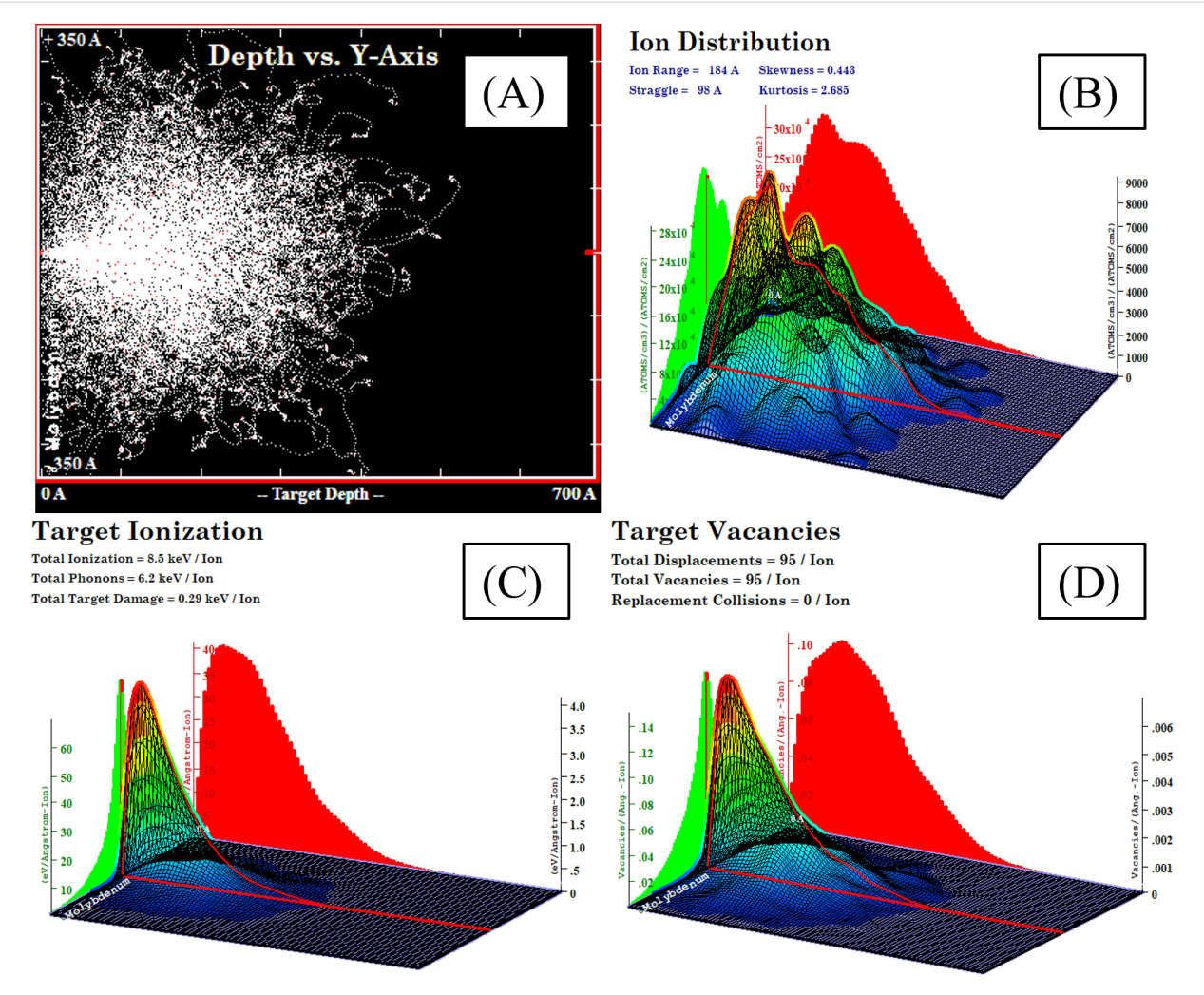

Figure 1: (A) Nitrogen ion trajectories, (B) distribution of ions, (C) distribution of losses due to ionization, and (D) vacancy distribution in a Mo thin film.

Mo film. This reveals a significant alteration in structure due to the implantation process. Similarly, in Figure 2B–D, the peak intensity of implanted Mo films decreases in comparison to the as-deposited Mo films of the same nominal thickness. This reduced intensity of diffraction peaks is attributed to amorphization and degradation of the structure by N_2^+ implantation. However, the peak intensity of the as-deposited Mo films increased with increasing thickness. This trend of intensity with thickness remains in the nitrogen-implanted films. At lower thicknesses (150 and 200 nm), crystallinity is significantly reduced because of the extensive penetration of nitrogen ions, resulting in considerable distortion of the material structure. In contrast, films of 250 and 300 nm maintain a degree of crystallinity derived from the unexposed bulk layer under the ion-implanted layer [30].

The full width at half maximum (FWHM) of diffraction peaks was evaluated from the prominent peak at 2θ = 37.80° associated with the (111) crystallographic plane. Further, the average crystallite size was calculated using the Scherrer equation [31-33]:

$$D = \frac{k\lambda}{\beta \cos\theta,} \quad (1)$$

where k is a constant (k = 0.94) [32,33], λ is the X-ray wavelength (λ = 1.5406 Å), θ is the Bragg angle, and β is the FWHM.

Additionally, the microstrain (ε) developed in the thin films due to lattice distortions or mismatch was calculated using Wilson's equation [31,33]:

$$\varepsilon = \frac{\beta}{4\tan\theta}. \quad (2)$$

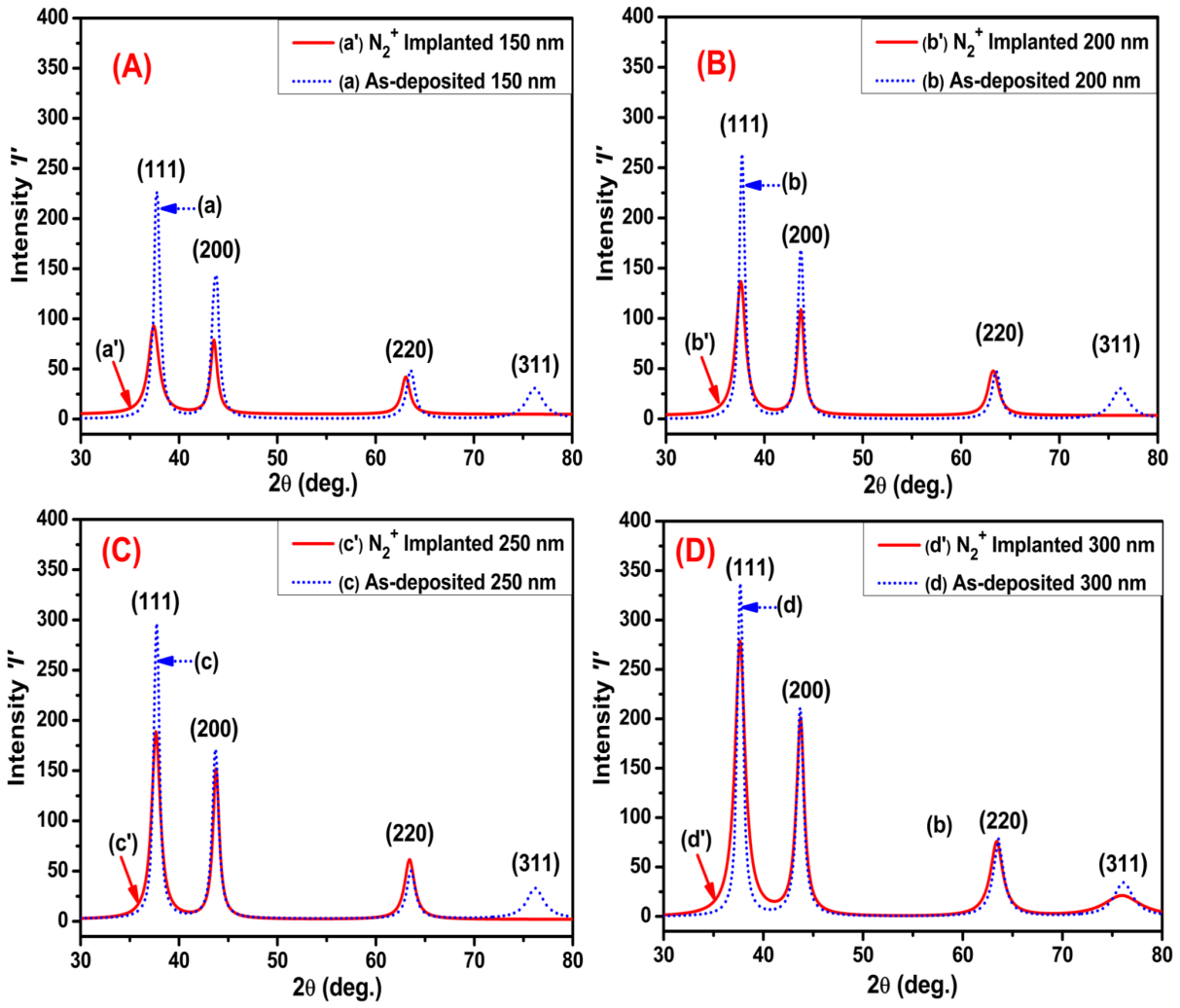

Figure 2: GXRD patterns of as-deposited and N_2^+-implanted Mo thin films. (A) 150 nm, (B) 200 nm, (C) 250 nm, and (D) 300 nm.

The dislocation density (δ) gives more information about the number of defects in the films; it was calculated from the relation [32]:

$$\delta = \frac{1}{D^2}, \tag{3}$$

where D is the average crystallite size.

The interplanar spacing (d) and lattice constant (a) were calculated using the relations [13,33]:

$$d = \frac{\lambda}{2\sin\theta} \text{ and} \tag{4}$$

$$a = d\sqrt{h^2 + k^2 + l^2}, \tag{5}$$

where $h,k,$ and l are the Miller indices of the corresponding diffraction peak [34]. The obtained values for average crystallite size, microstrain, dislocation density, and interplanar spacing for as-deposited and N_2^+-implanted Mo films are summarized in Table 1.

Table 1 shows that the FWHM decreases with increase in film thickness. This reveals an enhancement in crystallite size and uniformity, signifying improved crystallinity in the films. However, after N_2^+ implantation, the FWHM increases significantly. The crystallite size of the as-deposited and N_2^+-implanted Mo films increases from 13.22 to 15.24 nm and from 11.92 to 14.42 nm with an increase in thickness from 150 to 300 nm, respectively. This variation may relate to several factors involving film growth and substrate interactions. Thicker films (i.e., 250 and 300 nm) exhibit less surface diffusion effects during deposition, promoting better crystal formation and atomic plane

Table 1: Structural parameters of as-deposited and implanted Mo thin films.

Serial number	Sample	2θ (°) of the (111) peak	FWHM	Crystallite size *D* (nm)	Microstrain ε (× 10^{-3})	Dislocation density δ (× 10^{15} nm^{-2})	Interatomic spacing *d*(111) (Å)
1	as-deposited 150 nm	37.75	0.603	13.202 ± 1.051	7.542	5.951	2.381
2	N_2^+-implanted 150 nm	37.40	0.706	11.921 ± 0.953	9.041	7.032	2.389
3	as-deposited 200 nm	37.73	0.584	14.424 ± 1.131	7.431	4.801	2.382
4	N_2^+-implanted 200 nm	37.57	0.685	12.882 ± 1.320	8.745	6.631	2.388
5	as-deposited 250 nm	37.71	0.570	14.981 ± 1.101	7.252	4.472	2.384
6	N_2^+-implanted 250 nm	37.60	0.654	13.871 ± 0.789	8.344	5.191	2.387
7	as-deposited 300 nm	37.67	0.552	15.242 ± 1.033	7.041	4.306	2.385
8	N_2^+-implanted 300 nm	37.62	0.627	14.424 ± 0.848	7.981	4.802	2.386

organization. The increased film thickness may also enable more volume for the formation of ordered crystalline domains [35,36].

After N_2^+ implantation, the crystallite size decreased significantly relative to as-deposited Mo films of the same nominal thickness, as illustrated in Table 1. Nitrogen ions during implantation induced many lattice defects, including point defects, dislocations, and distortions, in the Mo crystal lattice, resulting in microstructural disorder and amorphization. The simultaneous impact of strain and defects leads to peak broadening and increase of the FWHM. The disruption of the crystal lattice and an increasing number of defects substantially influenced the grain boundaries, resulting in a notable alteration of the structural parameters of Mo thin films. Additionally, Table 1 shows that microstrain and dislocation density increased after implantation. The interplanar spacing of Mo thin films increased with film thickness [13,34].

Figure 3 shows the GXRD pattern for (111) diffraction peaks of as-deposited and implanted Mo thin films. The (111) peak position shifts slightly to smaller Bragg angles after N_2^+ implantation. This shift becomes less pronounced as the thickness increases, indicating an increase in the average interplanar spacing according to Bragg's law [29,35]. The change in interplanar spacing is attributed to the strain associated with residual stress in the Mo film. The stress induced in the films is calculated using the formula [13,33,37]

$$s = \frac{E_f\left(d_0 - d\right)}{2\nu_f d_0}, \tag{6}$$

where E_f is the Young's modulus, ν_f represents the Poisson's ratio, d_0 corresponds to the bulk interplanar spacing, and d is the calculated interplanar spacing. The material parameters for Mo are E_f = 320 GPa, ν_f = 0.3 [13,33,37], and d_0 = 2.3867 Å [37] (JCPDS Card No. 01-088-2331). The obtained values of stress are plotted in Figure 4.

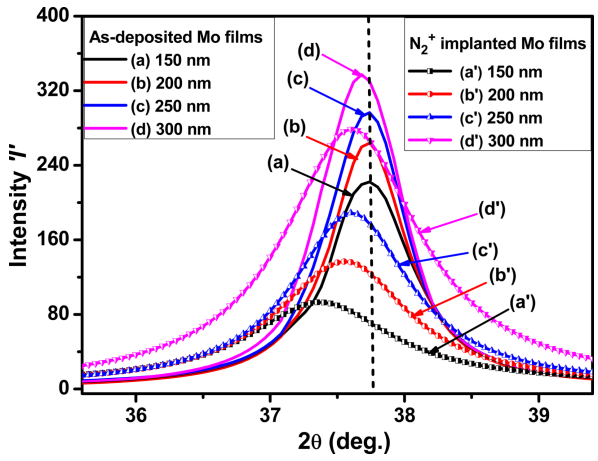

Figure 3: GXRD pattern of the (111) diffraction peak of as-deposited and N_2^+-implanted Mo thin films (a, a′) 150 nm, (b, b′) 200 nm, (c, c′) 250 nm, and (d, d′) 300 nm.

The as-deposited molybdenum thin films exhibited tensile stress, with the degree of this stress decreasing with an increase in film thickness. After nitrogen ion implantation, the stress in the films changed from tensile to compressive, as illustrated in Figure 4. The X-ray diffraction (XRD) peak position shift provides further insight into these stress changes. In as-deposited films, the peaks are shifting to lower 2θ values, signifying an increase in interatomic separation, which aligns with the measured tensile stress. In the nitrogen-implanted films, all peaks are shifted to reduced 2θ values compared to the as-deposited films, indicating compressive stress. Nevertheless, the peak positions for the implanted films shifted towards increasing 2θ values as the film thickness increased from 150 to 300 nm, signifying a reduction in interplanar spacing. The decrease in interplanar spacing is a direct consequence of the compressive force induced by nitrogen implantation.

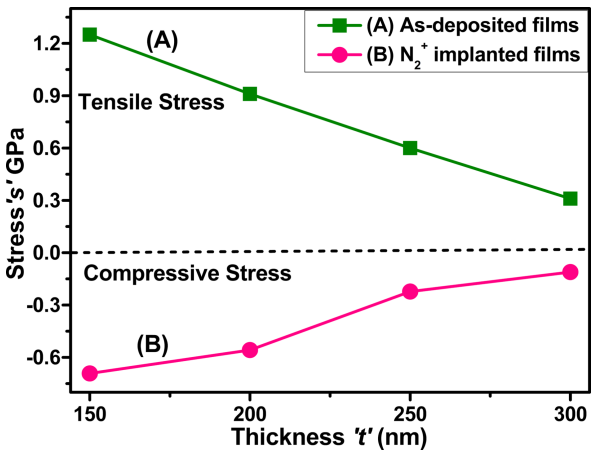

Figure 4: Stress in (A) as-deposited and (B) N_2^+-implanted Mo thin films as a function of the thickness.

During the deposition process, Mo thin films exhibit different types of stress due to changes in microstructure and the interplay of intrinsic and extrinsic stress mechanisms. Figure 4 shows that the tensile stress in as-deposited Mo thin films decreases from 1.25 to 0.31 GPa as the film thickness increases from 150 to 300 nm, attributed to the relaxation of intrinsic stress induced during deposition. At lower thickness, the films exhibit higher tensile stress due to grain boundary contacts and point defects generated during the first phase of film growth. The increased thickness of films led to larger crystallites and improved crystallinity, which reduced tensile stress by decreasing atomic-scale defects and strain [13,29]. The compressive stress increases from −0.69 to −0.11 GPa as the thickness of nitrogen-implanted Mo thin films increases from 150 to 300 nm. Nitrogen ion implantation plays an important role in altering the stress state from tensile to compressive. This process can be explained by the introduction of nitrogen ions into the film structure. This generates compressive stress due to the presence of implanted nitrogen atoms in interstitial positions within the Mo lattice, leading to lattice distortion [38].

As the film thickness increases, nitrogen ions are dispersed over more volume, enhancing the cumulative distortion effects inside the films. Furthermore, nitrogen implantation improves densification and modifies the crystal structure. Nitrogen ions serve as a barrier in boundary relaxation and grain growth, hence increasing the stress. The divergent behavior illustrates the significant influence of nitrogen inclusion on the stress evolution of Mo thin films.

The crystalline orientation of the Mo films along a particular (*hkl*) plane can be quantified by determining the texture coefficient (TC_{hkl}), which is determined by the following equation [39,40]:

$$TC_{hkl} = \frac{I(hkl)}{I(111)+I(200)+I(220)+I(311)}, \quad (7)$$

where *hkl* represents the (111), (200), (220), or (311) orientations. The calculated TC_{hkl} values for each Mo thin film are summarized in Table 2.

The texture coefficients of as-deposited and N_2^+-implanted Mo thin films demonstrate a strong orientation preference in the (111) direction. The TC_{111} values of these films are significantly larger than those for other orientations. Also, the texture coefficient for the (200) plane, though less than that for the (111) plane, is larger than those for the (220) and (311) planes. These observations reveal that the plane (111) is the dominant crystalline orientation in both as-deposited and nitrogen-implanted Mo thin films. The (111) plane in face-centered cubic structures, such as Mo, typically has the lowest surface energy [35]. Therefore, atoms tend to arrange themselves to minimize

Table 2: Lattice constants and texture coefficients of as-deposited and implanted Mo thin films.

Serial number	Sample	Lattice constant *a* (Å)	Texture coefficient			
			$TC_{(111)}$	$TC_{(200)}$	$TC_{(220)}$	$TC_{(311)}$
1	as-deposited 150 nm	4.124	0.501	0.302	0.104	0.054
2	N_2^+-implanted 150 nm	4.139	0.433	0.364	0.172	0.000
3	as-deposited 200 nm	4.126	0.511	0.311	0.110	0.057
4	N_2^+-implanted 200 nm	4.138	0.462	0.373	0.183	0.000
5	as-deposited 250 nm	4.129	0.518	0.328	0.118	0.059
6	N_2^+-implanted 250 nm	4.135	0.482	0.384	0.189	0.000
7	as-deposited 300 nm	4.133	0.525	0.331	0.126	0.061
8	N_2^+-implanted 300 nm	4.134	0.492	0.391	0.191	0.035

the overall energy, leading to a predominant (111) orientation. This tendency is even more pronounced for as-deposited films, where the absence of any external influence would have allowed for the natural minimization of surface energy. Nitrogen ion implantation could change the crystalline orientation through defects and stress introduced in the Mo thin films. The residual stress due to the implantation may also be an influential factor regarding the preferred orientation. If the applied stress promotes the (111) orientation, this plane will be more pronounced in the resultant thin film [9].

Additionally, the texture coefficients increase with the thickness for both as-deposited and implanted Mo thin films. Thicker films (i.e., 250 and 300 nm) generally exhibit stronger orientation preferences because of the increased volume for developing certain planes. In contrast, thinner films (i.e., 150 and 200 nm) exhibit a specific orientation preference owing to the restricted volume, which restricts the formation of certain planes [41]. Furthermore, the interaction between the substrate and the thin film can generate stress and strain, affecting the growth of specific planes. If the substrate promotes the (111) orientation through lattice compatibility, the resultant Mo thin film exhibits a pronounced (111) orientation.

Crystallite size and texture coefficients of these Mo thin films significantly increase with the thickness of Mo thin films. Moreover, a significant reduction has been observed in both these parameters after nitrogen implantation compared to equivalently thick as-deposited films. The increase in crystallite size with greater film thickness directly signifies enhanced crystallinity, observable by the formation of larger crystallites in thicker films. Additionally, the texture coefficient rises, signifying that crystallites attain a more uniform orientation in the film.

Surface morphology

Figure 5 depicts 2 × 2 μm^2 2D and 3D AFM images of as-deposited and implanted (at an ion fluence of 1×10^{17} $N_2^+ \cdot cm^{-2}$) Mo thin films. Figure 5a reveals that the 150 nm thick Mo film exhibits a surface with thinner and more elongated rough peaks [42]. In this stage of deposition, the particles exhibit granular, tightly packed vertical peak growth. After nitrogen implantation (Figure 5a′), the shape altered into broader and more flatter characteristics [42]. This may be because of surface alterations induced by the N_2^+ implantation [9,42]. Interestingly, variations in Mo film thickness from 150 to 300 nm also led to noticeable changes in morphology. With

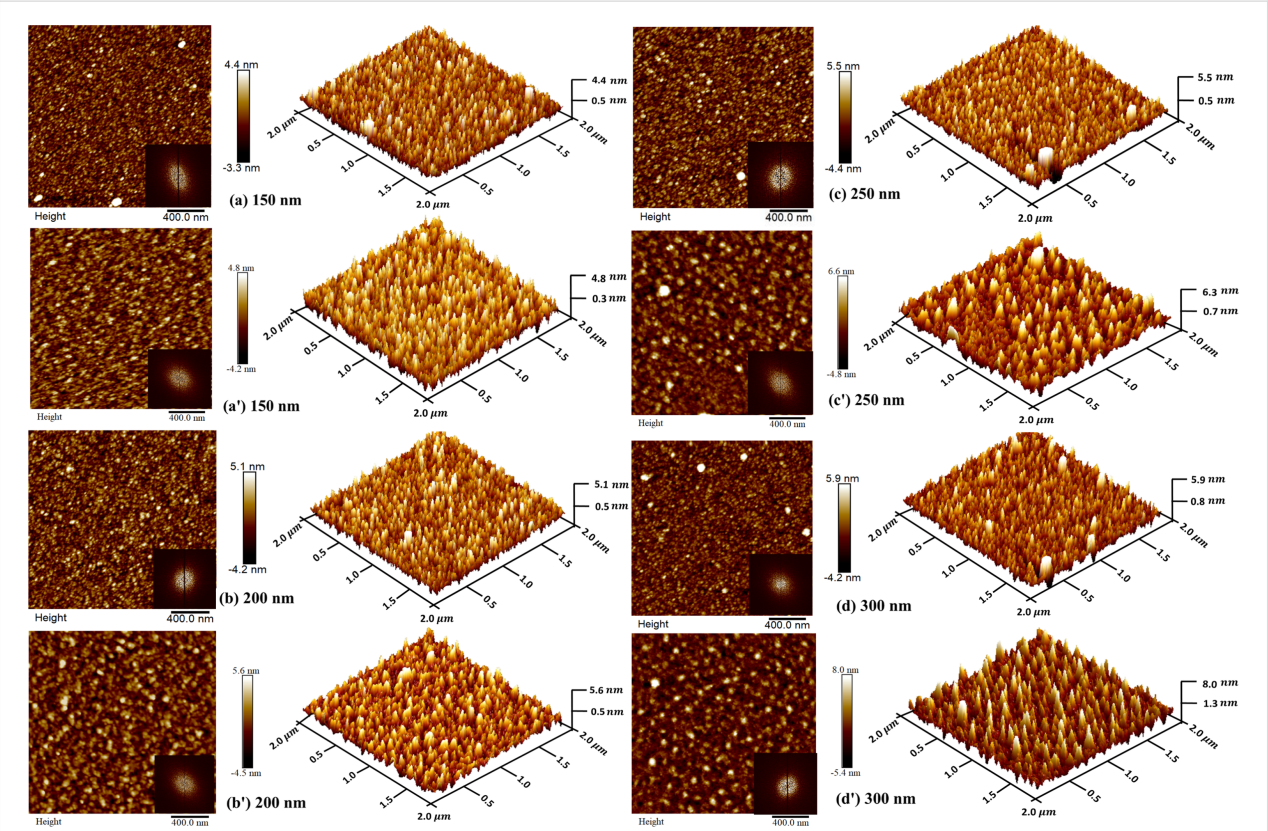

Figure 5: 2D and 3D AFM images of Mo thin films: as-deposited (a) 150 nm, (b) 200 nm, (c) 250 nm, and (d) 300 nm, and implanted (a′) 150 nm, (b′) 200 nm, (c′) 250 nm, and (d′) 300 nm. The fast Fourier transform images are insets in the 2D AFM micrographs.

the increase in thickness, rough peaks evolved into broader and flatter shapes. The fast Fourier transform images indicate random distribution with different orientations of particles. The surface morphology parameters are listed in Table 3. The RMS roughness values of Mo thin films with 150, 200, 250, and 300 nm thickness are around 1.09, 1.23, 1.41, and 1.73 nm, respectively. After N_2^+ implantation, the RMS roughness increases to 1.28, 1.43, 1.58, and 1.89 nm, respectively. A similar trend in roughness has been observed after N_2^+ implantation for all Mo films. Table 3 reveals a continuous increase in particle size with Mo film thickness before and after N_2^+ implantation.

Table 3: Values of RMS surface roughness and particle size of as-deposited and implanted Mo thin films.

Serial number	Sample	Roughness (nm)	Particle size (nm)
1	as-deposited 150 nm	1.09 ± 0.11	67.41 ± 0.88
2	N_2^+-implanted 150 nm	1.28 ± 0.21	100.71 ± 1.23
3	as-deposited 200 nm	1.23 ± 0.32	73.26 ± 1.21
4	N_2^+-implanted 200 nm	1.43 ± 0.12	106.41 ± 1.11
5	as-deposited 250 nm	1.41 ± 0.14	80.86 ± 1.24
6	N_2^+-implanted 250 nm	1.58 ± 0.28	113.24 ± 1.31
7	as-deposited 300 nm	1.73 ± 0.16	88.24 ± 1.40
8	N_2^+-implanted 300 nm	1.89 ± 0.21	119.86 ± 1.43

This increase in roughness and particle size is related to structural alterations due to the increasing film thickness. At the lowest thickness, a greater number of particles are found to be small [43]. As the thickness of Mo thin films increases, smaller particles coalesce, which increases the surface roughness. The increase in roughness and particle size of implanted films results from structural modifications caused by N_2^+ implantation. AFM analysis reveals that N_2^+ implantation and thickness of films significantly influence the surface morphology of Mo thin films.

Optical properties

Spectroscopic ellipsometry

Figure 6 depicts the fit of the spectroscopic ellipsometry data in which the parameters of the Drude–Lorentz oscillator model were adjusted. In ellipsometry, the two parameters ψ and Δ characterize a change in polarization state. ψ denotes the amplitude ratio between p-polarized (parallel to the plane of incidence) and s-polarized (perpendicular to the plane of incidence) light components after interaction with the sample. Δ denotes the phase difference between these components after contact with the sample. Upon successfully fitting the results of N_2^+-implanted molybdenum thin films for all thickness, a small error percentage (in this case, 0.15%) between the experimental and simulated curves is observed, indicating a close match [2,44]. The simulated curves derived from the fit process validate the results and offer a theoretical framework for understanding the optical properties of molybdenum thin films.

Absorbance spectra

The absorption spectra of Mo thin films in Figure 7 show the effects of nitrogen ion implantation and film thickness on the production of Mo nanoparticles and the subsequent increase in surface plasmon resonance or interband transitions. As-deposited molybdenum thin films deposited at room temperature typically exhibit a smooth surface and crystalline structure. The absorbance of molybdenum thin films increases with increasing film thickness and peaks between 300 and 700 nm, corresponding to the localized surface plasmon resonance (LSPR) of molybdenum nanoparticles [45,46].

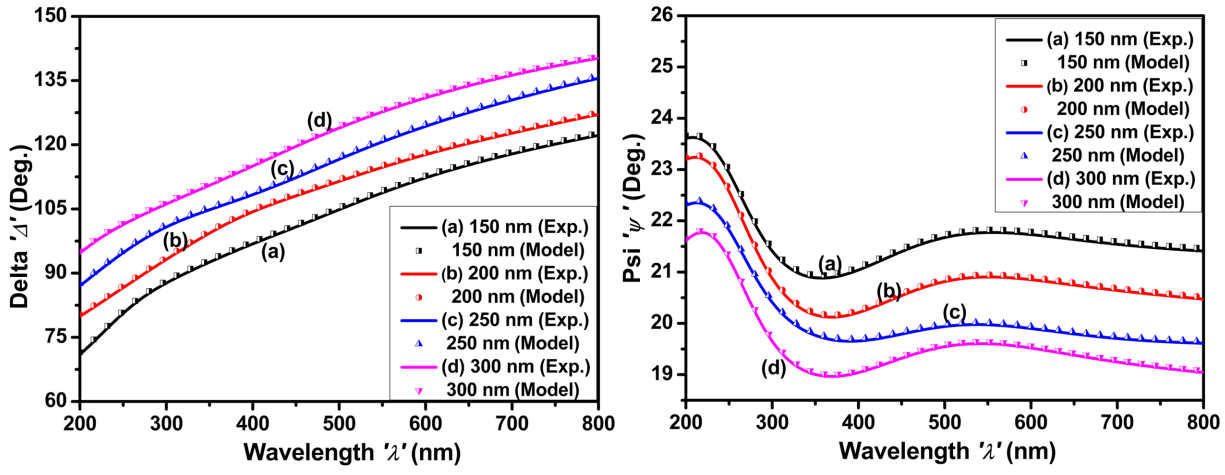

Figure 6: Measured SE data (solid line) and fit (symbols) of ψ and Δ spectra as functions of the wavelength of N_2^+-implanted molybdenum thin films with thicknesses of (a) 150 nm, (b) 200 nm, (c) 250 nm, and (d) 300 nm.

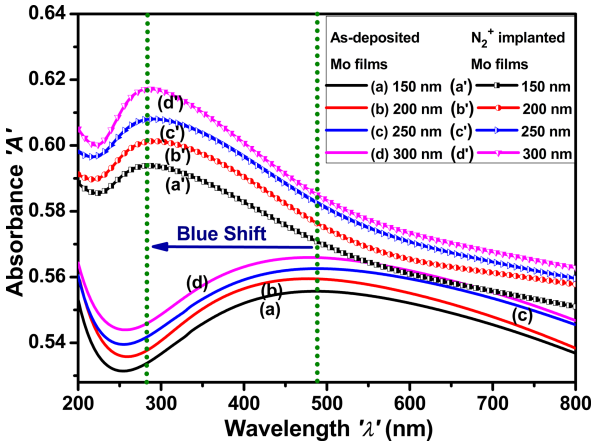

Figure 7: Absorbance spectra of as-deposited and N_2^+-implanted Mo thin films with thicknesses of (a, a′) 150 nm, (b, b′) 200 nm, (c, c′) 250 nm, and (d, d′) 300 nm.

The formation of defects through ion irradiation increased the scattering of light and absorption within the film, resulting in enhanced overall absorbance of Mo thin films. The blue shift of the LSPR band to a shorter wavelength (i.e., 260–340 nm) after nitrogen ion implantation can be attributed to modifications in the size, shape, and density of molybdenum nanoparticles [47]. The absorbance bands are more pronounced after nitrogen implantation because of defects that facilitate the growth of smaller nanoparticles or cause aggregation, consequently altering the plasmonic characteristics of the material.

Reflectance spectra

Figure 8 shows the reflectance spectra as-deposited and implanted Mo thin films as functions of the thickness. The dip observed in the reflectance spectra of Mo films between 300 and 700 nm is attributed to the LSPR of Mo nanoparticles. The peak observed in the reflectance spectra at approximately 260 nm correlates with the dip in absorbance [48]. A notable enhancement in the reflectance of Mo thin films is observed as a function of the film thickness. Ion implantation induces many alterations in the reflectance spectra. The shift of the peak to shorter wavelengths (about 225 nm) shows a change in the electrical structure of the Mo thin film, probably due to defect formation. These defects can modify the plasmonic behavior of the nanoparticles, influencing their resonance properties and, subsequently, the absorbance spectrum [49]. Furthermore, the alteration in peak location indicates an increased number of nanoparticles or a modification in their size distribution resulting from damage caused by ion implantation.

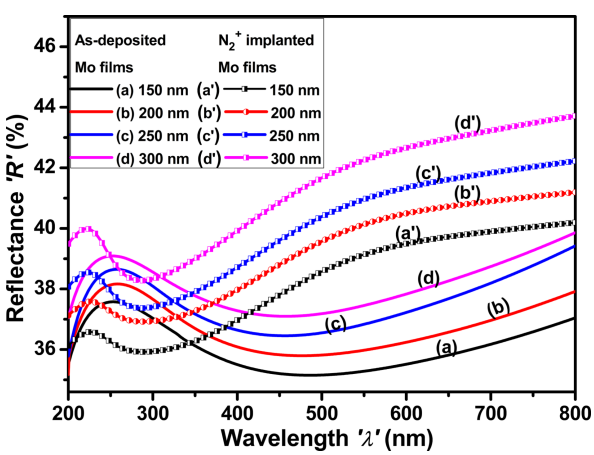

Figure 8: Reflectance spectra of as-deposited and N_2^+-implanted Mo thin films with thicknesses of (a, a′) 150 nm, (b, b′) 200 nm, (c, c′) 250 nm, and (d, d′) 300 nm.

Refractive index

Figure 9 shows the refractive index of as-deposited and implanted Mo thin films as a function of the thickness. The refractive index increases after N_2^+ implantation because of several factors, notably the formation of defects and changes in the composition and structure of Mo thin films. There is a dip in the refractive index between 300 and 700 nm, attributed to the LSPR of molybdenum nanoparticles. Defects include interstitials, vacancies, and structural deformation, which modify the electrical and lattice structure of the material [49,50]. The refractive index of both as-deposited and implanted Mo thin films increases with increasing film thickness. The increased refractive index suggests increased particle density and a better interaction between light and Mo thin films.

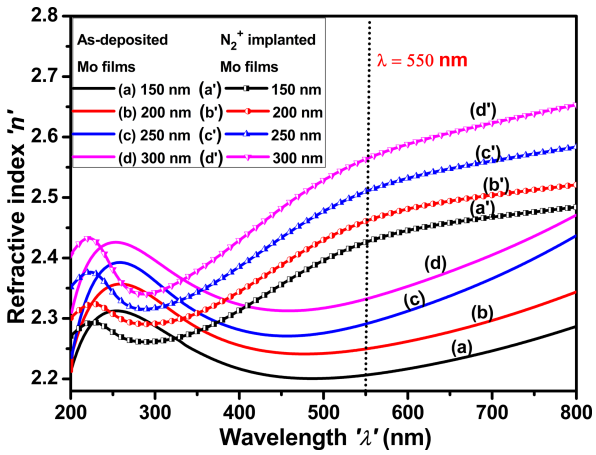

Figure 9: Refractive index of as-deposited and N_2^+-implanted Mo thin films with thicknesses of (a, a′) 150 nm, (b, b′) 200 nm, (c, c′) 250 nm, and (d, d′) 300 nm.

Electrical properties

Figure 10 shows the current–voltage (*I*–*V*) characteristics of the as-deposited and implanted Mo thin films as a function of thick-

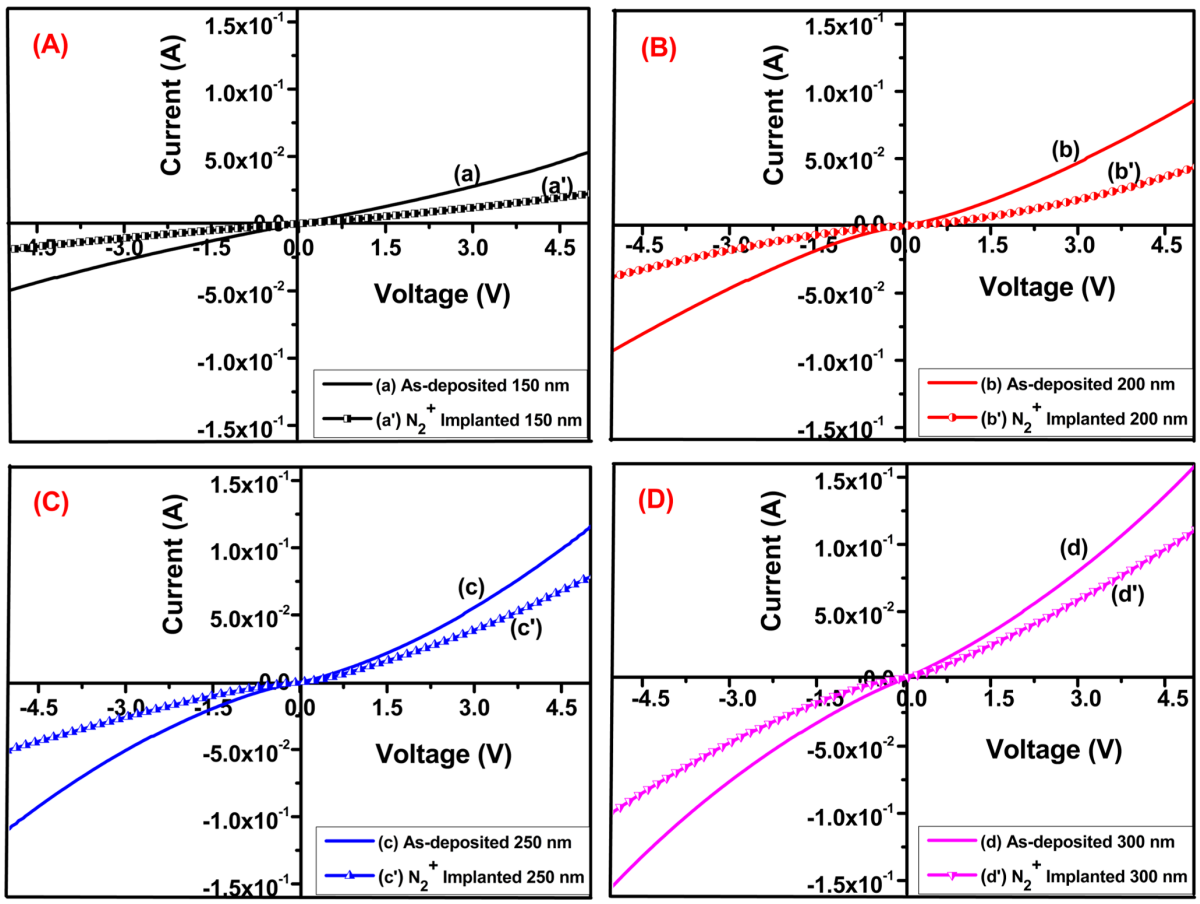

Figure 10: Current–voltage characteristics of as-deposited and N_2^+-implanted Mo thin films with thicknesses of (A) 150 nm, (B) 200 nm, (C) 250 nm, and (D) 300 nm.

ness. *I*–*V* curves have been obtained within a voltage range of −5 to 5 V. A nearly linear relationship between applied voltage and the resulting current indicates ohmic behavior [51]. Resistance and resistivity of the Mo thin films have been calculated based on the slope of the *I*–*V* curve. The observed increase in current across the thin films suggests their superior electrical conductivity. Such characteristics are highly desirable for various electronic and electrical applications where efficient electrical conduction is paramount.

The stress in the films may influence the electrical properties. As the thickness changes, the internal stress distribution could lead to impediments in electron transport, causing slight deviations from linearity. Nitrogen ions create defects, vacancies, or impurities in the molybdenum film, acting as scattering centers for charge carriers. Ion implantation may also create localized states within the film, causing some charge carriers to become trapped. This affects the charge transport mechanism, leading to slight nonlinearities. The ion implantation causes modifications in the grain structure of the molybdenum thin films. Such structural changes can influence the movement of electrons through the material, particularly at grain boundaries, resulting in nonlinear *I*–*V* behavior.

Resistivity and conductivity

The resistivity of thin films is defined by the relation [51,52]:

$$\rho = R\frac{A}{l}, \tag{8}$$

where ρ is the resistivity, R is the resistance, A represents the area of the thin molybdenum film samples (width of film × thickness of film), and l corresponds to the length between the two probes. The relationship between resistivity and conductivity is [51]:

$$\sigma = \frac{1}{\rho}, \tag{9}$$

Table 4: The electrical parameters of as-deposited and implanted Mo thin films.

Serial number	Thickness '*t*' (nm)	Resistance '*R*' (Ω)	Resistivity ρ (× 10^{-3} Ω·cm)	Conductivity σ (× 10^{2} S·cm^{-1})
1	as-deposited 150 nm	101	1.51	6.62
2	N_2^+-implanted 150 nm	160	2.56	3.90
3	as-deposited 200 nm	72	1.44	6.94
4	N_2^+-implanted 200 nm	117	2.40	4.18
5	as-deposited 250 nm	55	1.37	7.27
6	N_2^+-implanted 250 nm	90	2.25	4.44
7	as-deposited 300 nm	45	1.32	7.57
8	N_2^+-implanted 300 nm	68	2.07	4.84

where σ represents the conductivity of thin films, and ρ corresponds to the resistivity of thin molybdenum films. The resistivity of the films increases after implantation but reduces as the thickness of the film increases from 150 to 300 nm, as summarized in Table 4.

The conductivity of as-deposited Mo thin films increases from 6.62 × 10^2 to 7.57 × 10^2 S·cm^{-1} when the film thickness increases from 150 to 300 nm. This can be ascribed to the increased conducting pathways in thicker films. These channels provide more pathways for electrons to flow, enhancing conductivity. Conversely, the conductivity of the thin molybdenum films tends to decrease after N_2^+ implantation for films with the same nominal thickness [32,53]. The resistivity of as-deposited and implanted molybdenum thin films with different thickness is illustrated in Figure 11.

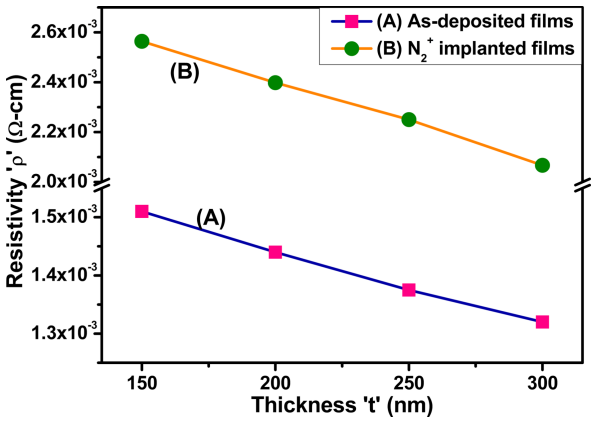

Figure 11: Resistivity of (A) as-deposited and (B) N_2^+-implanted Mo thin films as a function of the thickness.

The increase in resistivity after nitrogen implantation is linked to the decreased crystalline quality of molybdenum thin films. After implantation, various grain boundaries disrupt the crystal structure. These boundaries act as obstacles for charge carriers, hindering their movement and thus increasing resistivity. Further, scattering at these boundaries reduces the mobility of charge carriers, leading to a decrease in conductivity. Essentially, the more boundaries present after implantation, the greater the scattering effect [32]. As the thickness of the films increases, their conductivity increases. This is because thicker films have a denser microstructure. More atoms are packed closely in thicker films, creating a more efficient pathway for electrical current to travel [54]. The increase in conductivity with thickness is beneficial for applications such as interconnects and conductive traces in microelectronic devices, where efficient electrical conduction is crucial. Overall, ion implantation with a nitrogen ion beam under the specified conditions affects the conductivity of molybdenum thin films by introducing defects, modifying the crystal structure, doping the material with nitrogen ions, and potentially improving surface characteristics.

Correlation of structural, optical, and electrical parameters with thickness

Figure 12 depicts the mutual correlations between the structural, optical, and electrical parameters of both as-deposited and N_2^+-implanted Mo films as a function of film thickness. The crystallite size of the as-deposited Mo films increased with increasing thickness, signifying a more defined crystalline structure. This trend persists even after ion implantation, with a reduction in crystallite size due to structural alterations and defects introduced by the ion implantation process. After N_2^+ implantation, the refractive index increased due to defects created by the implantation, which modified the crystal structure and resulted in a denser, optically distinct material. Similarly, the electrical conductivity of the as-deposited Mo films increased with increasing thickness, as thicker films often provide better pathways for electron conduction because of less scattering effects. However, after implantation, several grain boundaries are compromising the crystalline structure. These barriers act as obstacles for charge carriers, obstructing their mobility and increasing resistivity. This results in a reduction in conductivity.

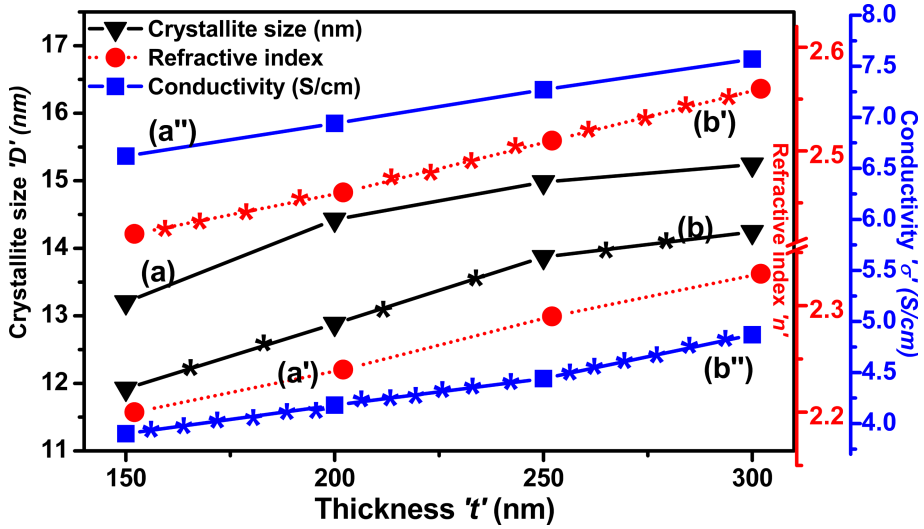

Figure 12: Mutual correlation between (a, b) crystallite size, (a′, b′) refractive index, and (a″, b″) conductivity and thickness of the Mo films. (a), (a′) and (a″) stand for as-deposited and (b), (b)′, and (b″) stand for N_2^+-implanted Mo thin films.

Despite this reduction, the conductivity also increased in implanted films.

Conclusion

This study gives comprehensive insights into the structural, morphological, optical, and electrical properties of Mo thin films of varying thickness deposited on Si(100) substrates by RF sputtering. Some of these films have been implanted with 1×10^{17} $N_2^+ \cdot cm^{-2}$ at 30 keV. GXRD showed that crystallite size and texture coefficients of Mo thin films enhanced with thickness in as-deposited films, indicating improved crystallographic order and diminishing dislocations and microstrain. This trend with film thickness persists even after N_2^+ implantation. After implantation, these parameters significantly decrease relative to as-deposited films with the same nominal thickness. Structural analysis also shows a shift of peaks towards lower 2θ values, indicating that the tensile stress in as-deposited Mo thin films changes to compressive stress after implantation. The AFM analysis shows that RMS roughness increases with thickness in both as-deposited and implanted films. The RMS roughness significantly increases upon implantation. Optical studies using SE show a significant increase in absorbance and reflectance in both as-deposited and N_2^+-implanted films. The absorbance peak and reflectance spectra dip correspond to molybdenum nanoparticles. Electrical investigations showed that conductivity increases with the film thickness in both as-deposited and implanted films, but decreases upon implantation for the corresponding films with the same nominal thickness. The findings suggest that nitrogen ion implantation can tailor the properties of Mo thin films, enhancing their performance in applications such as photovoltaic devices, energy storage, and integrated circuits.

Funding

Usha Rani is thankful to CSIR, New Delhi, for providing the CSIR-JRF. The authors are also grateful to the Department of Science and Technology (DST), New Delhi, for providing funds for establishing the 200 kV ion accelerator and related characterization facilities at Kurukshetra University, Kurukshetra. The authors are also thankful to the Ministry of Human Resources and Development (MHRD) for RUSA 2.0 grants to the Centre for Advanced Material Research (CAMR), Kurukshetra University, Kurukshetra.

Author Contributions

Usha Rani: conceptualization; formal analysis; investigation; methodology; writing – original draft. Kafi Devi: investigation; methodology; visualization; writing – original draft. Divya Gupta: conceptualization; investigation; validation; writing – review & editing. Sanjeev Aggarwal: conceptualization; supervision; validation; visualization; writing – review & editing.

ORCID® iDs

Usha Rani - https://orcid.org/0009-0007-8584-0189
Divya Gupta - https://orcid.org/0000-0002-9879-8553
Sanjeev Aggarwal - https://orcid.org/0000-0002-0054-4679

Data Availability Statement

Data generated and analyzed during this study is available from the corresponding author upon reasonable request.

References

1. Battu, A. K.; Makeswaran, N.; Ramana, C. V. *J. Mater. Sci. Technol.* **2019,** *35,* 2734–2741. doi:10.1016/j.jmst.2019.05.023

2. Makeswaran, N.; Orozco, C.; Battu, A. K.; Deemer, E.; Ramana, C. V. *Materials* **2022,** *15,* 754. doi:10.3390/ma15030754
3. Chelvanathan, P.; Zakaria, Z.; Yusoff, Y.; Akhtaruzzaman, M.; Alam, M. M.; Alghoul, M. A.; Sopian, K.; Amin, N. *Appl. Surf. Sci.* **2015,** *334,* 129–137. doi:10.1016/j.apsusc.2014.08.154
4. Zhou, D.; Zhu, H.; Liang, X.; Zhang, C.; Li, Z.; Xu, Y.; Chen, J.; Zhang, L.; Mai, Y. *Appl. Surf. Sci.* **2016,** *362,* 202–209. doi:10.1016/j.apsusc.2015.11.235
5. Khalil, M. I.; Bernasconi, R.; Lucotti, A.; Le Donne, A.; Mereu, R. A.; Binetti, S.; Hart, J. L.; Taheri, M. L.; Nobili, L.; Magagnin, L. *J. Appl. Electrochem.* **2021,** *51,* 209–218. doi:10.1007/s10800-020-01494-1
6. Bredell, L. J.; van der Berg, N. G. *Surf. Coat. Technol.* **1998,** *103-104,* 118–123. doi:10.1016/s0257-8972(98)00386-7
7. Guillén, C.; Herrero, J. *J. Mater. Process. Technol.* **2003,** *143-144,* 144–147. doi:10.1016/s0924-0136(03)00395-9
8. Jubault, M.; Ribeaucourt, L.; Chassaing, E.; Renou, G.; Lincot, D.; Donsanti, F. *Sol. Energy Mater. Sol. Cells* **2011,** *95,* S26–S31. doi:10.1016/j.solmat.2010.12.011
9. Jia, X.; Lin, Z.; Yang, T. C.-J.; Puthen-Veettil, B.; Wu, L.; Conibeer, G.; Perez-Wurfl, I. *Appl. Sci.* **2018,** *8,* 1692. doi:10.3390/app8091692
10. Agarwal, D. C.; Chauhan, R. S.; Kumar, A.; Kabiraj, D.; Singh, F.; Khan, S. A.; Avasthi, D. K.; Pivin, J. C.; Kumar, M.; Ghatak, J.; Satyam, P. V. *J. Appl. Phys.* **2006,** *99,* 123105. doi:10.1063/1.2204333
11. Chelvanathan, P.; Shahahmadi, S. A.; Arith, F.; Sobayel, K.; Aktharuzzaman, M.; Sopian, K.; Alharbi, F. H.; Tabet, N.; Amin, N. *Thin Solid Films* **2017,** *638,* 213–219. doi:10.1016/j.tsf.2017.07.057
12. Chavan, K. B.; Desarada, S. V.; Chaure, N. B. *J. Mater. Sci.: Mater. Electron.* **2020,** *31,* 10306–10314. doi:10.1007/s10854-020-03578-2
13. Ahmed, N.; Khan, Z. S.; Ali, A.; Iqbal, M. A.; Shahzad, M. I.; Shahzad, N. *Mater. Today Commun.* **2023,** *34,* 105238. doi:10.1016/j.mtcomm.2022.105238
14. Hoffman, R. A.; Lin, J. C.; Chambers, J. P. *Thin Solid Films* **1991,** *206,* 230–235. doi:10.1016/0040-6090(91)90427-y
15. Navin, K.; Gupta, A.; Koyiloth Vayalil, S. *Appl. Phys. A: Mater. Sci. Process.* **2024,** *130,* 316. doi:10.1007/s00339-024-07466-y
16. Thornton, J. A.; Hoffman, D. W. *J. Vac. Sci. Technol. (N. Y., NY, U. S.)* **1977,** *14,* 164–168. doi:10.1116/1.569113
17. Sun, S.-S. *J. Vac. Sci. Technol., A* **1986,** *4,* 572–576. doi:10.1116/1.573850
18. Tripathi, J. K.; Novakowski, T. J.; Joseph, G.; Linke, J.; Hassanein, A. *J. Nucl. Mater.* **2015,** *464,* 97–106. doi:10.1016/j.jnucmat.2015.04.022
19. Klaver, P.; Haddeman, E.; Thijsse, B. *Nucl. Instrum. Methods Phys. Res., Sect. B* **1999,** *153,* 228–235. doi:10.1016/s0168-583x(99)00050-6
20. Ono, K.; Miyamoto, M.; Nakano, T.; Hiraoka, Y. *J. Nucl. Mater.* **2011,** *415,* S1214–S1217. doi:10.1016/j.jnucmat.2010.11.003
21. Takamura, S. *Plasma Fusion Res.* **2014,** *9,* 1405131. doi:10.1585/pfr.9.1405131
22. Jauberteau, I.; Bessaudou, A.; Mayet, R.; Cornette, J.; Jauberteau, J.; Carles, P.; Merle-Méjean, T. *Coatings* **2015,** *5,* 656–687. doi:10.3390/coatings5040656
23. Kim, D. J.; Kim, I.-S.; Kim, Y. T.; Park, J.-W. *MRS Online Proc. Libr.* **1999,** *563,* 45. doi:10.1557/proc-563-45
24. Lee, J.; Park, J. K.; Lee, J. W.; Heo, Y.; Oh, Y. S.; Lee, J. S.; Cho, J.; Jeen, H. *RSC Adv.* **2020,** *10,* 44339–44343. doi:10.1039/d0ra08533b
25. Carreri, F. C.; Oliveira, R. M.; Oliveira, A. C.; Silva, M. M. N. F.; Ueda, M.; Silva, M. M.; Pichon, L. *Appl. Surf. Sci.* **2014,** *310,* 305–310. doi:10.1016/j.apsusc.2014.03.086
26. Nakano, T.; Miyamoto, M.; Hasuike, S.; Ono, K.; Yoshida, N. *J. Nucl. Mater.* **2011,** *417,* 834–837. doi:10.1016/j.jnucmat.2010.12.143
27. Mändl, S.; Gerlach, J. W.; Assmann, W.; Rauschenbach, B. *Surf. Coat. Technol.* **2003,** *174-175,* 1238–1242. doi:10.1016/s0257-8972(03)00457-2
28. Mändl, S.; Manova, D.; Gerlach, J. W.; Assmann, W.; Neumann, H.; Rauschenbach, B. *Surf. Coat. Technol.* **2004,** *180-181,* 362–366. doi:10.1016/j.surfcoat.2003.10.134
29. Oubaki, R.; Machkih, K.; Larhlimi, H.; Samih, Y.; Alami, J.; Makha, M. *Thin Solid Films* **2024,** *790,* 140217. doi:10.1016/j.tsf.2024.140217
30. Tripathi, J. K.; Novakowski, T. J.; Hassanein, A. *Appl. Surf. Sci.* **2015,** *353,* 1070–1081. doi:10.1016/j.apsusc.2015.06.173
31. Pethe, S. A.; Takahashi, E.; Kaul, A.; Dhere, N. G. *Sol. Energy Mater. Sol. Cells* **2012,** *100,* 1–5. doi:10.1016/j.solmat.2011.11.038
32. Gupta, T.; Chauhan, R. P. *J. Mater. Sci.: Mater. Electron.* **2021,** *32,* 6185–6198. doi:10.1007/s10854-021-05335-5
33. Cullity, B. D.; Stock, S. R. *Elements of X-Ray Diffraction,* 3rd ed.; Pearson Education Limited: Harlow, UK, 2001.
34. Rashid, H.; Rahman, K. S.; Hossain, M. I.; Nasser, A. A.; Alharbi, F. H.; Akhtaruzzaman, M.; Amin, N. *Results Phys.* **2019,** *14,* 102515. doi:10.1016/j.rinp.2019.102515
35. Das, R.; Deo, M.; Mukherjee, J.; Ramachandra Rao, M. S. *Surf. Coat. Technol.* **2018,** *353,* 292–299. doi:10.1016/j.surfcoat.2018.08.065
36. Hu, K.; Xu, X.; Hu, Q. F.; Li, Q.; Ma, J. *Thin Solid Films* **2023,** *768,* 139724. doi:10.1016/j.tsf.2023.139724
37. Huang, Y.; Gao, S.; Tang, Y.; Ao, J.; Yuan, W.; Lu, L. *Thin Solid Films* **2016,** *616,* 820–827. doi:10.1016/j.tsf.2016.09.058
38. Blösch, P.; Güttler, D.; Chirila, A.; Tiwari, A. N. *Thin Solid Films* **2011,** *519,* 7453–7457. doi:10.1016/j.tsf.2010.12.187
39. Chawla, V.; Jayaganthan, R.; Chawla, A. K.; Chandra, R. *J. Mater. Process. Technol.* **2009,** *209,* 3444–3451. doi:10.1016/j.jmatprotec.2008.08.004
40. Chawla, V.; Jayaganthan, R.; Chandra, R. *Mater. Charact.* **2008,** *59,* 1015–1020. doi:10.1016/j.matchar.2007.08.017
41. Liedtke-Grüner, S.; Grüner, C.; Lotnyk, A.; Gerlach, J. W.; Mensing, M.; Schumacher, P.; Rauschenbach, B. *Thin Solid Films* **2019,** *685,* 8–16. doi:10.1016/j.tsf.2019.05.062
42. Grayeli, A.; Sadeghi, M.; Shakoury, R.; Matos, R. S.; da Fonseca Filho, H. D.; Arman, A. *Opt. Quantum Electron.* **2024,** *56,* 1142. doi:10.1007/s11082-024-07039-6
43. Deambrosis, S. M.; Miorin, E.; Montagner, F.; Zin, V.; Fabrizio, M.; Sebastiani, M.; Massimi, F.; Bemporad, E. *Surf. Coat. Technol.* **2015,** *266,* 14–21. doi:10.1016/j.surfcoat.2015.02.006
44. Liu, Y.; He, T.; Chen, D.; Yang, H.; Ferguson, I. T.; Huang, D.; Feng, Z. C. *J. Alloys Compd.* **2020,** *848,* 156631. doi:10.1016/j.jallcom.2020.156631
45. Gavrilova, N.; Myachina, M.; Harlamova, D.; Nazarov, V. *Colloids Interfaces* **2020,** *4,* 24. doi:10.3390/colloids4020024
46. Dan, Z.; Yang, Y.; Qin, F.; Wang, H.; Chang, H. *Materials* **2018,** *11,* 446. doi:10.3390/ma11030446
47. Vellaichamy, B.; Periakaruppan, P. *New J. Chem.* **2017,** *41,* 4006–4013. doi:10.1039/c7nj00084g
48. Bommali, R. K.; Mahapatra, D. P.; Gupta, H.; Guha, P.; Topwal, D.; Vijaya Prakash, G.; Ghosh, S.; Srivastava, P. *J. Appl. Phys.* **2018,** *124,* 063107. doi:10.1063/1.5043386

49. Lombardo, S.; Battaglia, A.; Foti, M.; Tringali, C.; Cannella, G.; Costa, N.; Gerardi, C.; Principato, F. *Energy Procedia* **2014,** *44,* 216–222. doi:10.1016/j.egypro.2013.12.030
50. Kotsedi, L.; Mthunzi, P.; Nuru, Z. Y.; Eaton, S. M.; Sechoghela, P.; Mongwaketsi, N.; Ramponi, R.; Maaza, M. *Appl. Surf. Sci.* **2015,** *353,* 1334–1341. doi:10.1016/j.apsusc.2015.08.047
51. Javed, A.; Khan, N.; Bashir, S.; Ahmad, M.; Bashir, M. *Mater. Chem. Phys.* **2020,** *246,* 122831. doi:10.1016/j.matchemphys.2020.122831
52. Singh, Y. *Int. J. Mod. Phys.: Conf. Ser.* **2013,** *22,* 745–756. doi:10.1142/s2010194513010970
53. Gupta, D.; Kumar, R. *Mater. Sci. Semicond. Process.* **2023,** *158,* 107326. doi:10.1016/j.mssp.2023.107326
54. Benramache, S.; Aoun, Y.; Lakel, S.; Benhaoua, B. *Mater. Res. Express* **2019,** *6,* 126418. doi:10.1088/2053-1591/ab574a

License and Terms